Detonation in Spatially Inhomogeneous Media

XiaoCheng Mi

Department of Mechanical Engineering
McGill University

February 13, 2018

A dissertation submitted to McGill University in partial fulfillment of the requirements for the degree of
Doctor of Philosophy

Knowledge does not come from amusement, but from hard work;
Virtue is nurtured not by following, but by independent thinking.

— Han Yu, *An Explication of Progress in Learning*

Abstract

Detonation propagation in a compressible medium wherein the energy release has been made spatially inhomogeneous is examined via numerical simulations. The inhomogeneity is introduced via concentrating reactive material into regions which are separated by inert gaps while maintaining the same average energy density. The propagation velocity and propagation limit of detonation waves under the influence of these imposed inhomogeneities are put to a rigorous examination.

Spatial inhomogeneities are introduced to adiabatic detonation systems with a hierarchy of complexities. In a system governed by one-dimensional Euler equations with a simplified mechanism of instantaneous energy deposition, i.e., a source triggered by the passage of leading shock after a prescribed delay time, the resulting averaged propagation speed over hundreds of spatially discrete sources is compared to the ideal Chapman-Jouguet (CJ) speed for an equivalent amount of energy release. Velocities in excess of the CJ speed are found as the reactive regions are made increasingly discrete, with deviation above CJ being as great as 15%. The deviation above the CJ value increases with decreasing values of specific heat ratio γ. When the sources are sufficiently spread out so as to make the energy release of the media nearly continuous, the classic CJ solution is obtained for the average wave speed. In the limit of highly discrete sources, time-averaged mean wave structure shows that the effective sonic surface does not correspond to an equilibrium state. The average state of the flow leaving the wave in this case does eventually reach the equilibrium Hugoniot, but only after the effective sonic surface has been crossed. Thus, the super-CJ waves observed in the limit of highly discretized sources can be understood as weak detonations due to the non-equilibrium state at the effective

sonic surface.

The investigation on how detonation velocity is influenced by the presence of spatial inhomogeneities is then extended to one- and two-dimensional systems with a more realistic mechanism of energy release, i.e., single-step Arrhenius kinetics. In the case of sufficiently inhomogeneous media wherein the spacing between the reactive zones is greater than the inherent reaction zone length, average wave speeds significantly greater than the corresponding CJ speed of the homogenized medium are obtained. If the shock transit time between reactive zones is less than the reaction time scale, then the classical CJ detonation velocity is recovered. The super-CJ wave propagation is also identified in the cases with a two-dimensional arrangement of spatial inhomogeneities. The correspondence of the super-CJ behavior identified in this study with real detonation phenomena that may be observed in experiments is discussed.

Finally, a random distribution of spatially discrete sources is implemented into a two-dimensional detonation system confined by an inert, compressible layer of gas. In this system, detonation waves experience losses due to lateral expansion behind a curved shock front and, thus, propagate at a velocity lower than the ideal CJ velocity. As the thickness of the reactive layer within the confinement decreases, the deficit in propagation velocity increases; below a critical thickness, detonations can no longer propagate in a self-sustained manner. The critical thickness for a steady propagation is determined for a homogeneous reactive medium and a mixture with randomly distributed, discrete reactive sources. The simulation results show that, for a sufficiently high activation energy, the spatial inhomogeneities assist a detonation wave to propagate beyond the limit that is encountered in a homogeneous reactive medium. This enhancing effect of the spatial inhomogeneities on the near-limit propagation of detonation waves is found to be more pronounced with increasing activation energy.

Résumé

L'étude de la propagation d'une onde de détonation dans un milieu compressible inhomogène est menée à l'aide de simulations numériques. L'inhomogénéité du milieu est introduite en imposant une concentration plus haute de matières réactives dans certaines régions séparées les unes des autres par du gaz inerte tout en conservant une densité d'énergie moyenne constante. L'influence des inhomogénéités spatiales sur la vitesse de propagation du front d'onde et sur la limite de propagation des ondes de détonation est étudiée avec rigueur et précision.

Les inhomogénéités spatiales sont introduites dans des systèmes adiabatiques avec un degré de complexité croissante. Dans un système unidimensionnel inhomogène gouverné par les équations d'Euler et avec un mécanisme de déposition d'énergie simplifié (une source est déclenchée lors du passage du front d'onde après un certain intervalle de temps), la vitesse de propagation moyenne de l'onde est mesurée puis comparée à la vitesse de propagation obtenue dans les conditions idéales de Chapman-Jouguet (CJ) dont la quantité d'énergie libérée est identique. A mesure que les régions réactives sont de plus en plus discrètes, on observe des vitesses supérieures à la vitesse CJ, la déviation pouvant atteindre jusqu'à 15%. L'écart (excédentaire) avec la vitesse CJ est d'autant plus grand que le coefficient adiabatique γ décroît. Lorsque les sources sont suffisamment dispersées, tout en conservant une quantité l'énergie libérée identique, on retrouve la vitesse CJ pour la vitesse de propagation moyenne. Dans le cas limite où les sources discrètes sont fortement éparpillées, la structure moyenne de l'onde révèle que la surface sonique effective ne correspond pas à un état d'équilibre. L'état thermodynamique moyen du milieu quittant le système d'ondes peut éventuellement atteindre l'équilibre d'Hugoniot

mais une fois seulement que la surface sonique effective a été dépassée. Ainsi, les ondes super-CJ observées dans le cas limite où les sources discrètes sont très espacées peuvent être considérées comme de faibles détonations dues à l'état de non-équilibre de la surface sonique effective.

L'étude de l'influence des inhomogénéités sur la vitesse de propagation de l'onde de détonation est ensuite étendue à des cas unidimensionnels et bidimensionnels avec un mécanisme de libration d'énergie plus réaliste i.e. la cinétique d'Arrhenius en une seule étape. Dans le cas de milieux inhomogènes où l'espacement entre les différentes zones actives est plus grand que la zone de réaction intrinsèque, la vitesse moyenne de l'onde est considérablement plus grande que la vitesse CJ correspondante obtenue dans un milieu homogène. Si l'onde de choc parcourt la distance séparant deux zones actives consécutives avec un délai inférieur au temps de réaction alors la vitesse classique de CJ est de nouveau obtenue. La propagation des ondes super-CJ est également visible quand les inhomogénéités sont reparties dans les deux directions de l'espace. Le comportement des ondes super-CJ simulé dans cette étude numérique est comparé aux phénomènes observés dans de véritables expériences.

Enfin, une distribution aléatoire de sources discrètes est implémentée dans un système de détonation bidimensionnel isolé par une couche de gaz compressible inerte. Dans ce système, l'onde de détonation perd une certaine quantité de mouvement à cause de l'expansion latérale se produisant avec une onde de choc incurvée, d'où une vitesse de propagation plus faible que dans le cas idéal de CJ. À mesure que l'épaisseur de la couche réactive dans le système confiné décroît, la vitesse de propagation décroît également et l'écart avec le cas idéal augmente; en dessous d'une valeur limite, la détonation ne peut plus avoir lieu de manière auto-entretenue. L'épaisseur limite pour avoir une propagation auto-entretenue est déterminée pour le cas d'une détonation dans un milieu réactif homogène et pour un système avec des sources actives discrètes réparties aléatoirement dans

le domaine. Les résultats des simulations montrent que, pour une énergie d'activation suffisamment grande, les inhomogénéités discrètes présentes dans le domaine contribuent à la propagation des ondes de détonation au-delà de la limite précédemment trouvée pour un milieu réactif homogène. Cet effet des inhomogénéités sur la limite de propagation est d'autant plus prononcé que l'énergie d'activation est grande.

Acknowledgment

Prof. Andrew J. Higgins, with his continued guidance, support, and encouragement over the past four years of my PhD study, renders me speechless, and brings tears to my eyes at this very moment for me to acknowledge him. Any form of "thank you" would sound too pale to express my gratitude towards him as my mentor and, more importantly, the sincerest friend that I have ever made in my life. *Living everyday of my life as if it was the day to make a difference* is perhaps the best way to let someone know that I have been and am always proud of being one of Prof. Higgins' students.

I am deeply grateful to Profs. Hoi Dick Ng, Nikolaos Nikiforakis, Evgeny V. Timofeev, Charles B. Kiyanda, and Jianling Li for sharing me their enormous amount of knowledge and sophisticated tools for computational fluid dynamics. A large number of the simulations presented in this dissertation would not have been done without their generous assistance. Our collaboration with Prof. Jianling Li and use of her CFD code in 2013 was my first introduction to detonation physics.

My grateful acknowledgment is due to many researchers in the field of detonation science around the globe: Profs. Matei I. Radulescu, Ashwin Chinnayya, Aslan R. Kasimov, Drs. Mark Short, John B. Bdzil, and Scott I. Jackson. Their constructive advice and criticism are so valuable for me to significantly improve the scientific quality of my dissertation.

I would also like to thank Prof. John H.S. Lee, Dr. Samuel Goroshin, Profs. Jeffrey

M. Bergthorson and David L. Frost for broadening my knowledge in shock wave physics and combustion science beyond the scope of my dissertation. Collaborating and having discussions with them also provided me some interesting insights towards my own research project.

Over the past four years, I have been so fortunate to meet and develop friendships with my academic brothers and sisters at McGill University. Many thanks go to Justin Huneault, Dr. Jason Loiseau, William Georges, Myles Hildebrand, Fredric Lam, Alex Wright, John Lian, Kelechi Ezeji, Janakiraman Boopathy, Dr. Michael Soo, Jan Palecka, Dr. Philippe Julien, Quentin Pontalier, James Vickery, Samuël Vaillancourt, Ramsey Hamadeh, Jihane Kamil, Oscar Ng, Raphaël Limbourg, Kelsey Tang Yuk, Ivan Hung, and Abtin Ameri for making the research, sport, and drinking activities in my grad life unforgettably pleasant. Raphaël's careful translation of the abstract of this dissertation into French is especially appreciated.

At the end, I would like to extend my full gratitude to my loving parents and grandmother, as well as my grandfather in heaven, for supporting, understanding, and never losing their confidence in me throughout my entire life.

Preface

This present dissertation consists of manuscripts which are in publication (Ch. 2) or being prepared for submission (Ch. 3). My own and my collaborators' contributions towards the accomplishment of each research project are listed below:

Chapter 2 (Sec. 2.1): This section of the present thesis contains material that appears in "Effect of spatial discretization of energy on detonation wave propagation," **817**, 306-338, *Journal of Fluid Mechanics*, 2017. [1] In order to model the one-dimensional gasdynamic system coupled with an instantaneous energy deposition process, I wrote a simulation code based on a fixed (non-adaptive) uniform grid. Most of the results reported in this article were obtained by myself using my simulation code. The data points for highly spatially discretized sources (plotted in Figs. 2.5 and 2.6) were obtained by Evgeny Timofeev, enabled by his simulation code with adaptive mesh refinement (AMR). This manuscript was partially written by me with a substantial amount of text in the Introduction and Discussions written by Andrew Higgins and a description of the AMR methodology written by Evgeny Timofeev. Scientific advice and editorial support were provided by both co-authors, with additional input from the anonymous peer reviewers.

Chapter 2 (Sec. 2.2): This section of the present thesis contains material that appears in "Propagation of gaseous detonation waves in a spatially inhomogeneous reactive medium," **2**, 053201, *Physical Review Fluids*, 2017. [2] The simulation code used in this study to solve the one-dimensional reactive Euler equations coupled with a temperature-dependent reaction model was developed by myself. The two-

dimensional simulations were performed by me using a code based on a GPU-accelerated computing architecture, which was originally written by Nikolaos Nikiforakis' research group at the University of Cambridge, UK, and further developed by me to treat the specific problem at hand. Hoi Dick Ng introduced me to this GPU-based code and assisted me in its further development. Charles Kiyanda set up and maintained a workstation that allowed me to perform the simulations on GPU computing processors. This manuscript was entirely written by myself and edited by the co-authors (Andrew Higgins, with additional input from Hoi Dick Ng and Charles Kiyanda).

Chapter 3: The manuscript of this chapter is being prepared for submission to the *Shock Waves* Journal, which was entirely written by myself and edited by Andrew Higgins. The GPU-based code was further developed by me to model a two-dimensional detonation system with a charge of randomly distributed discrete sources confined by a layer of inert gas. A theoretical model was implemented by me to provide a prediction that can be compared with the simulation results. The detail of this model (shown in Appendices C and D) was published in "Geometric scaling for a detonation wave governed by a pressure-dependent reaction rate and yielding confinement", **27**, 027102, *Physics of Fluids*, 2015. [3] That study utilized the results of simulations that used a code written by Jianling Li for comparison to the theoretical model, however, results using that code are not included in this dissertation.

The original contributions of this dissertation are:

1. A detonation wave, under the influence of sufficiently discretized energy release, may propagate at a velocity significantly greater than the Chapman Jouguet (CJ) ve-

locity for a homogeneous system with the same amount of energy release. This result was demonstrated using computational simulations in which the sources were deposited via direct energy deposition into the computational cells. The super-CJ result was also reproduced in a more realistic gas-phase detonation system in which the energy release was controlled by Arrhenius kinetics, in both one- and two-dimensional systems. Decreasing either the discreteness (i.e., spreading out the energy release zones so as to approach a homogeneous system) or decreasing the spacing of the inhomogeneities in comparison to the chemical length scale resulted in the wave speed reverting to the classical CJ solution.

2. The results of simulations of detonation in spatially discrete systems were analyzed via spatio-temporal averaging and space-time (x-t) diagrams. The averaging analysis revealed the super-CJ waves to be classified as weak detonations resulting from the nonequilibrium flow at the effective sonic surface at the exit of the detonation wave. Analysis of the transient wave dynamics and the reaction progress variable on an x-t diagram was used to define a discreteness parameter that can be used to quantify the deviation from the classical CJ solution. This result establishes the range of applicability of the CJ model of detonations and when that model is no longer appropriate due to the effect of discreteness.

3. The effect of the discrete energy sources on the near-limit propagation of detonation waves, i.e., assisting a detonation wave to propagate in a reactive layer thinner than the critical thickness resulting from a homogeneous medium, was demonstrated in a gas-phase detonation via computational simulations. The sensitizing effect of spatial inhomogeneities was found to increase when the activation energy was increased.

The outcome of this study contributes to the understanding of how the spatially inhomogeneous nature of gaseous detonations assist in sustaining detonation wave propagation in response to losses due to lateral expansion in the reaction zone.

Contents

List of Figures

Chapter 1

Introduction

1.1 Spatially inhomogeneous nature of detonation phenomena

The spatially inhomogeneous nature of detonations in explosive gases and condensed-phase energetic materials has been revealed over the past 60 years. [6, 7] The experimental evidence of cellular structure exhibited by gaseous detonations was first noted by Denisov and Troshin [8], and these detonation cells are now recognized as being essential for the propagation of detonations in high activation energy mixtures (e.g. hydrocarbon fuels and air). Over the past decade, using high-resolution schlieren and self-luminous photography, the spatially inhomogeneous wave and reaction zone structure of gaseous detonations have been illustrated in greater detail. [9, 4, 10] The structure consists of triple-point interactions between the leading shock and transverse shock waves that result in a cellular wave front. As a result of this spatially and temporally varying shock front compressing the reactive mixture at different strengths, the distribution of post-shock temperature varies greatly over the detonation cell cycle. Since the exothermic reactions

in gaseous combustible mixtures governed by Arrhenius kinetics are very temperature sensitive, the reaction rates in different regions behind the leading shock may differ by several orders of magnitude. Although zones of prompt reaction triggered by adiabatic compression may exist in regions of the front consisting of strong Mach stems, weakly-shocked pockets of reactant may not be able to undergo significant exothermic reaction due to their thermal history on the time scale of a detonation. [9, 4, 10] These pockets eventually burn out during the cell cycle, likely due to a turbulent flame-like mechanism, releasing their energy in compression waves that still help to support the leading front. A schlieren photograph of detonation structure in an oxygen/methane mixture (Fig. 1.1(a)) recorded and interpreted by Radulescu *et al.* [4] is shown as an example of spatially inhomogeneous gaseous detonations.

In some homogeneous condensed-phase explosives, detonations are also observed to develop multidimensional instabilities which resemble the cellular structure in gaseous detonations. The evidence of transverse waves that arise from homogeneous solid and liquid explosives can be found in the following examples: Cellular patterns formed by triple-point trajectories in cast trinitrotoluene (TNT) were captured by Howe *et al.* [11]; Urtiew *et al.* observed cellular patterns imprinted on a steel tube wall by a detonation in liquid nitromethane-acetone mixture [12]. The reaction zone structure of these initially homogeneous condensed-phase detonations likely exhibits spatial variations rendered by the interacting waves, similar to that in gaseous detonations.

In polycrystalline and slurry high-explosives, the mixtures are inherently inhomogeneous, and the reaction zone is usually controlled by the heterogeneity of the medium, wherein shock localization at density inhomogeneities results in local centers of energy release, so-called "hot spot", from which reaction fronts burnout the rest of the explosive within the reaction zone. Greater complications are unveiled in some recent experimental studies showing that a cellular-like wave structure may also arise in some heterogeneous

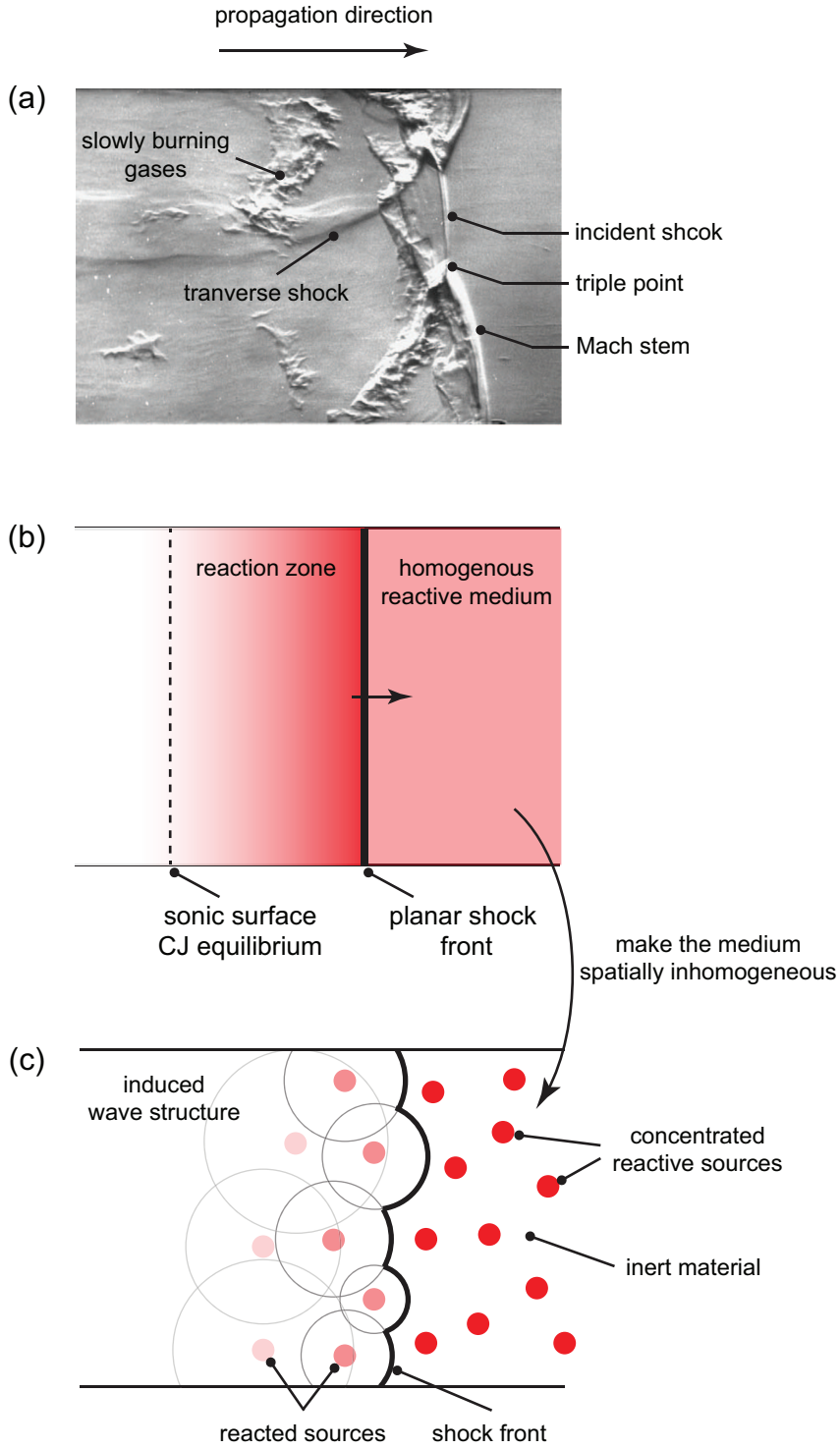

Figure 1.1: A schematic introducing the problem studied in this dissertation: (a) an example showing the spatially inhomogeneous nature of detonations (a schlieren photograph of detonation structure in an oxygen/methane mixture [4]); (b) the theoretical depiction of a detonation wave in the ZND solution; (c) a conceptual illustration of the approach of inducing complex wave structure by imposing spatial inhomogeneities in the reactive medium in which a detonation wave propagates.

explosives i.e., polymethyl methacrylate (PMMA)-gelled nitromethane mixed with glass micro-balloons [13] and vapor-deposited hexanitrostilbene (HNS) films [14]. The spatially inhomogeneous nature of detonation phenomena thus makes a notoriously challenging problem for theoretical description.

1.2 Theoretical description of detonation phenomena

Given such challenging problems of detonation research, the available theoretical tools deriving from first principles are surprisingly simple. Over a century ago, the first conceptual picture of a detonation wave was independently proposed by Chapman and Jouguet [15, 16]. In this theoretical model, the flow of reactants enters the coupled shock and reaction complex at the detonation velocity, and the flow of products exits this wave complex at the local sonic speed, which is known as the Chapman-Jouguet (CJ) criterion. Knowing the chemical energy density and the thermodynamic state of the reactive medium, the detonation velocity can be predicted by applying CJ criterion to the conservation equations. Nearly 50 years later, the steady, one-dimensional flow structure linking the upstream state and downstream CJ equilibrium state of a detonation wave was independently solved by Zeldovich [17], von Neumann [18], and Döring [19], which is known as the ZND solution. A conceptual illustration of the ZND solution of detonation structure is shown in Fig. 1.1 (b).

Based on the ZND solution, quasi-one-dimensional models with losses were developed. For detonations experiencing lateral expansion, an analytic relation between the detonation velocity deficit and the curvature of the leading shock front at the central axis (i.e., D_{N}-κ relation) was obtained by Wood and Kirkwood [20]. If a D_{N}-κ relation is provided, a procedure of geometrically constructing a two-dimensional leading shock front, which was even earlier proposed by Eyring et al. [5], can be used to obtain a relation between

detonation velocity deficit and charge diameter as well as to predict the critical size below which a detonation fails to propagate. Since the early 1980's, inspired by Whitham's theory of Geometrical Shock Dynamics (GSD) [21], a theory of Detonation Shock Dynamics (DSD) assuming a smooth, weakly-curved detonation front and a slowly evolving flow structure has been developed to describe the propagation of detonation waves in two- or three-dimensional space [22, 23, 24].

Perhaps in all theoretical models of detonations, a smooth, laminar-like wave structure and a homogeneous reactive medium based on the averaged thermodynamics, flow and chemical properties are assumed. The question then arises as to whether the propagation behavior of detonation waves that are influenced by their inhomogeneous nature can be accurately predicted by these simple models based on an averaging treatment. Answering this question is attempted in the current thesis.

1.3 Objective of the thesis

The objective of this thesis is to examine how spatial inhomogeneities affect the propagation of detonations via computational simulations. It is however worthwhile to note that to numerically resolve the self-developed instabilities in a multidimensional detonation complex is a challenging task as well. As shown for example by Mazaheri *et al.*, a fully converged result cannot be obtained for a two-dimensional, cellular detonation structure at a numerical resolution of 10^3 to 10^4 computational cells per half-reaction-zone length[1] [25] It is rather difficult to quantitatively characterize these inhomogeneities developed in the reaction zone as they significantly vary with numerical resolution; thus, it

[1]Numerical resolution of the reaction zone dynamics within a detonation wave complex is commonly assessed by comparing the computational grid size to the characteristic length of the reaction zone coupled to the leading shock front. This characteristic length can be evaluated as the distance downstream from the leading shock to the location where 50% of the reactants have been converted to products in the ideal ZND wave structure, which is known as the half-reaction-zone length.

is questionable to use these simulations to scrutinize the effect of spatial inhomogeneities on the overall propagation behavior of detonations.

In this current work, instead of exhausting the computational efforts to resolve the naturally developed instabilities from a homogeneous reactive medium, complex wave structures can be induced by imposing spatial inhomogeneities in the initial detonable medium. Starting from a homogeneous reactive medium, inhomogeneities can be implemented by collecting the reactive material in the medium and concentrating them into spatially discrete pockets that are separated by inert material. The imposed inhomogeneities can be quantitatively characterized and controlled; the induced wave structure is hypothesized to have the same effects on detonation propagation as those resulting from the intrinsic instabilities or the complex mesoscale morphologies. This approach of imposing inhomogeneities, as illustrated in Fig. 1.1(c), draws inspiration from Vasil'ev and Nikolaev's heuristic model [26], which utilized two-dimensionally arranged point-like sources to induce interacting blast waves mimicking detonation cell structure.

Using the above-mentioned approach, this present body of work builds upon similar research examining flame propagation in discretized media, in which point-like sources release heat to diffuse outward and trigger subsequent sources [27, 28, 29, 30, 31, 32]. A wave propagation mechanism by which an energetic source generates a blast that, in turn, can initiate the next source was proposed by Stewart and Asay [33] in modeling the response of propellant beds comprised of explosive grains to strong shock stimuli. They outlined a "theory of discrete interactions" in which initiation of subsequent sources would be described by a nonlinear recursion relation. Propagation of detonation in media with a sinusoidal variation in properties was explored computationally by Morano and Shepherd [34] in one dimension and extended to two dimensions by Li *et al.* [35]. In these

studies, no significant deviation greater than 2% away from CJ was observed when the detonation propagated without losses present. Li *et al.* did observe enhanced wave speeds when the detonation propagated in a layer with inhomogeneities and yielding confinement (in comparison to a detonation propagating in a homogeneous layer with the same yielding confinement). [35]

The effect of spatial inhomogeneities on the wave propagation velocity in adiabatic detonation systems with a hierarchy of complexities will be investigated in Ch. 2. By introducing spatial inhomogeneities to a detonable mixture confined by a compressible, inert layer, their influence on the critical charge thickness marking the propagation limit will be examined in in Ch. 3. Simulation results will then be analyzed and compared with the theoretical predictions made using the models (briefly reviewed in Sec. 1.2) which neglect the presence of spatial inhomogeneities. The difference between the simulation and analysis results and the theoretical predictions will be discussed in order to further elucidate the physical mechanisms of a spatially inhomogeneous reaction zone supporting a detonation complex to propagate.

Chapter 2

Effect of spatial inhomogeneities on detonation velocity

Despite the inhomogeneous features of detonations as reviewed in Sec. 1.1, the average velocity of detonation fronts is usually very close to the predictions of the CJ criterion. Detonation waves in gaseous is usually observed to propagate within 1% of the equilibrium CJ velocity (V_{CJ}). In condensed-phase energetic materials, the prediction of V_{CJ} is also fairly close to the experimental measurement, despite some uncertainty in the equation of state of condensed materials at extremely high pressure. The success of the steady, one-dimensional CJ criterion in predicting the propagation speed of a detonation wave with a highly complex, transient structure seems thus contradictory. Although this paradoxical situation was first articulated by A.K. Oppenheim in 1961 [36], a fully satisfactory explanation still eludes researchers.

In this chapter, the CJ prediction of detonation velocity will be put to a rigorous examination. Spatial inhomogeneities in chemical reactivity will be imposed to the initial explosive mixtures. The detonations propagating in these inhomogeneous media will be computationally simulated. The resulting propagation velocity will then be compared

with the corresponding V_{CJ} for the same amount of energy release. This examination on detonation velocity will be performed in several modeling systems with a hierarchy of complexities. In Sec. 2.1, the modeling system is governed by the one-dimensional Euler equations with spatial inhomogeneities introduced via concentrating reactant into spatially discrete layers separated by inert gaps. The simplest mechanism of energy deposition is incorporated in this model: each reactive layer is instantaneously triggered by the passage of the leading shock after a prescribed delay time. A system based on Euler equations with single-step Arrhenius kinetics is modeled in Sec. 2.2 to investigate the effect of spatial inhomogeneities on the propagation velocity of gaseous detonations. The simulations are also extended to two dimensions in this section.

2.1 One-dimensional detonation system with an instantaneous energy deposition

The objective of this section is to put the CJ criterion to a rigorous test by examining detonation in a media in which the energy release is concentrated into spatially discrete layers separated by regions of inert gas (as illustrated in Fig. 2.1). The energetic layers will release their energy when activated by a passing shock front after a fixed delay time. The new blast wave generated by the energy release becomes the mechanism to initiate additional sources, such that the wave propagates via a sequence of "sympathetic detonations." The spatial scale of the sources and their spacing will be varied, examining the behavior of the wave propagation in this system from continuous energy release (i.e., no discretization) to highly-concentrated sources in the limit of δ-function-like sources of energy separated by layers of inert gas. The overall energy release will be maintained as constant, so that the average wave velocity can always be compared to the equivalent CJ speed of the homogenized media.

The plan for this section is as follows. In Sec. 2.1.1, the problem statement and parameters will be defined. Section 2.1.2 describes the numerical methodology used to solve the governing Euler equations. Section 2.1.3 presents the results of a study where each of the model parameters was systematically varied and compared to the ideal CJ detonation velocity of the equivalent homogenous media. Section 2.1.3.3 analyzes the results by temporally averaging select simulations to provide a quasi-steady one-dimensional description of the transient waves. The results are discussed in Sec. 2.1.4 and summarized in the Conclusions (Sec. 2.1.5). An Appendix presents an *ad hoc*, or heuristic, model that attempts to construct an analytic solution to this problem for the case of zero delay in triggering the sources.

2.1.1 Problem statement

This study considers a calorically perfect gas (i.e., fixed ratio of specific heats γ) that has the potential to release energy with a heating value of $\widetilde{Q}$ (J/kg). The tilde "$\sim$" denotes a dimensional quantity. The flow variables, density, pressure, and particle velocity, are non-dimensionalized with reference to the initial state ahead of the leading shock, i.e., $\rho = \widetilde{\rho}/\widetilde{\rho}_0$, $p = \widetilde{p}/\widetilde{p}_0$, and $u = \widetilde{u}/\sqrt{\widetilde{p}_0/\widetilde{\rho}_0}$, respectively, and the space coordinate x by the spacing between two adjacent sources $\widetilde{L}$, i.e., $x = \widetilde{x}/\widetilde{L}$. The subscript "0" indicates the initial state of the uniform reactive medium. The heat release $\widetilde{Q}$ is non-dimensionalized as $Q = \widetilde{Q}/\left(\widetilde{p}_0/\widetilde{\rho}_0\right)$. A detonation wave propagating through this uniform medium is expected to move at the non-dimensional CJ speed, given by,

$$V_{\mathrm{CJ}} = M_{\mathrm{CJ}} c_0 = \left\{ \sqrt{\frac{\gamma^2-1}{\gamma} Q + \sqrt{\left(\frac{\gamma^2-1}{\gamma} Q + 1\right)^2 - 1} + 1} \right\} \sqrt{\gamma} \tag{2.1}$$

where c_0 denotes the non-dimensionalized initial speed of sound and equals $\sqrt{\gamma}$. Equation 2.1 is the classical CJ detonation solution, and is used to compare the resulting propagation speeds from the discrete source simulations with that of the steady detonation in the equivalent homogeneous media. All the simulation results of wave speeds reported in this paper are normalized by the corresponding V_{CJ}.

To examine the effect of spatial discretization, the energy is initially collected in regions with width $\widetilde{W}$ (source width) that are spaced a distance $\widetilde{L}$ apart (i.e., the distance $\widetilde{L}$ is, for example, from the right edge of a source to the right edge of its neighbor). The total energy release per unit mass of the medium remains fixed at Q, so the energy in each concentrated source is $Q\widetilde{L}/\widetilde{W}$. The initial discreteness of the system is described by a parameter $\Gamma_{\mathrm{init}} = \widetilde{W}/\widetilde{L}$. As $\Gamma_{\mathrm{init}} \to 0$, the sources of energy become highly spatially concentrated. In the limit of $\Gamma_{\mathrm{init}} \to 1$, the energy release becomes continuous through the

medium. In most of the simulations reported in this paper, the following mechanism of energy deposition is incorporated (unless otherwise specified). A discrete source of energy is instantaneously triggered by the passage of a rightward-propagating shock wave past the right edge of the source, independent of the strength of the shock, after a non-dimensional time delay $t_{\rm d}$ (time variables are non-dimensionalized as $t = \widetilde{t}/\left(\widetilde{L}/\sqrt{\widetilde{p}_0/\widetilde{\rho}_0}\right)$). This time delay is reported as another non-dimensional value $\tau = t_{\rm d}V_{\rm CJ}$, where the time required for the CJ detonation to propagate over the distance $\widetilde{L}$ in the equivalent homogenous system has been used to non-dimensionalize the delay time. Note that the non-dimensionalized spacing between two adjacent sources is unity.

Two different scenarios of sources are considered: fixed and convected sources that deposit their energy instantaneously. For fixed sources, the energy source is considered to be independent of the inert, gaseous media and is not convected along with it. Conceptually, this would correspond to a fine mesh of explosive wire in a tube filled with inert gas, wherein the mesh spans the tube cross-sectional area and is attached to the tube wall. In this case, the shock-accelerated, inert gas is free to flow (without resistance) around the sources of energy, which remain fixed until they release their energy. In the second scenario (convected sources), the sources are assumed to be embedded in the inert, gaseous media and convect along with it. This would correspond to a layer of explosive dust, suspended between sections of inert gas. As the successive blast waves propagate through the media, the sources in this scenario are compressed and convected along with the post-shocked inert gas. The two above-described scenarios are illustrated schematically in Fig. 2.2.

For an instantaneous energy deposition, after the delay time has elapsed, the energy that is released by the source is deposited in the volume occupied by the source at that moment. Maintaining the overall amount of specific heat release of the medium at Q, the conservation laws require that the energy deposition results in an increase in the pressure

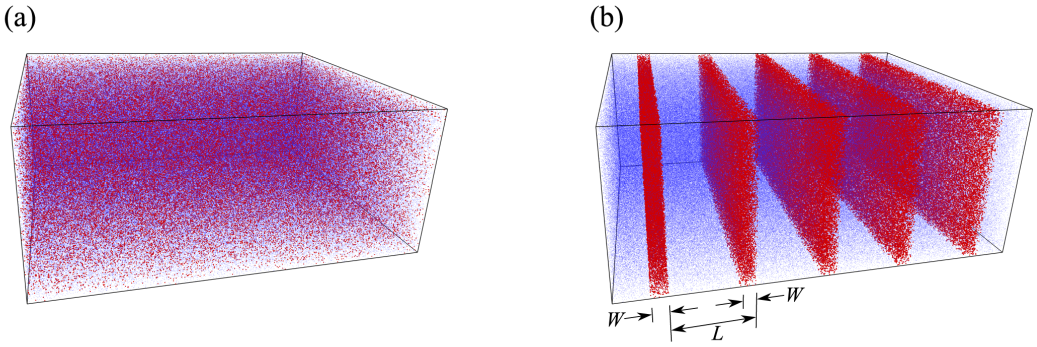

Figure 2.1: Schematic of an explosive medium with (a) source energy (red dots) uniformly distributed throughout inert medium (blue dots) and with (b) source energy collected into planar sheets (layers of red dots of width W and spacing L) with inert media in between.

in the region of an activated source by an amount given by,

$$\Delta p = \frac{Q\,(\gamma - 1)}{\Gamma} \tag{2.2}$$

where Γ is the effective spatial discreteness of a source when it instantaneously releases energy. It is important to note that, in the scenario of fixed sources, the source width remains constant as being processed by the leading shock and hence $\Gamma = \Gamma_{\text{init}}$; in the scenario of convected sources, the actual source width $\widetilde{W}$ at the instant of energy release is smaller than its initial value, i.e., $\Gamma < \Gamma_{\text{init}}$, due to the compression of the media in which the source energy is stored and the particle motion induced by the passage of the shock wave. The numerical implementation of delay time and convected source tracking and energy addition is described in Sec. 2.1.2. This method of adding energy to a compressible flow is essentially the same as that originally used by [37] to numerically simulate the Taylor-Sedov point-blast problem.

The gasdynamics of the proposed system coupled with a mechanism of instantaneous energy deposition after a delay time can be described by the one-dimensional Euler equa-

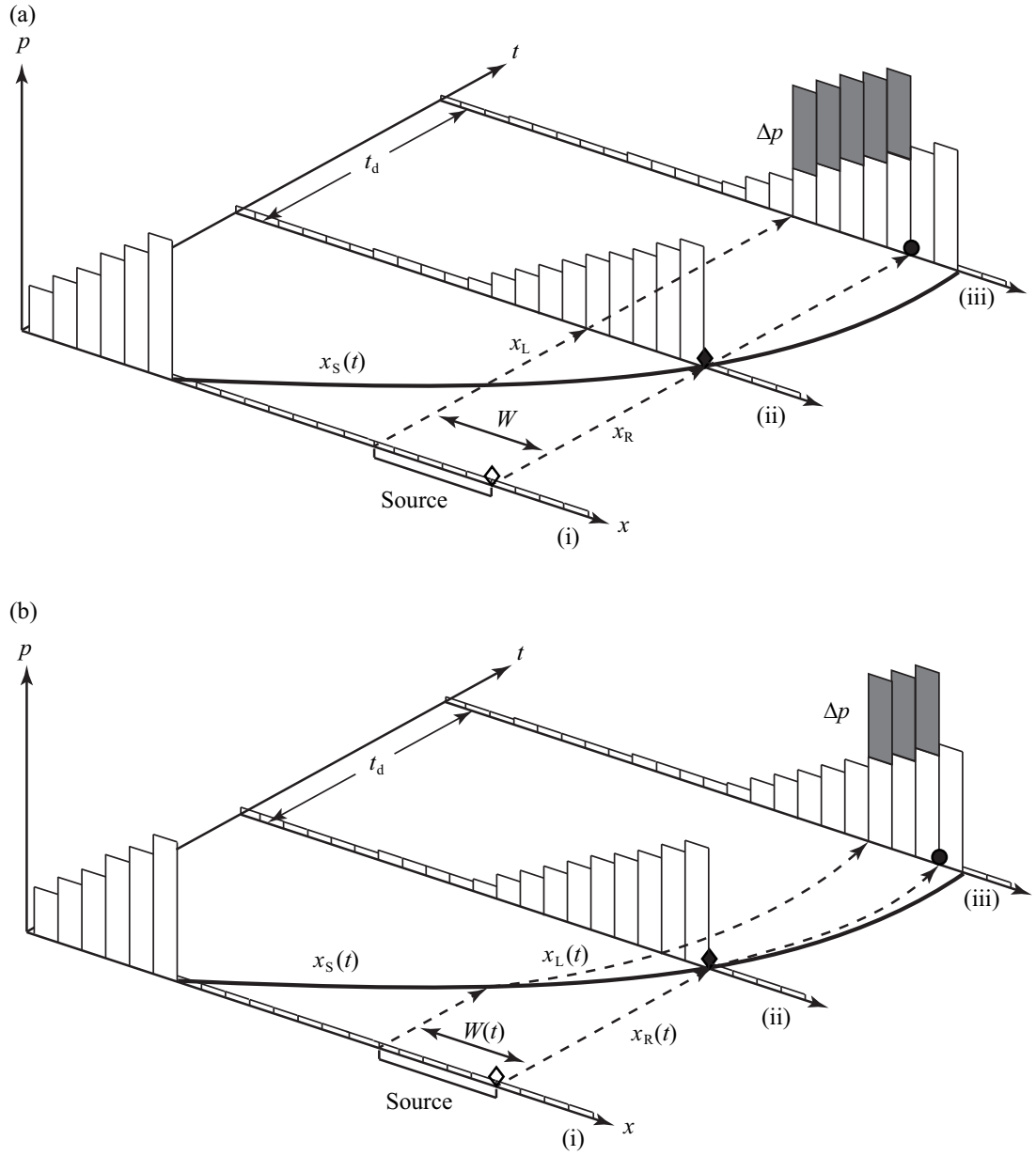

Figure 2.2: Schematic of the numerical implementation of the energy release process and source tracking algorithm for (a) lab-fixed and (b) convected discrete sources at three different moments: (i) before the arrival of the leading shock wave $x_s(t)$, (ii) the source being shocked marking the onset of delay period, and (iii) the source instantaneously releasing energy.

tions with a source term $\mathbf{S}$ in the lab-fixed reference frame,

$$\frac{\partial \mathbf{U}}{\partial t} + \frac{\partial \mathbf{F}(\mathbf{U})}{\partial x} = \mathbf{S}(\mathbf{U}) \tag{2.3}$$

where the conserved variable $\mathbf{U}$ and the convective flux $\mathbf{F}$ are, respectively,

$$\mathbf{U} = \begin{pmatrix} \rho \\ \rho u \\ \rho e \end{pmatrix} \qquad \mathbf{F}(\mathbf{U}) = \begin{pmatrix} \rho u \\ \rho u^2 + p \\ (\rho e + p)u \end{pmatrix} \tag{2.4}$$

In the above equations, $e = p/(\gamma - 1)\rho + u^2/2$ is the non-dimensional specific total energy.

For the cases where energy is deposited instantaneously, the energy is incorporated in the energy balance equation via $\mathbf{S}(\mathbf{U})$ as follows,

$$\mathbf{S}(\mathbf{U}) = \begin{pmatrix} 0 \\ 0 \\ \sum_n \Delta p \delta(t_{\mathrm{i},n} - t_{\mathrm{d}}) \mathrm{H}(x - x_{\mathrm{L},n}) \mathrm{H}(x_{\mathrm{R},n} - x) \end{pmatrix} \tag{2.5}$$

where δ and H denote δ- and Heaviside functions, respectively, and n is the index of each discrete source of energy. The positions of the left and right edges of the n-th source are denoted as $x_{\mathrm{L},n}$ and $x_{\mathrm{R},n}$, respectively. The two Heaviside functions, i.e., $\mathrm{H}(x - x_{\mathrm{L},n})$ and $\mathrm{H}(x_{\mathrm{R},n} - x)$, describe that the energy is deposited in the volume occupied by the n-th source. Note that, in the case with extremely discrete sources, where $(x_{\mathrm{R},n} - x_{\mathrm{L},n}) = W$ tends to 0, the spatially discrete sources approach the limit of a δ-function in space, i.e., $\lim_{W \to 0} \mathrm{H}(x - x_{\mathrm{L},n}) \mathrm{H}(x_{\mathrm{R},n} - x)/W = \delta(x - x_n)$. For convected sources, the fluid elements marking the left and right edges of the n-th source move at their corresponding

particle velocities, hence, their motions are governed by the following equations,

$$\frac{\mathrm{d}x_{\mathrm{L},n}}{\mathrm{d}t} = u\left(x_{\mathrm{L},n}, t\right) \quad \text{and} \quad \frac{\mathrm{d}x_{\mathrm{R},n}}{\mathrm{d}t} = u\left(x_{\mathrm{R},n}, t\right) \tag{2.6}$$

A variable, $t_{\mathrm{i},n}$, with its initial value 0, is introduced in Eq. 2.5 to measure the time elapsed since the source has been shocked. The time evolution of $t_{\mathrm{i},n}$ is described by the following equation,

$$\frac{\mathrm{d}t_{\mathrm{i},n}}{\mathrm{d}t} = \mathrm{H}\left(p\left(x_{\mathrm{R},n}, t\right) - p_0\right) \tag{2.7}$$

The Heaviside function indicates that the measurement of $t_{\mathrm{i},n}$ starts once the local pressure at the right edge of the source becomes incrementally greater than the initial pressure of the medium.

2.1.2 Numerical methodology

Two independently-written, one-dimensional, finite-volume Euler codes were used in this study. One of them was based on a fixed (non-adaptive) uniform grid. This solver, however, encountered computer memory limitations as the sources were progressively made more discrete, due to the requirement for a minimum number of computational cells within each source to properly resolve all wave phenomena induced by energy release (see discussion below). For this reason, a second code using adaptive mesh refinement was used to both extend the results into the limit of highly spatially discrete sources and verify the results of the fixed-grid code. Both codes solve the one-dimensional Euler equations using the MUSCL-Hancock TVD node-centered Godunov-type finite-volume scheme [38] with an exact Riemann solver and the van Leer non-smooth slope limiter. The scheme is of second order of accuracy in space and time on smooth solutions.

In the adaptive code, the background (initial) grid is also uniform. Grid adaptation is

performed at each time step via hierarchical h-refinement. Each refinement level reduces the local grid step by two times. The number of refinement levels is determined from the requirement of having the smallest grid step corresponding to the desired number of grid nodes within the energy source (see discussion below). The refinement/coarsening sensor is based on normalized second derivatives of density and pressure. Prior to energy release via pressure modification for a source, the grid is refined in the vicinity of the source, regardless of the sensor values in the region, so that the energy release and subsequent induced wave motion would be always resolved on the finest mesh. The data structure and adaptation procedure of the adaptive code were adopted, with suitable simplification, from the two-dimensional unstructured Euler code described by Satio *et al.* [39] to a one-dimensional code. Preliminary numerical trials demonstrated that simple linear solution interpolation used in the code [39] when inserting a new node led to significant (of the order of 5%) error in wave speeds when long distance propagation typical for the problem under consideration was simulated. For this reason, node insertion and deletion procedures were modified to be fully conservative, i.e., the conservation of mass, momentum, and energy were strictly enforced when assigning gasdynamic parameters at a newly inserted node or removing a node.

In both fixed and adaptive mesh refinement codes, the instantaneous energy deposition by each discrete source after a finite delay period is implemented as follows. The trajectory of the leading shock front, $x_{\rm s}(t)$, is tracked in the simulations by finding the location where p first increases to 1.01 from its upstream initial state $p_0 = 1$ at each time step. A discrete source is considered as being shocked once the leading shock passes the right edge of the space occupied by this source, i.e., the pressure at right edge of the source $p\left(x_{\rm R}, t\right)$ becomes greater than p_0 (here and below the source index n is omitted). The time elapsed since the source has been shocked, $t_{\rm i}$, is measured by numerically integrating Eq. 2.7. The

algorithm of delay time update at each time step Δt is formulated as follows,

$$t_{\mathrm{i}}^{t+\Delta t} = t_{\mathrm{i}}^{t} + \Delta t_{\mathrm{i}}, \quad \text{where} \quad \Delta t_{\mathrm{i}} = \begin{cases} 0, & p\left(x_{\mathrm{R}}, t\right) = p_0 \\ \Delta t, & p\left(x_{\mathrm{R}}, t\right) > p_0 \end{cases} \tag{2.8}$$

Once t_{i} reaches t_{d}, the simulation is stopped before advancing to the next time step, and energy is deposited within the space occupied by this triggered source, i.e., between the left and right edges of this source ($x_{\mathrm{L}} \leqslant x \leqslant x_{\mathrm{R}}$), via increasing the pressure by Δp,

$$p_{\mathrm{updated}}\left(x, t\right) = p\left(x, t\right) + \Delta p \quad \text{at} \quad t_{\mathrm{i}} = t_{\mathrm{d}} \tag{2.9}$$

with the value of Δp being given by Eq. 2.2. Unlike in the scenario of fixed sources, the location and volume occupied by a convected source change with time. The trajectories of the fluid elements marking the right and left edges of each convected source, i.e., $x_{\mathrm{R}}(t)$ and $x_{\mathrm{L}}(t)$, respectively, are tracked via numerical integration of the corresponding particle paths described by Eq. 2.6 using a Lagrangian approach,

$$\begin{aligned} x_{\mathrm{R}}^{t+\Delta t} &= x_{\mathrm{R}}^{t} + \Delta t \cdot u_{\mathrm{R}}^{t} \\ x_{\mathrm{L}}^{t+\Delta t} &= x_{\mathrm{L}}^{t} + \Delta t \cdot u_{\mathrm{L}}^{t} \end{aligned} \tag{2.10}$$

With this source tracking algorithm, the code is able to add pressure into the space occupied by a convected source at the moment when it releases energy after the delay period. The numerical implementation of energy release and source tracking algorithm for lab-fixed and convected sources is illustrated in Fig. 2.2.

The length of the entire simulated problem is over 100 spatial units, i.e., containing more than 100 discrete sources. In order to make the simulation time-efficient, the computation, at every time step, is only performed in a window enclosing the leading wave

complex in a laboratory-fixed reference frame, instead of the entire simulation domain. A minimum eight-unit-wide window (i.e., containing 8 sources) is necessary to capture all of the dynamics contributing to the propagation of the leading wave front for the longest delay times considered in this study. Once the leading front reaches the end of this computational window, the window frame (i.e., left and right boundaries) advanced by one spatial unit while maintaining the same width of the domain. A transparent boundary condition is applied on both boundaries of the computational window [38]. In order to rule out any possible influence of the boundary conditions, a 10-unit-wide window was used in all the simulations reported below. As the numerical resolution is increased from 50 to 200 computational cells within a discrete source, the simulation results did not show any significant difference. The results reported in this paper were all performed with a numerical resolution of 100 computational cells per source.

2.1.3 Results

The results of a sample calculation are shown in Fig. 2.3, showing the pressure profile of the computational domain for a simulation of Scenario 1 with the following parameters: $\Gamma = 0.05$, $\tau = 1.5$, $Q = 50$, and $\gamma = 5/3$. Both early time (the first 3 sources) and later time (after the triggering of 280 sources) are shown in parts (a) and (b), respectively, and symbols indicate the location and status of the sources (i.e., unshocked, shocked with delay time elapsing, and energy released). The local shock dynamics following the initial release of energy resembles a classical blast wave profile. At later times (Fig. 2.3(b)), a large number of saw-toothed waves, which are residual, decaying blast waves from earlier sources, can be seen superimposed upon the flow field. Figure 2.4 shows x-t diagrams constructed from simulation results ($\Gamma = 0.05$, $\tau = 0.1$, $Q = 50$, $\gamma = 1.1$, and sources held fixed), with the shading indicating pressure in the flow field obtained over the region

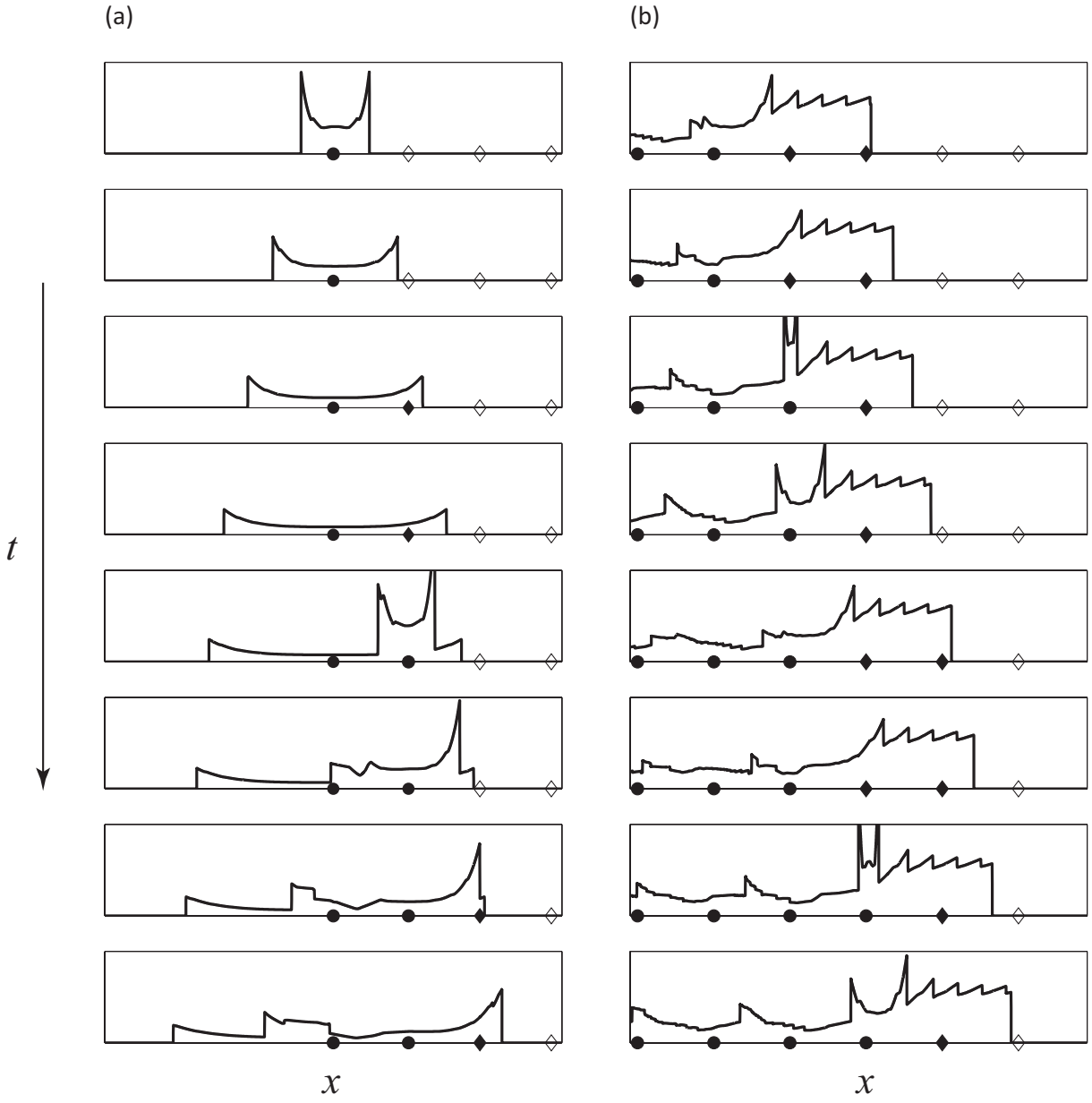

Figure 2.3: Pressure profiles showing evolution of flow field with instantaneous release of source energy ($\Gamma = 0.05$, $\tau = 1.5$, $Q = 50$, $\gamma = 5/3$, and lab-fixed sources): (a) triggering of the first 3 sources and (b) later time evolution after triggering 280 sources. The symbols plotted on the horizontal axis indicate the location of energy sources. An open diamond represents a source before being shocked, a solid diamond – a source undergoing delay period after being shocked, and a solid circle – a source after releasing its energy.

from the 280^{th} to the 284^{th} source. The dark V-shaped regions in the pressure fields are the blast waves generated by the energy release of the sources, propagating both forward and backward in the flow. The forward propagating blast generated by a newly triggered source catches up and accelerates the leading shock ahead of it. After the leading shock has traveled a sufficiently long distance, the process of new sources releasing their energy and the forward propagating blast waves catching up to the leading shock becomes nearly periodic. In Fig. 2.4(b), the spatial coordinates are transformed into a reference frame moving at the average velocity of the leading shock, i.e., $x' = x - V_{\text{avg}}t$. Right-running characteristics are constructed in Fig. 2.4(b) by integrating an ODE describing the path along which acoustic signals move through the domain at the particle velocity (with respect to the wave-attached frame) plus the local sound speed. The use of x-t diagrams and characteristics analysis was first explored by McVey and Toong [40] and recently by Kasimov and Stewart [41] and Leung *et al.* [42] to illustrate the physical mechanisms governing the instabilities in hypersonic exothermic flow and pulsating detonations, respectively. This construction of the x-t diagram is a post-processing exercise performed upon the already-computed solution. In Fig. 2.4(b), there is a characteristic (plotted as a thickened line) such that the characteristics upstream (on the right) of it can eventually reach the leading shock, while those downstream (on the left) can never reach the leading shock. This limiting characteristic is known as the separatrix, such that only the flow field upstream of it is able to influence the shock front. It can be clearly seen in Fig. 2.4(b) that the separatix oscillates around a location which is significantly downstream from the loci of sources releasing energy.

Figure 2.5(a) shows the evolution of the instantaneous velocity, V_{inst}, normalized by V_{CJ}, at which the leading wave front propagates over the first 8 lab-fixed sources for the case of $\Gamma = 0.05$, $\tau = 0.01$, $Q = 50$, and $\gamma = 1.1$. As described in Sec. 2.1.2, the trajectory of the leading shock front is tracked in the simulations. V_{inst} as a function of x_{s} can thus

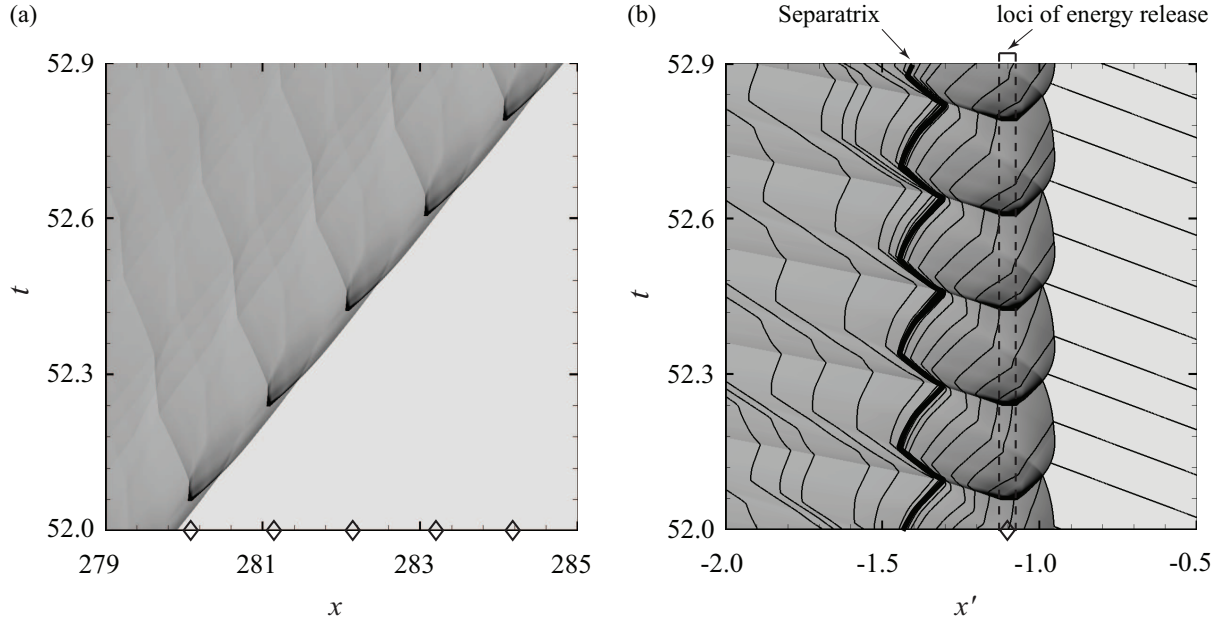

Figure 2.4: x-t diagram of flow field in (a) lab-fixed and (b) wave-fixed reference frame ($\Gamma = 0.05$, $\tau = 0.1$, $Q = 50$, $\gamma = 1.1$, and lab-fixed sources). The curves in (b) are right-running characteristics generated by integrating the trajectory of an acoustic wave through the already-computed flow field, and the thickened curve indicates the separatrix. The symbols plotted on the horizontal axis indicate the location of energy sources.

be obtained by numerically differentiating $x_s(t)$ using a central difference scheme. V_{inst} exhibits large fluctuations as the successive sources are triggered and the blast waves they drive reach the leading shock front. Each time a blast wave reaches and merges with the shock front, V_{inst} is brought to a peak value, and then, decays to a local minimum velocity just before the next blast wave reaches the front. In Fig. 2.5(a), it can be observed that both the local minimum and maximum V_{inst}, just before and after the instant of the next blast wave reaching the front respectively, monotonically increase to steady values as the sources are successively triggered. Also shown in Fig. 2.5(a) is the prediction of a simple heuristic model that is based on the classic similarity solution of Taylor and Sedov for planar blast waves, the concept of energy partitioning of new source energy released at the blast front, and displacement of the flow field resulting from the residual influence of prior sources; see the Appendix for a complete development of this model.

With $x_s(t)$ obtained from the simulation results, the average velocity at which the leading wave front travels from one source to the next can be calculated. Figure 2.5(b) shows the evolution of the source-to-source average wave velocity, $V_{avg,source}$, as a function of the distance traveled by the leading wave front. The results shown in this figure are for the cases of various values of discreteness ($\Gamma = 0.001$ to continuous), $\tau = 0.01$, $Q = 50$, and $\gamma = 1.1$ over 100 lab-fixed sources. For all values of Γ, $V_{avg,source}$ gradually increases and converges to a nearly constant value. A plateau value of $V_{avg,source}$ indicates that the dynamics of the shock front triggering the energy release of the sources and the resulting blast waves reaching and supporting the shock front have reached a quasi-periodic state with a constant time interval between the trigger of subsequent sources. As the sources become more discrete ($\Gamma \to 0.001$), the plateau $V_{avg,source}$ converges to a value that is 15% in excess of the CJ velocity of the equivalent homogeneous system (note the horizontal line indicating CJ velocity) for $\gamma = 1.1$. The distance required for $V_{avg,source}$ to reach a quasi-steady value decreases from the order of 100 for continuous energy source to that in

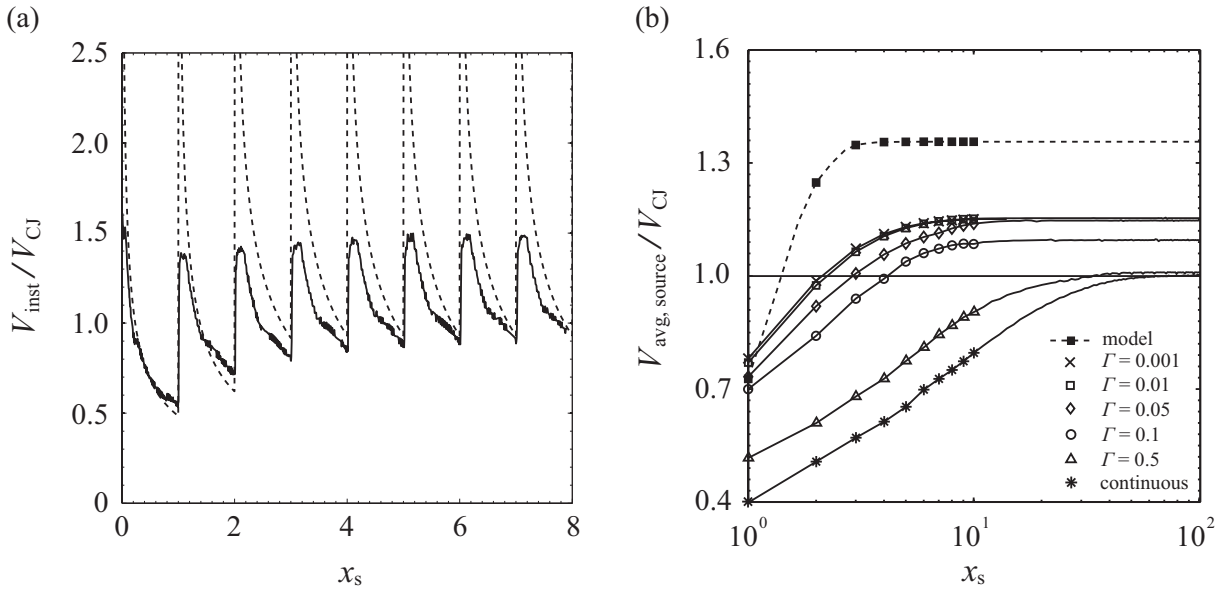

Figure 2.5: The history of (a) the instantaneous wave velocity normalized by $V_{\rm CJ}$ over the first 8 lab-fixed sources for the case of $\Gamma = 0.05$, $\tau = 0.01$, $Q = 50$, and $\gamma = 1.1$, and (b) the source-to-source average wave velocity over 100 lab-fixed sources for the cases of $\Gamma = 0.001$ to 1, $\tau = 0.01$, $Q = 50$, and $\gamma = 1.1$ as a function of the leading shock position $x_{\rm s}$. The heuristic model prediction is plotted as a dashed curve. In (b), the symbols are plotted only for the first 10 sources.

the order of 10 for $\Gamma = 0.001$. The heuristic model (see the Appendix) prediction of how $V_{\rm avg,source}$ evolves as sources are triggered successively is also shown in Fig. 2.5(b). In order to show the results for a large range in the value of source discreteness, the simulation results shown in Fig. 2.5(b) are those obtained by using the adaptive mesh refinement code.

The following subsections systematically study the average velocity of the wave as the various parameters in the model are varied. The influence of the source scenarios (lab-fixed *vs.* convected sources) and energy deposition mechanism (instantaneous deposition *vs.* single-step Arrhenius kinetics) is also investigated. All average velocities, subsequently reported in this paper and denoted as $V_{\rm avg}$, were measured after the leading shock front has reached a quasi-steady value. The length of the simulation domain, i.e., the total

number of discrete sources, over which the detonation wave needs to propagate to reach a quasi-periodic state, varied approximately from 20 to 100 as Γ increases from 0.001 to 1. In the simulations using the fixed, uniform grid code, which are the cases with relatively less discrete sources ($\Gamma \geqslant 0.05$), the leading front propagated through 300 sources, and the average velocities calculated over the last 100, 50, or 10 sources differed by less than 0.1%. Hence, for the simulations using the fixed, uniform grid code, average velocity over the last 50 sources, i.e., from the 250^{th} to 300^{th} source, is reported in the following subsections of Sec. 2.1.3 as V_{avg}. For the cases with extremely discrete sources ($\Gamma \leqslant 0.01$) which were only simulated using the adaptive mesh code, the length of the simulation domain cannot be extended beyond 30 sources due to computational time and memory limits. This length is, however, sufficient for the wave propagation to reach a quasi-periodic state as shown in Fig. 2.5(b). Hence, for those cases, it is sufficient to report the average velocity over the last 10 sources as V_{avg}. All values are normalized by the CJ velocity of the equivalent homogenized media.

2.1.3.1 Fixed sources with instantaneous energy deposition

Discreteness

The effect of the spatial concentration of the sources, i.e., the effective discreteness parameter Γ, which is the same as the initial discreteness in this scenario with fixed sources ($\Gamma = \Gamma_{\text{init}} = \widetilde{W}_{t=0}/\widetilde{L}$), on the average shock front velocity (normalized by CJ velocity) is reported in Fig. 2.6(a). For these calculations, the value of Q was held constant at 50, the delay time was a constant $\tau = 0.01$, and the sources were assumed to remain fixed after the passage of the shock. Note that in all simulations, as the width of the source was expanded to fill the entire space between sources ($\Gamma \to 1$), the average wave velocity converged to the CJ velocity (to within 0.5%). Also note that in this limit, the energy of each source is

still released instantaneously, only now there is no gap between subsequent sources. The fact that the CJ velocity is recovered in the limit of homogeneous energy released in a piecewise continuous manner is good confirmation in the overall implementation of this model.

As the sources are made progressively more discrete by concentrating them in space, an increasing deviation in the average velocity away from the CJ solution is observed. For $\gamma = 5/3$, the deviation from CJ reaches a plateau value of $V_{\rm avg}/V_{\rm CJ} = 1.025$ as Γ decreases below 0.2. For lesser values of γ, greater deviations from CJ are observed and the deviation continues to increase as the sources are made increasingly discrete ($\Gamma \to 0$). For the cases with highly discrete sources, i.e., $\Gamma < 0.05$, the numerical code with a fixed grid cannot adequately resolve the sources with sufficient resolution (100 computational cells per source) due to computer memory limitations, motivating the use of the adaptive refinement code. The uniform, fixed grid and adaptive mesh refinement codes exhibit good agreement, as seen by comparing the solid and open symbols in Fig. 2.6(a), respectively, providing confidence that the results of this study, and the observed super-CJ velocities in particular, are not an artifact of the particular solver used.

For the case of $\gamma = 1.1$, the average wave speed achieves a value of 15% greater than CJ (i.e., $V_{\rm avg}/V_{\rm CJ} = 1.15$) as the sources become concentrated into 5% of the available volume (i.e., discreteness $\Gamma = 0.05$). This is the greatest deviation away from the CJ solution observed in this study. The effect of the ratio of specific heats is explored further in the next section. As the sources are made progressively more discrete ($\Gamma < 0.05$) in the $\gamma = 1.1$ case, the average wave speed appears to reach a plateau value. We interpret this plateau as an asymptotic limit in spatial discreteness, and we explore the concept of an asymptotic limit of δ-function-like sources further in the Appendix.

Specific heat ratio

The average wave speed measured for quasi-periodic propagation is reported as a function of the specific heat ratio γ in Fig. 2.6(b). For these simulations, the value of heat release was fixed at $Q = 50$, the delay time at $\tau = 0.01$, and the discreteness was fixed at $\Gamma = 0.05$. From Fig. 2.6(a), this value of the discreteness parameter is seen to be sufficiently small that the wave is propagating in the asymptotic limit of highly discretized sources, such that decreasing the value of Γ further will no longer influence the result. The average velocity (as normalized by the CJ velocity) is seen to increase as the value of γ is decreased. Also shown in this figure is the result of the heuristic model developed in the Appendix. The qualitative agreement between the model and the simulations will provide a basis to explain the dependence on γ, as discussed in Sec. 2.1.4.

Heat release

The value of the heat release Q was varied in a way such that the Mach number of the CJ detonation in the homogenous media remained between values of $M_{\rm CJ} = 4$ and $M_{\rm CJ} = 10$, in order to be representative of real detonable mixtures. This resulted in the value of Q varying between 50 and 250 for $\gamma = 1.1$ and between 10 and 60 for $\gamma = 5/3$. The average wave speed measurements of these simulations are shown in Fig. 2.6(c). The observed wave speed normalized by the CJ speed is not particularly sensitive to the heat release of the mixture.

Delay time

The assumption of a fixed delay time, which is not influenced by the strength of the shock wave that triggers the source or the post-shock thermodynamic states, may be viewed as an unrealistic assumption in the model. Thus, it is important to examine

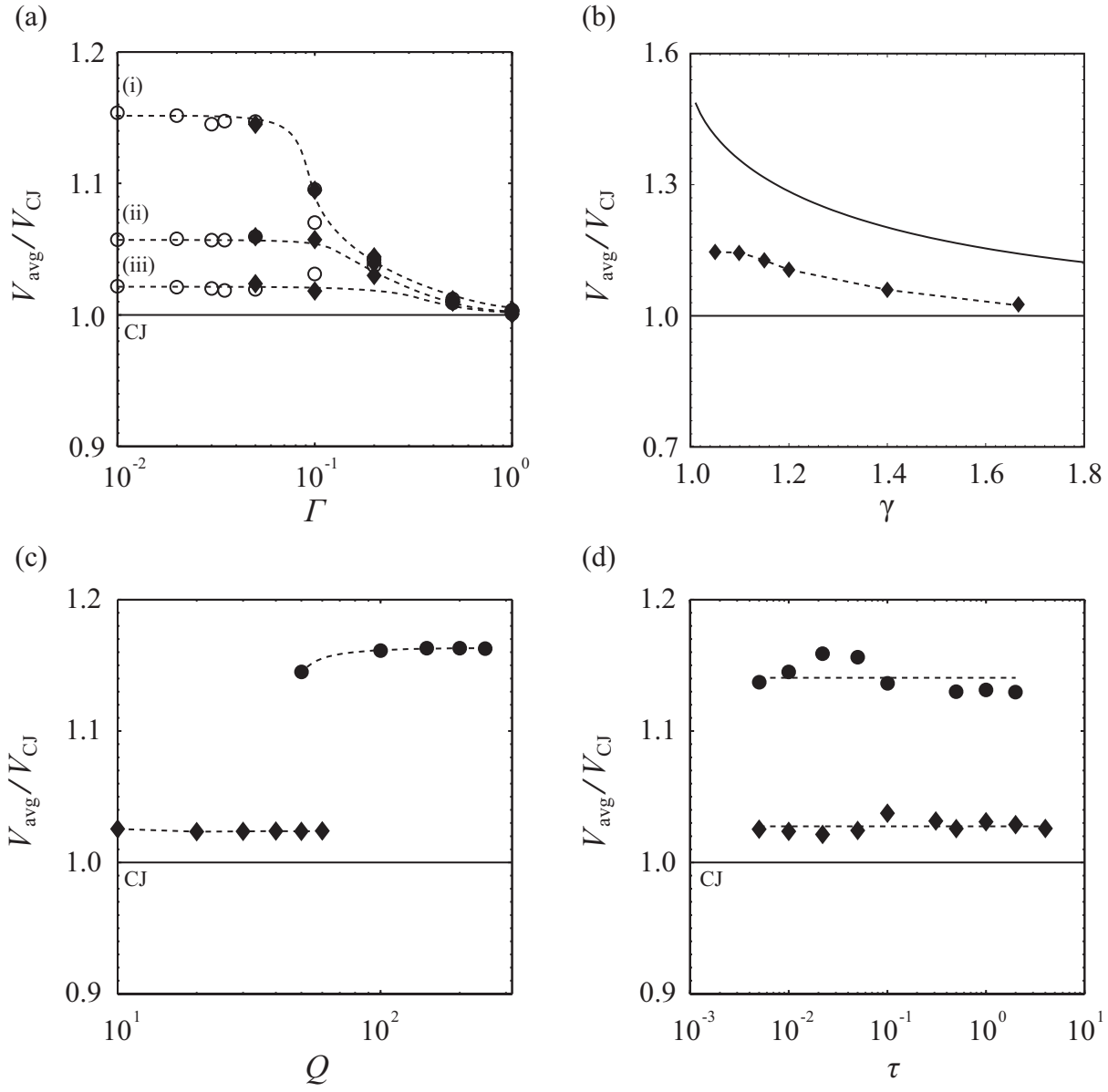

Figure 2.6: Simulation results of the average wave velocity normalized by the CJ velocity as a function of (a) effective discreteness, (b) specific heat ratio, (c) heat release, and (d) delay time with lab-fixed sources. Simulation data obtained using the adaptive refinement code are plotted as open circles. In (a), the simulation results with $\tau = 0.01$, $Q = 50$, and $\gamma = 1.1$, 1.4, and 5/3 are labeled (i), (ii), and (iii), respectively. In (b), the simulation results with $\Gamma = 0.05$, $\tau = 0.01$, and $Q = 50$ are plotted as diamonds and compared to the heuristic model prediction plotted as a solid curve (see the Appendix). In (c), the simulation results with $\Gamma = 0.05$ and $\tau = 0.01$ are plotted as circles and diamonds for $\gamma = 1.1$ and 5/3, respectively. In (d), the simulation results with $\Gamma = 0.05$ and $Q = 50$ are plotted as circles and diamonds for $\gamma = 1.1$ and 5/3, respectively.

the influence of varying the delay time τ in separate calculations. The effect of varying the delay time, which remained fixed for each simulation, is reported in Fig. 2.6(d) for discreteness $\Gamma = 0.05$ and $Q = 50$. Note that, as the delay time is varied from $\tau = 0.004$ to $\tau = 3$, the observed average wave speed does not exhibit any overall trend. A small deviation is observed around $\tau = 0.03$ and $\tau = 0.1$ for $\gamma = 1.1$ and 5/3, respectively, however, we are unable to attribute any significance to this particular result.

2.1.3.2 Convected sources with instantaneous energy deposition

The simulations presented so far are for the case of sources that remain spatially fixed after the passage of the shock. In order to examine the influence of this assumption, a series of simulations were performed in which the energy source is embedded in the medium through which the shock wave propagates, and following the passage of the shock wave, is convected along with the flow. Since a convected source is compressed by the shock wave, the width of a source when it releases energy after a finite delay time $t_{\rm d}$ is smaller than its initial width before the passage of the shock. Hence, the effective discreteness ($\Gamma = \widetilde{W}_{t_{\rm i}=t_{\rm d}}/\widetilde{L}$) is smaller than that in the initial distribution of sources ($\Gamma_{\rm init}$), and this effective discreteness is used here to compare these results with those from Sec. 2.1.3.1 in Fig. 2.7. The simulations were performed with $Q = 50$, $\tau = 0.01$, and $\gamma = 1.1$ and 5/3. The result of an increasing average wave speed for the cases of convected sources, as the value of $\Gamma \to 0$, coincides with that for the cases of fixed sources. For Γ approximately below 0.1, the average wave speed reaches a plateau value of 15% and 3% greater than the CJ value for $\gamma = 1.1$ and 5/3, respectively.

2.1.3.3 Analysis

The fact that a spectrum of quasi-periodic solutions that propagate at average speeds significantly greater than the CJ speed (i.e., super-CJ solutions) when the source energy

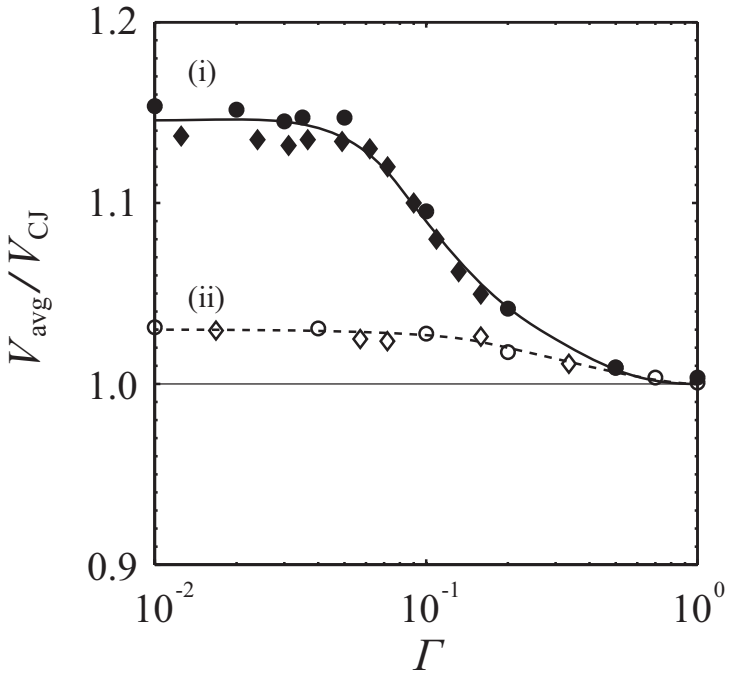

Figure 2.7: Simulation results of the average wave velocity normalized by the CJ velocity as (a) a function of effective discreteness Γ for the cases of instantaneously triggered lab-fixed (circles) and convected (diamonds) sources with $\tau = 0.01$, $Q = 50$, and (i) $\gamma = 1.1$ (solid symbols and trend line) and (ii) $\gamma = 5/3$ (open symbols and dashed trend line).

is sufficiently concentrated in space is a result that could be met with a large degree of skepticism, given the considerable success of the CJ solution in comparison with experiments. In order to provide an explanation of this finding, the results of select simulations reported in the prior section were analyzed using the conventional pressure/specific volume (p-v) representation of thermodynamic states. Following the approach developed by White [43], Lee and Radulescu [9], Radulescu *et al.* [4], and Sow *et al.* [44], the flow field of the wave propagating in a discrete source detonation will be analyzed in a moving reference frame and the flow at each point in the domain will be averaged over time. This will enable the average structure of the wave to be compared to the classical structure of the ZND model of a detonation, as visualized in the p-v diagram. The analysis shown in this section was only performed for the simulation results for the cases with instantaneously triggered, lab-fixed sources.

Similar to the analysis performed by Radulescu *et al.* [4], the averaging is done in a reference frame moving at the average velocity of the wave calculated from the 250^{th} to the 300^{th} source. Thus, in the moving reference frame, the spatial coordinate and particle velocity are transformed as $x' = x - V_{\text{avg}}t$ and $u' = u - V_{\text{avg}}$, respectively. For convenience, u denotes the particle velocity with respect to the moving frame in this section.

A simple time averaging, or Reynolds averaging procedure, is then applied to density and pressure (and other quantities in Eqs. 2.13-2.17) as follows,

$$\bar{\rho}\left(x'\right) = \frac{1}{t_2 - t_1}\int_{t_1}^{t_2} \rho\left(x', t\right) \mathrm{d}t \tag{2.11}$$

$$\bar{p}\left(x'\right) = \frac{1}{t_2 - t_1}\int_{t_1}^{t_2} p\left(x', t\right) \mathrm{d}t \tag{2.12}$$

where t_1 and t_2 indicate the starting and ending time of the period, respectively, over which ρ and p are averaged. The bar "–" indicates time-averaged variables. Favre averaging

(i.e., density weighted averaging) is applied to particle velocity and specific energy as follows,

$$u^* = \frac{\overline{\rho u}}{\bar{\rho}} \text{ and } u = u^* + u'' \tag{2.13}$$

$$e^* = \frac{\overline{\rho e}}{\bar{\rho}} \text{ and } e = e^* + e'' \tag{2.14}$$

where superscripts $*$ and $''$ indicate Favre-averaged variables and fluctuating quantities, respectively. The average structure of the wave is therefore governed by the one-dimensional, stationary Favre-averaged Euler equations as follows,

$$\frac{\partial}{\partial x'}\left(\bar{\rho} u^*\right) = 0 \tag{2.15}$$

$$\frac{\partial}{\partial x'}\left(\bar{\rho} u^{*2} + \bar{p} + \overline{\rho u''^2}\right) = 0 \tag{2.16}$$

$$\frac{\partial}{\partial x'}\left(\bar{\rho} e^* u^* + \bar{\rho}\left(e'' u''\right)^* + \overline{p u}\right) = 0 \tag{2.17}$$

For an averaged fluid element traversing the wave structure, its averaged mass and momentum are conserved according to,

$$\overline{M}^2 = \frac{\bar{p} - 1 + f}{\gamma\left(\bar{v} - 1\right)} \tag{2.18}$$

where $\bar{v} = 1/\bar{\rho}$ is the averaged specific volume, $\overline{M} = V_{\text{avg}}/c_0$ is the Mach number of the average wave velocity, and $f = \overline{\rho u''^2}$ is the Reynolds stress, which measures the intensity of fluctuations in momentum. Note that when $f = 0$, i.e., there is no fluctuation in fluid momentum over time, Eq. (2.18) reverts to the ideal Rayleigh line that a fluid element traversing a one-dimensional steady detonation structure is expected to follow.

The average sound speed, which is assumed to be independent of the intensity of

fluctuation, can be calculated as,

$$c^* = \sqrt{\frac{\gamma \bar{p}}{\bar{\rho}}} \tag{2.19}$$

The sonic point in the one-dimensional averaged wave structure is located at the position where $u^* + c^* = 0$. The importance of using a mean steady detonation profile to determine the location of the effective sonic plane was highlighted by Lee and Radulescu [9].

Figure 2.8 shows the simulation results for the case of continuous (i.e., $\Gamma = 1$) lab-fixed energy sources, $Q = 50$, $\tau = 0.1$, and $\gamma = 1.1$ analyzed using the Favre averaging approach and p-v representation of thermodynamic states. Note that while the source energy is uniform throughout the medium, it is still released in piecewise-continuous segments with width $\widetilde{L}$, which is non-dimensionalized to a value of unity when reported here. In Fig. 2.8(a), the evolution of the flow field is plotted as a grayscale contour of pressure in a x'-t diagram. Figure 2.8(b) shows the spatial profile of f in the wave-attached reference frame, which measures the intensity of mechanical fluctuations around the Favre-averaged value in the flow field, normalized by Q. The one-dimensional steady structure of the time-averaged pressure $\bar{p}$ in the wave-attached reference frame is plotted in Fig. 2.8(c) below the x'-t diagram. The thermodynamic path taken by a fluid element traversing this one-dimensional steady, averaged wave structure is plotted in a p-v diagram as shown in Fig. 2.8(d). The location of the sharp increase in $\bar{p}$ from the upstream initial state to its peak value occurs in the region between the leading shock and the loci of the source releasing energy in the x'-t diagram. The peak in the averaged pressure matches the von Neumann pressure, i.e., the downstream pressure behind a normal shock of strength M_{CJ}, shown in Fig. 2.8(d). As shown in Fig. 2.8(a), the $u + c$ characteristics near the separatrix are quasi-straight lines with slight wiggles as they pass through backward-running shock waves and contact surfaces.

Comparing Fig. 2.8(a) and (c), the sonic point in the averaged profile is found to match

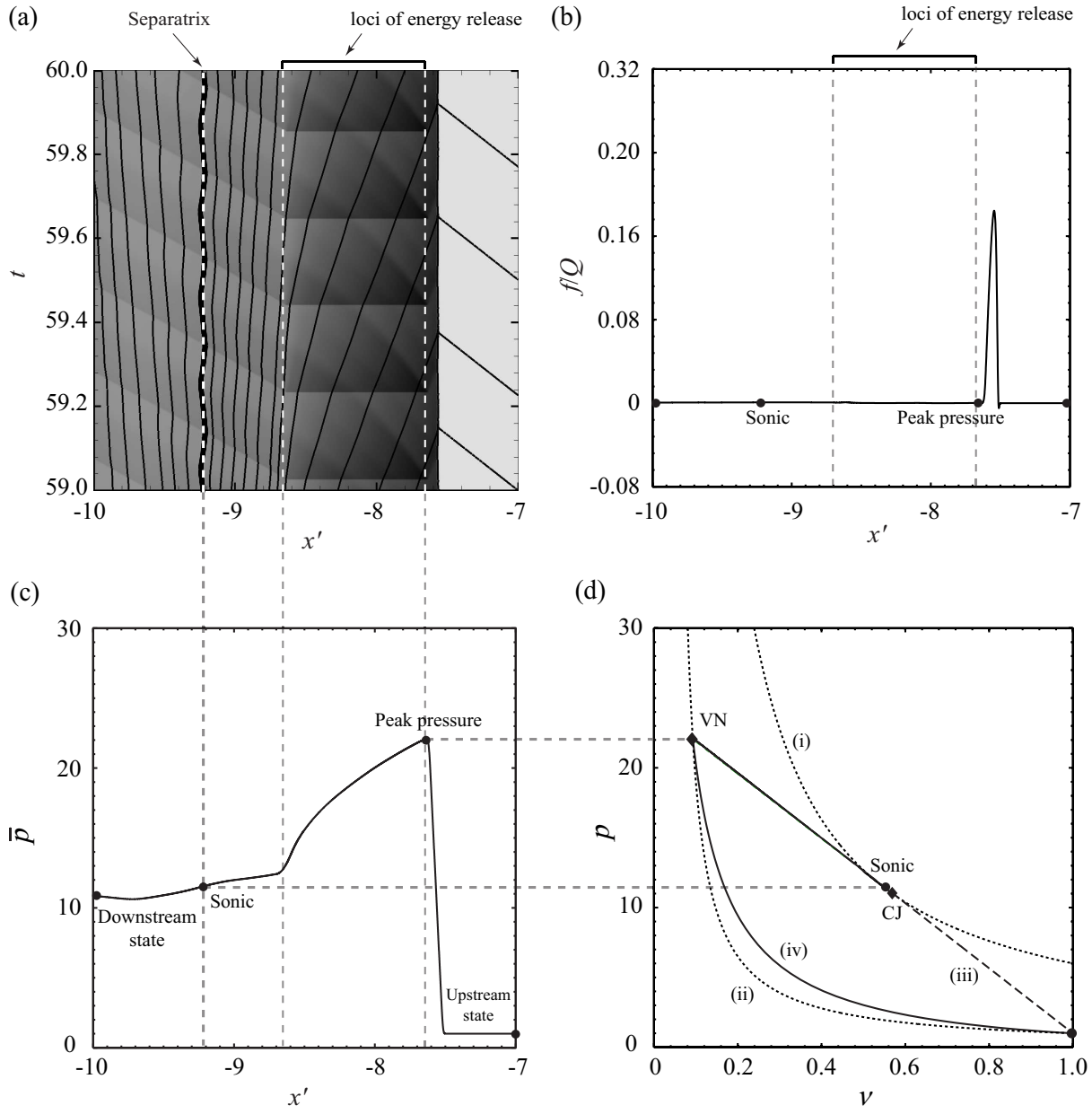

Figure 2.8: For the case of continuous (i.e., $\Gamma = 1$) lab-fixed energy sources, $Q = 50$, $\tau = 0.1$, and $\gamma = 1.1$, (a) pressure contour plotted as a x'-t diagram showing the evolution of the flow field and right-running characteristics, (b) the spatial profile of the intensity of mechanical fluctuation f normalized by Q, (c) the one-dimensional steady structure of the time-averaged pressure $\bar{p}$ in the wave-attached reference frame, and (d) the p-v representation of the one-dimensional averaged wave structure. In (d), curve (i) is the equilibrium Hugoniot curve of complete energy release $Q = 50$, curve (ii) is the Hugoniot curve of zero energy release $Q = 0$, curve (iii) is the ideal Rayleigh line corresponding to a leading shock strength of $M_{\rm CJ}$, and curve (iv) is the p-v thermodynamic path taken by a fluid element traversing the one-dimensional averaged wave structure.

the trajectory of the limiting characteristic of the separatrix, which appears downstream from the loci of sources releasing energy. The thermodynamic state at this averaged sonic point nearly coincides with the CJ state of a one-dimensional steady detonation wave propagating at M_{CJ}, as seen in Fig. 2.8(d). This is consistent with the result that the $\overline{M}$ obtained from the simulation with continuous energy sources is only 0.3% greater than the M_{CJ} for the same total energy release Q. Since the CJ point is the intersection of the ideal Rayleigh line and the equilibrium Hugoniot curve of complete energy release, the averaged flow field relaxes to equilibrium at the sonic point.[1] In Fig. 2.8(b), it can be seen that mechanical fluctuation f/Q is significantly positive only in a narrow region which corresponds to the sharp increase in averaged pressure shown in Fig. 2.8(c). In Fig. 2.8(d), the averaged p-v path from the upstream initial state to the peak averaged pressure (or the von Neumann) state significantly departs from the ideal Rayleigh line corresponding to a wave speed of M_{CJ}, which can be interpreted as the fact that the mechanical fluctuation is concentrated between the shock and energy release as shown in Fig. 2.8(b). As f/Q rapidly decays to and remains at zero downstream of the location of peak averaged pressure to the sonic point, the averaged p-v path connecting the peak averaged pressure state to the sonic point coincides with the ideal Rayleigh line. In the case of continuous energy sources, despite the mechanical fluctuation caused by the interaction between the forward-running blast generated by each individual source releasing its energy and the preceding shock front, the highly unsteady wave propagation and energy deposition process has a temporal average structure that is nearly equivalent to a steady one-dimensional detonation structure with the same amount of heat release. The excellent agreement obtained between the averaged structure of the wave extracted from the simulations (with continuous energy release) and the steady ZND structure can

[1] It is important to note that, in this problem, the term "equilibrium" refers to mechanical (or hydrodynamic) equilibrium that the flow reaches at the sonic point in the classical CJ solution, rather than chemical equilibrium of a system with reversible reactions.

be taken as validation of the averaging method used in this study.

Figure 2.9 shows the simulation results for the case of highly discrete ($\Gamma = 0.05$) lab-fixed energy sources, $Q = 50$, $\tau = 0.1$, and $\gamma = 1.1$ analyzed using the Favre averaging approach and the p-v representation of thermodynamic states. As seen from Fig. 2.6(b), $\Gamma = 0.05$ approximately corresponds to the limit of discreteness where the wave velocity becomes independent of the value of Γ (i.e., making the sources even more discrete does not result in greater deviation from the CJ solution). The x'-t diagram of flow field evolution, the spatial profile of f/Q, the one-dimensional steady profile of $\bar{p}$, and the p-v diagram of the averaged wave structure are plotted in Fig. 2.9(a), (b), (c), and (d), respectively. Comparing Fig. 2.9(a) and (c), it can be found that the increase in averaged pressure from the initial state to its peak value spans over the region where the forward-running blast waves interact with the leading shock front in the x'-t diagram. As shown in Fig. 2.9(b), the maximum intensity of mechanical fluctuation is associated with wave interactions in this region.

In contrast to the continuous case (Fig. 2.8), as shown in Fig. 2.9(a), the u+c characteristics exhibit a "zig-zag" pattern as they are processed by much stronger backward-running blast waves. The trajectory of the limiting characteristic (i.e., separatrix) oscillates back and forth while its overall zig-zag pattern remains in a fixed region relative to the leading wave front over time. For this particular calculation, the sonic point found in the one-dimensional Favre-averaged wave structure coincides with the right (or upstream) end of the limiting characteristic. Similar to the continuous case, the location of the sonic point is significantly downstream from the loci of discrete sources releasing energy. For instantaneous energy deposition, this result, wherein the forward-most point of characteristic propagation corresponds the sonic point found in the averaging procedure, was verified for all cases considered.

Plotting the p-v path taken by a fluid element traversing the Favre-averaged wave

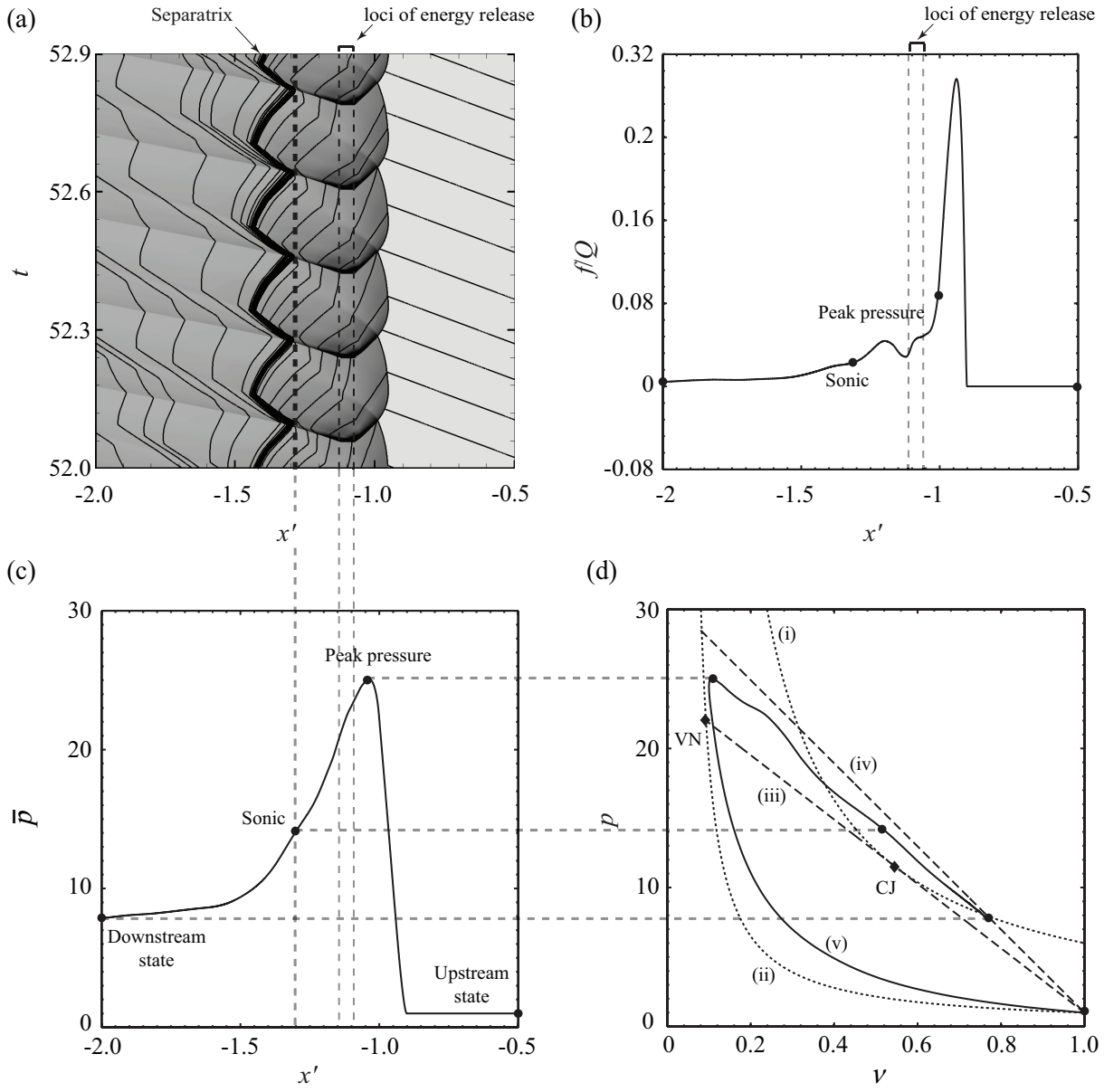

Figure 2.9: For the case of highly discrete ($\Gamma = 0.05$) lab-fixed energy sources, $Q = 50$, $\tau = 0.1$, and $\gamma = 1.1$, (a) pressure contour plotted as a x'-t diagram showing the evolution of the flow field and right-running characteristics, (b) the spatial profile of the intensity of mechanical fluctuation f normalized by Q, (c) the one-dimensional steady structure of the time-averaged pressure $\bar{p}$ in the wave-attached reference frame, and (d) the p-v representation of the one-dimensional averaged wave structure. In (d), curve (i) is the equilibrium Hugoniot curve of complete energy release $Q = 50$, curve (ii) is the Hugoniot curve of zero energy release $Q = 0$, curves (iii) and (iv) are the ideal Rayleigh lines corresponding to a leading shock strength of M_{CJ} and $\overline{M}$, respectively, and curve (v) is the p-v thermodynamic path taken by a fluid element traversing the one-dimensional averaged wave structure.

structure in Fig. 2.9(d), it can be seen that the peak averaged pressure is greater than the von Neumann pressure behind a shock of strength M_{CJ}. The averaged sonic point departs from the CJ point, and is not found on the equilibrium Hugoniot curve for $Q = 50$. Hence, equilibrium is not reached as the separatrix and the effective sonic surface in the flow field are encountered. Equilibrium is eventually attained in the far field downstream from the sonic point, as this downstream state coincides with the intersection between the equilibrium Hugoniot curve of $Q = 50$ and the Rayleigh line of a wave speed $\overline{M}$. The averaged pressure at this equilibrium state is significantly less than that of the CJ state. The $\overline{M}$ for $\Gamma = 0.05$ discrete case, which is 14% greater than M_{CJ}, is associated with a weak detonation solution. As shown in Fig. 2.9(b), the mechanical fluctuation retains a significantly positive value from the leading wave front to a location beyond the sonic point, such that the entire averaged p-v path departs from the ideal Rayleigh line based on a one-dimensional steady detonation structure. The quantity f/Q eventually decays to zero in the far field downstream, consistent with the result that the far-field downstream thermodynamic state reaches the intersection between the equilibrium product Hugoniot curve and the Rayleigh line associated with the wave speed $\overline{M}$.

2.1.4 Discussion

The results presented in this paper demonstrate that the classical CJ solution for detonation velocity breaks down and is no longer valid as the source of energy is spatially concentrated into highly discretized sources. In order to explain this result, the analysis in Sec. 2.1.3.3 shows that flow crossing the separatrix (i.e., the limiting characteristic that can influence the shock front) has not reached equilibrium due to on-going shock wave interactions that are occurring in the flow for the case of a highly discretized medium. This separatrix is the unsteady flow analog to a sonic surface, and the fact that the

flow is not in equilibrium at the effective sonic surface is a hypothesis as to why non-CJ speeds are observed. As seen in Fig. 2.9(d), the flow does eventually reach the equilibrium Hugoniot downstream of the effective sonic surface. This result suggests that the super-CJ speeds in this study are properly designated as weak detonations. Prior examples of weak detonations include so-called pathological detonations, in which competing exothermic and endothermic reactions permit the flow in the reaction zone to pass through a sonic point while in a non-equilibrium state [18, 6, 45], and ultrafast detonations [46], in which chemical reactions are sufficiently fast that significant reaction occurs within the shock front itself, enabling the wave to by-pass the von Neumann state and proceed directly to the weak branch of the product Hugoniot. The mechanism suggested in this paper, namely, a high degree of flow non-equilibrium resulting from shock interactions, is believed to be a new mechanism able to realize weak (non-CJ) solutions.

The deviations from CJ speed depend significantly upon the ratio of specific heats, γ, as seen in Fig. 2.6(b). The heuristic model developed in the Appendix, which examines the limiting case of the time delay going to zero ($\tau \to 0$) and the spatial discreteness also approaching zero ($\Gamma \to 0$), such that the energy release of the first source will result in a classical point blast solution, may provide an explanation for this trend. In this model, subsequent sources will release their energy on the shock front of the prior source, and as discussed in the Appendix, the partitioning of energy release of that source into forward and backward directed blast waves is related to the density ratio in the limit of a strong shock front ($\frac{\gamma+1}{\gamma-1}$). Since this function increases rapidly as the value of γ approaches unity ($\gamma \to 1$), we would expect the energy release of subsequent sources to be increasingly directed in the direction of propagation. In simpler language, in the limit of γ going to unity, the strong shock front becomes a solid wall, so that energy released on that wall results in a blast wave directed entirely forward. This picture may provide a qualitative explanation for the influence of γ, and indeed the simple heuristic model developed in the

Appendix performs better in predicting the average wave speed than might be expected, as seen in Fig. 2.6(b).

As the value of dimensionless heat release Q varies in a way such that the CJ detonation velocity for an equivalent homogeneous reactive medium remains in the range between $M_{\mathrm{CJ}} = 4$ and $M_{\mathrm{CJ}} = 10$, the ratio of the resulting V_{avg} in the discrete reactive system to the homogenous equivalent V_{CJ} exhibits no significant change (see Fig. 2.6(c)). An insight obtained from the heuristic model is that the key dynamics of the wave propagation in a medium of discrete sources can be fairly well pictured as a complex superposition of blast waves generated by a series of point sources. According to the Taylor-Sedov blast wave solution, the average speed at which the blast wave front propagates over a fixed distance has a square root dependence on the energy released by a planar source, namely, $\sqrt{Q}$. In the limit of large heat release, the CJ velocity also linearly depends on $\sqrt{Q}$. Hence, this dependence of $\sqrt{Q}$ might be expected to cancel out when V_{avg} is normalized by V_{CJ}, and this may explain the results presented here.

The result that the deviations of the average wave speed away from the CJ speed do not depend on delay time is another result from this study, as seen in Fig. 2.6(d). The delay time was varied between $\tau = 0.004$, meaning that the sources release their energy effectively instantaneously upon contact with the leading shock, and $\tau = 3$, meaning that the blast wave released by a source must approximately propagate a distance of three source spacings before it reaches the location where the shock was when the source released its energy, by which time the leading shock had moved further downstream as well, resulting in it taking even longer for the blast to reach the leading shock. In this limit of large τ, given the large number of blast wave interactions that occur before the blast from a source actually reaches the leading shock and contributes to its sustenance, it is perhaps remarkable that the average speed does not depend upon the delay time. Note, however, that in the classical CJ detonation model, the details of the reaction zone,

such as kinetic rates, do not affect the detonation wave velocity. In this connection, it is perhaps plausible that the results do not depend on the delay time of the discrete sources.

The results of this study may have application to resolving the conundrum that was discussed previously in Ch. 2, namely, resolving why the CJ criterion is so successful in describing the average propagation velocity of transient and multidimensional detonation waves. Unstable detonations feature pockets of gas that may get compressed by multiple shock waves and explode, while other portions of the detonation cell might be described by a non-reacting shock wave. The study of Kiyanda and Higgins [47] estimated that nearly the entire second half of a detonation cell in low pressure methane/oxygen does not react coupled to the shock front, but rather burns as shock-compressed pockets detached from the leading front. The effective discreteness of such unstable detonations, as defined in this paper, is unlikely to be less than $\Gamma = 0.3$. As shown in Fig. 2.7, it is unlikely that deviations from the ideal CJ speed would be more than a few percent for this degree of discreteness, a difference that is hardly experimentally resolvable. This result may also have relevance to the phenomenon of galloping detonation, wherein steady detonation propagation is not possible due to the tube diameter being smaller than a characteristic cell size required for propagation, such that the detonation fails to approximately half CJ speed and periodically reinitiates to an initially overdriven wave via a process similar to deflagration to detonation transition (DDT). Despite the fact that the cycle of the galloping detonation occurs over hundreds of tube diameters and the wave should experience significant heat and momentum losses due to the relatively small size of the tube used, galloping detonations continue to propagate remarkably close to the CJ speed on average [48, 49, 50]. This aspect of the discrete source detonation model has been further explored by Radulescu and Shepherd [51]. The possibility that all real detonations might be weak detonations (if only slightly away from the CJ solution) is intriguing, as this idea was suggested by Davis [52] but has not attracted significant attention in detonation research.

The results of the present study are fundamentally different from those of Mi and Higgins [53], which examined the discrete source detonation problem in a Burgers analog system. The one-dimensional, inviscid scalar Burgers equation with a source term was proposed by Fickett and Davis [54] and Majda [55] as an analog to the reactive Euler equations in order to explore detonation dynamics. In recent years, study of this scalar analog system has generated a number of interesting results, including the existence of pulsating, chaotic solutions [56, 57, 58, 59]. The study of Mi and Higgins [53] was a precursor to the present study using the inviscid Burgers equation with periodically spaced δ-function sources that were triggered by the passage of the leading shock front. Both regularly spaced sources with fixed delay and randomly spaced sources with randomly generated delays were considered. The resulting wave dynamics involved the interaction of a number of sawtooth-profiled blast waves generated by the sources. For the Burgers equation the trajectories of the blast waves could be solved analytically. In all cases considered, the average propagation velocity was found to be within 1% of the CJ detonation velocity of the equivalent CJ system. That result is in seeming contradiction to the results of the present study, which exhibited super-CJ solutions, so comparing these two studies warrants further discussion. The Euler equations have three families of propagating characteristics, namely, right-running, left-running, and particle characteristics, while the Burgers equation has only the family of right-running characteristics. This feature of the Burgers equation system might explain the unusual dynamics noted in [53] (see Sec. 2.1.3.2 and Fig. 2.7(b)) wherein the limiting characteristic became coincident with the locus of new sources in the case of regularly spaced sources with a fixed delay, while in the present study, the limiting characteristic is spatially separated from the locus of new sources (see Figs. 2.4 and 2.9 in the present paper). This aspect of the Euler equations means that the dynamics of the shock front influences the post-shock flow, which in turn influences the shock again, resulting in the entire flow being a nonsimple wave re-

gion. In the present study, the super-CJ velocity in a discrete reactive medium is a direct result of the significantly intense mechanical fluctuation near the limiting characteristic (as explained in Sec. 2.1.3.3 and shown in Fig. 2.9), which is caused by the downstream propagating blast waves generated by the sources releasing energy. In contrast, due to the lack of left-running characteristics, a source releasing energy cannot generate a blast wave influencing the flow field downstream from the source in the Burgers equation system [53]. Thus, we can hypothesize that it is the existence of both right- and left-running characteristics that is the necessary feature to observe the super-CJ solutions found in this study.

Extension of the current, Euler equation-based study to higher dimensions is likely to reveal richer behavior. Examination of the propagation of flames in three dimensional systems of random, discrete sources has revealed a percolation-like regime that has demonstrated the ability of flames to propagate beyond the thermodynamic limit of the corresponding homogeneous medium [31], and similar behavior may occur with detonations in discrete systems. Examination of detonation propagation in the limit of spatially randomized, point-like sources in three dimensional clouds may have some relevance to the anomalous scaling between experiments in axisymmetric geometries (tubes) and two-dimensional slab geometries (rectangular geometries) [60, 61, 62, 63, 64]. A preliminary step in this direction was made in the recent computational study of Li *et al.* [35], in which a two-dimensional sinusoidal ripple in properties was introduced in a medium prior to detonation propagation through it. Extension of this study using perturbations with greater discreteness than sinusoidal would be of great interest.

Detonation theory has profitably explored the asymptotic limits of high activation energy [65, 66], zero activation energy [67], high overdrive [68, 69], low energy release [70], and the Newtonian limit (i.e., ratio of specific heats approaching unity) [71]. The line of investigation suggested in this study examines a different type of asymptotic limit, the

limit of spatially discrete energy sources approaching δ-functions in space and time. It is unknown if a rational asymptotic solution to the problem, rigorously derived from the governing Euler equations can be found, in contrast to the *ad hoc* solution constructed in the Appendix. This problem is left as an open question to the detonation theory community.

2.1.5 Conclusions

Detonation propagation in systems with the energy release of the medium spatially concentrated into discrete pockets was simulated computationally. The energy release of one such discrete source drives a blast wave, which is capable of initiating the next source after a prescribed delay. The resulting ensemble of blast wave interactions propagates in a quasi-periodic manner, and the average wave speed was measured. Systematic variation of the model parameters identified that the average wave deviated significantly from the CJ detonation speed of the equivalent homogenous media, with speeds as great as 15% in excess of the CJ speed being measured. This discrepancy is significant, given that experimental measurements of detonation speeds in gases usually agree to within 1% of the equilibrium CJ speed. A systematic variation of model parameters found that the deviation away from CJ depended on the degree of spatial concentration of the sources (more discrete sources resulted in greater deviations above CJ), with the wave speed reaching an asymptotic limit as the sources were concentrated into a space occupying less than 1% of the entire domain (limit of $\Gamma \to 0$). The deviation from CJ also depended on the ratio of specific heats (with greater deviations observed as $\gamma \to 1$), but the deviation from CJ did not depend upon the delay time of the sources between being shocked and releasing their energy or the average value of the energy release. The results were interpreted via temporal averaging of the simulations onto a steady, one-dimensional projection that

could be compared with the classical ZND structure of detonations. This analysis suggests that the existence of non-CJ solutions can be interpreted as weak detonations due to the non-equilibrium of the flow resulting from the ensemble of shock interactions as the flow crosses the effective sonic surface.

2.2 One- and two-dimensional detonation systems with Arrhenius kinetics

In the previous section, an artificial mechanism of energy deposition, i.e., a discrete source that is instantaneously triggered by the passage of the leading shock, independent of the shock strength, after a prescribed delay time, was implemented due to its simplicity. Hence, a more realistic mechanism of heat release, wherein the energy release evolves from the reactive media itself, depending upon the local thermodynamic state, must be incorporated in order to further investigate the effect of spatial inhomogeneities on gaseous detonations.

In this section, the effect of both one- and two-dimensional spatial inhomogeneities on the propagation speed of gaseous detonation waves without losses is computationally examined. Since a typical detonable mixture of gases is governed by activated chemical reactions, single-step Arrhenius kinetics, as the simplest candidate reaction model, is incorporated into the system. The spatial discretization of energy can be realized, as illustrated in Fig. 2.10(b), via concentrating the reactant into layers (or sheets), standing perpendicular to the direction of detonation wave propagation, separated by regions of inert gas. Another way to discretize the reactive medium is by concentrating the reactant into infinitely long square-based prisms laying along an axis that is perpendicular to the direction of detonation wave propagation, as shown in Fig. 2.10(c). This arrangement can be implemented in two-dimensional simulations as an array of square sources. These two arrangements of spatial inhomogeneities are referred to as reactive *layers* and *squares*, respectively, in this paper.

The first objective of this study is to examine whether the super-CJ wave propagation still occurs in a one- or two-dimensional gaseous detonation system with state-dependent Arrhenius kinetics. The simulation results are then analyzed via a spatio-temporal averaging procedure to further elucidate the physical mechanism that is responsible for this super-CJ wave speed. By performing parametric studies, a continuous transition from the continuum CJ propagation to the super-CJ waves in extremely discretized reactive media, i.e., a sequence of point-source blasts that in turn trigger the next source, is systematically explored and analyzed.

This section is organized as follows. In Sec. 2.2.1, the problem statement and the governing equations of the proposed system are introduced. Section 2.2.2 describes the numerical methodology used to solve the governing equations. The results of sample one- and two-dimensional wave structures, the history of instantaneous propagation speed, and the averaged propagation speed as a function of the model parameters are presented in Sec. 2.2.3. In Sec. 2.2.4, the procedures of data analysis are described. The findings based upon the simulation results and the analysis are discussed in Sec. 2.2.5 and summarized in the Conclusions (Sec. 2.2.6). The detailed derivation of the governing equations based on the averaged properties can be found in the Appendix B.

2.2.1 Problem statement

The detonable mixtures are modeled to be calorically perfect (i.e., with a fixed ratio of specific heats γ) and have the potential to release chemical energy with a specific heating value $\widetilde{Q}$ (J/kg). The tilde "$\sim$" denotes a dimensional quantity. The flow variables, density, pressure, temperature, and particle velocity (x- and y-components), are non-

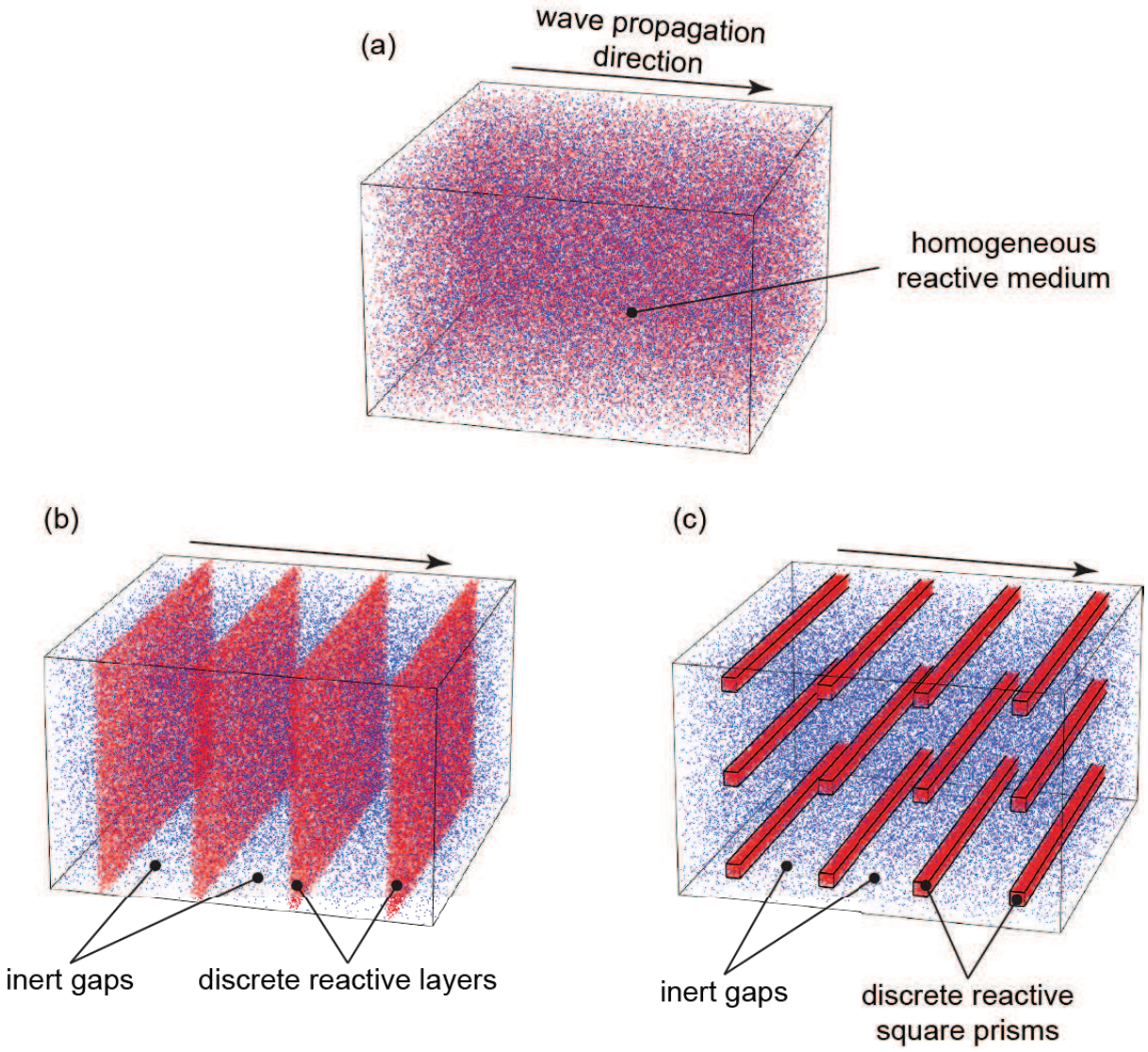

Figure 2.10: Conceptual illustrations of a reactive system with (a) energy sources (red dots) homogeneously embedded within an inert medium (blue dots), (b) energy sources collected into spatially discretized layers (or sheets), and (c) energy sources collected into square-based prisms separated by inert regions.

dimensionalized with reference to the initial state ahead of the leading shock as shown in Sec. 2.1.1. The properties of a thermodynamic state are related via the ideal gas law, i.e., $\widetilde{p} = \widetilde{\rho}\widetilde{\mathrm{R}}\widetilde{T}$, where $\widetilde{\mathrm{R}}$ is the gas constant, or $p = \rho T$ in dimensionless form. The heat release $\widetilde{Q}$ is non-dimensionalized as $Q = \widetilde{Q}/\left(\widetilde{p}_0/\widetilde{\rho}_0\right)$. Applying the CJ criterion, the velocity of a detonation wave propagating in a uniform reactive medium with the heat release Q can be calculated via Eq. 2.1. The average propagation speed resulting from each inhomogeneous scenario simulated in this study will be compared with the V_{CJ} corresponding to a homogeneous reactive system with the same average energy release Q.

The non-linear, unsteady gasdynamics of the system is described by the two-dimensional (or one-dimensional) reactive Euler equations in the laboratory-fixed reference frame:

$$\frac{\partial \mathbf{U}}{\partial t} + \frac{\partial \mathbf{F}\left(\mathbf{U}\right)}{\partial x} + \frac{\partial \mathbf{G}\left(\mathbf{U}\right)}{\partial y} = \mathbf{S}\left(\mathbf{U}\right) \tag{2.20}$$

where the conserved variable $\mathbf{U}$, the convective fluxes $\mathbf{F}$ and $\mathbf{G}$, and reactive source term $\mathbf{S}$ are, respectively,

$$\mathbf{U} = \begin{pmatrix} \rho \\ \rho u \\ \rho v \\ \rho e \\ \rho Z \end{pmatrix} \qquad \mathbf{F} = \begin{pmatrix} \rho u \\ \rho u^2 + p \\ \rho uv \\ (\rho e + p)u \\ \rho Z u \end{pmatrix} \qquad \mathbf{G} = \begin{pmatrix} \rho v \\ \rho uv \\ \rho v^2 + p \\ (\rho e + p)v \\ \rho Z v \end{pmatrix} \qquad \mathbf{S} = \begin{pmatrix} 0 \\ 0 \\ 0 \\ 0 \\ \rho\Omega \end{pmatrix} \tag{2.21}$$

In the above equations, e is the non-dimensional specific total energy, and Z is the reaction progress variable, or the normalized concentration of reactant, which varies between 1 (unreacted) and 0 (fully reacted). For a homogeneous reactive system, the specific total energy is defined as $e = p/(\gamma - 1)\rho + (u^2 + v^2)/2 + ZQ$. In this study, the reaction rate

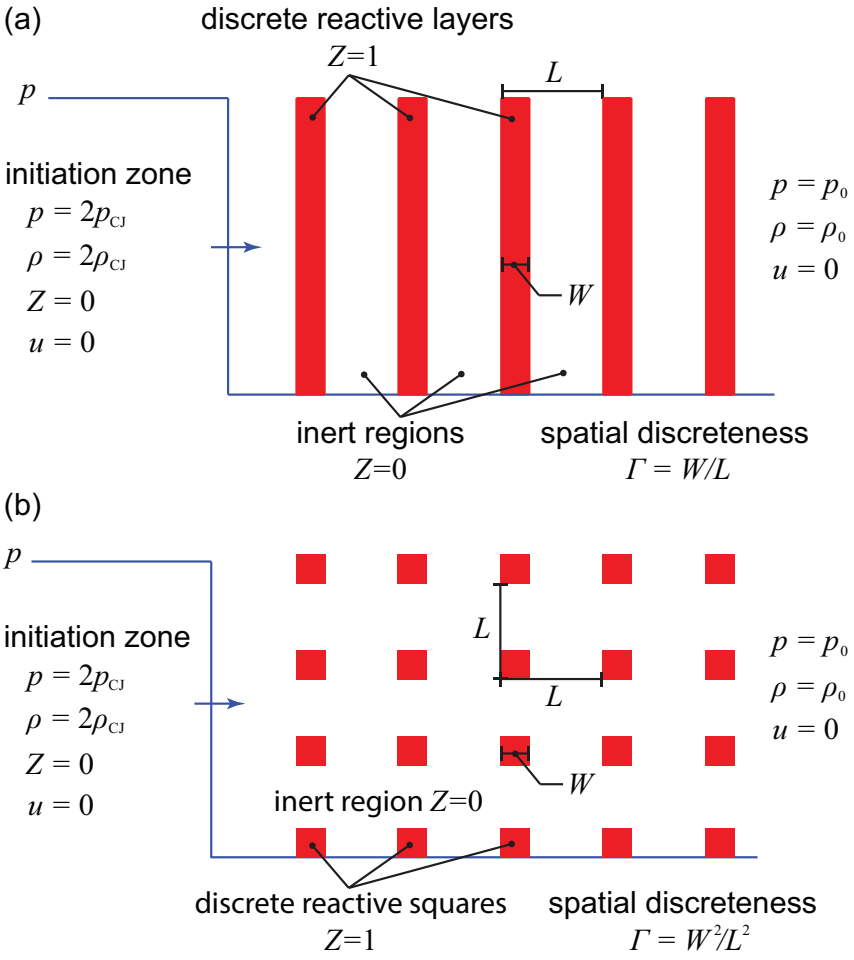

Figure 2.11: Schematic showing the initiation method and implementation of spatially discrete reactive (a) layer and (b) squares.

$\Omega = \partial Z/\partial t$ is governed by single-step Arrhenius chemical kinetics as follows,

$$\Omega = -kZ \times \exp\left(-E_{\mathrm{a}}/T\right) \tag{2.22}$$

where k and E_{a} are the dimensionless pre-exponential factor and activation energy, respectively.

The reactive domain that contains discrete sources is initialized with uniform pressure,

density, and particle velocity as $p = 1$, $\rho = 1$, and $u = 0$, respectively. An initiation zone, where pressure and density equal twice the corresponding CJ value, i.e., $p = 2p_{\mathrm{CJ}}$ and $\rho = 2\rho_{\mathrm{CJ}}$, is placed on the left of the reactive domain. A rightward propagating shock wave generated from this initiation zone thus triggers the discrete sources and supports a reaction wave to propagate to the right. The spatial inhomogeneities are introduced into the system as spatially discrete reactive layers or squares separated by inert regions. This spatial discretization is realized by initializing Z as 1 in the reactive sources and 0 in the inert regions. As shown in Fig. 2(a), the reactive layers with a width W are distributed in the domain with a regular spacing L between each two consecutive layers. Thus, the initial distribution of Z in space can be described as a summation of regularly spaced, one-dimensional Heaviside (boxcar) functions,

$$Z\left(x, y, t = 0\right) = \sum\nolimits_i \mathrm{H}\left(x - iL\right) \mathrm{H}\left(iL + W - x\right) \tag{2.23}$$

where i is the index of each discrete reactive layer. The scenario with discrete reactive squares is shown in Fig. 2 (b). The side length of each square source is W and the spacing between each two neighboring sources is L. In this case, the initial distribution of Z can be described as a summation of regularly spaced, two-dimensional Heaviside functions,

$$Z\left(x, y, t = 0\right) = \sum\nolimits_i \sum\nolimits_j \mathrm{H}\left(x - iL\right) \mathrm{H}\left(iL + W - x\right) \mathrm{H}\left(y - jL\right) \mathrm{H}\left(jL + W - y\right) \tag{2.24}$$

where i and j are the indices of each discrete reactive square in x- and y-directions, respectively.

The spatial discreteness parameter Γ is defined as $\Gamma = W/L$ for the cases with reactive layers and $\Gamma = W^2/L^2$ for the cases with reactive squares. In the limit of $\Gamma \to 1$, the

initial distribution of Z becomes uniform in the reactive medium; in the limit of $\Gamma \to 0$, the spatially discrete source approaches a δ-function in space. In order to maintain the overall amount of energy release Q the same as the homogeneous case ($\Gamma = 1$), the actual heat release associated with each discrete source must be increased according to the prescribed spatial discreteness Γ. Hence, for the cases with discrete reactive sources, the specific total energy is formulated as $e = p/(\gamma - 1)\rho + (u^2 + v^2)/2 + ZQ/\Gamma$.

This current study is focused on exploring the effect of spatial discreteness Γ and source spacing L on the wave propagation behavior in an inhomogeneous reactive medium. The values of Q and γ are chosen to be $Q = 50$ and $\gamma = 1.2$ to represent a typical gaseous detonable mixture. The dimensionless activation energy is chosen to be $E_a = 20$ to ensure stable detonation propagation in the one-dimensional, homogeneous system, which can be used as a control case to more clearly identify the effect of the spatial inhomogeneities and intrinsic multi-dimensional instabilities on the resulting propagation behavior. [72, 73] The pre-exponential factor $k = 16.45$ is chosen so that the half-reaction-zone length for the homogeneous case is unity.

2.2.2 Numerical methodology

Two independently-written simulation codes were used to solve the one- and two-dimensional reactive Euler equations. Both of them were based upon a uniform Cartesian grid. The one-dimensional simulation code used the MUSCL-Hancock TVD Godunov-type finite-volume scheme [38] with an exact Riemann solver and the van Leer non-smooth slope limiter. The reaction process in the one-dimensional simulations was solved using a second-order, two-stage explicit Runge-Kutta method. The Strang splitting method was used in order to maintain second-order accuracy. [74] The two-dimensional simulation

code was also based upon the MUSCL-Hancock scheme but with an HLLC approximate solver for the Riemann problem. [75, 76] This code was implemented in Nvidia's CUDA programming language and performed on a Nvidia Tesla K40M GPU computing processor to accelerate the simulation runs.

In each case simulated in this study, the length (i.e., size in the x-direction) of the entire domain was at least 50 times the source spacing L. For the cases with reactive squares, the transverse width (i.e., size in the y-direction) was at least $5L$. In order to have a better algorithmic efficiency, instead of the entire domain, the simulations were only performed in a window that enclosed the leading wave complex at each time step. A window size (in the x-direction) of $10L$ (i.e., containing 10 discrete reactive layers or 10 vertical arrays of reactive squares) was used and was verified to be sufficient to capture all of the dynamics contributing to the propagation of the leading shock. Once the leading shock front reached the end (right boundary) of the computational window, the window frame (i.e., left and right boundaries) was advanced by half of the window size $5L$. A transmissive boundary condition was applied on both left and right boundaries of the computational window. On the top and bottom boundaries, a periodic boundary condition was applied to simulate a detonation wave propagating in an infinitely wide domain without experiencing any losses due to lateral expansion. The minimum numerical resolution used in this study was 20 computational cells per half-reaction-zone (unity) length of the homogeneous case, i.e., $\Delta x = 0.05$. For cases with very small source spacing, e.g., $L = 1$, a high numerical resolution of 100 computational cells per half-reaction-zone length was used to ensure a sufficient number (~ 10) of computational cells within a discrete source.

2.2.3 Result

Results from three different cases are presented here: reactive layers in one dimension, reactive layers in two dimensions, and reactive squares in two dimensions. For each case, a snapshot of the flow field will be shown, followed by the velocity history. The measured average velocity, V_{avg}, will be presented as a function of spatial discreteness Γ and source spacing L. Since $Q = 50$, $\gamma = 1.2$, and $E_{\text{a}} = 20$ are fixed in this current study, only the values of L and Γ are mentioned for each specific case of simulation presented in the remainder of this paper. In Figs. 2.15 and 2.18 where the results of V_{avg} are presented, the data points for the cases with one-dimensional reactive layers, two-dimensional reactive layers, and two-dimensional reactive squares are plotted as blue circles, green diamonds, and red squares, respectively; solid symbols are for the cases with a fixed L and various Γ, while open symbols are for the cases with a fixed Γ and various L.

2.2.3.1 One-dimensional reactive layers

The sample result plotted in Fig. 2.12 shows the time evolution (from (a) to (c)) of the pressure (top row) and reaction progress variable (bottom row) profiles of the computational domain for a simulation with $\Gamma = 0.04$ and $L = 10$ (spacing between two sources). The leading wave front propagates rightward in this figure. The δ-function-like, vertical spikes in the profile of Z, as indicated in the figure, are the discrete reactive layers where chemical energy is highly concentrated. As shown in Fig. 2.12(a), the peak in the pressure profile is associated with a strong exothermic reaction upon the leading shock encountering one of these reactive layers. The shorter spike in the Z profile in Fig. 2.12(a) corresponds to this partially reacted discrete source shortly after being shocked. As shown in Fig. 2.12(b), forward- and backward-running blast waves that are generated by this strong exothermic reaction can be identified in the pressure profile. Downstream from the

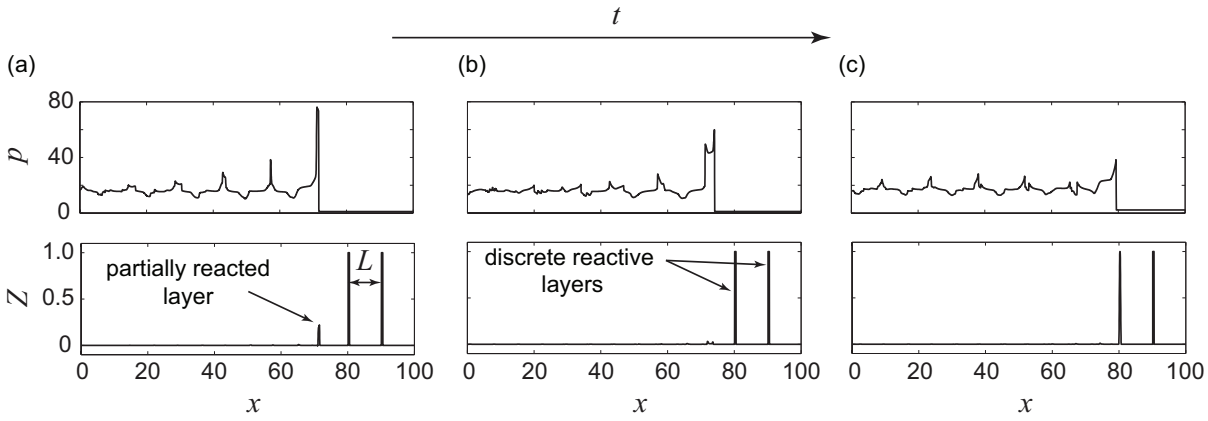

Figure 2.12: Time evolution (from (a) to (c)) of the pressure (top row) and reaction progress variable (bottom row) profiles for a one-dimensional simulation with reactive layers and the following parameters: $\Gamma = 0.04$ and $L = 10$.

leading shock, the pressure profile consists of a large number of decaying and interacting blast waves generated by the earlier sources. The history of the instantaneous propagation speed V normalized by V_{CJ} for the same case is plotted in Fig. 2.14(a) as a function of the leading shock position x_{s}. The trajectory of the leading shock $x_{\mathrm{s}}(t)$ can be obtained from the simulation by finding the location where pressure increases to $p = 1.5$ from its initial, pre-shock state $p_0 = 1$ at each time step. The instantaneous propagation speed V can then be calculated by numerically differentiating $x_{\mathrm{s}}(t)$ over time. After a short process of initiation (over approximately 5 sources), the wave propagation becomes periodic as shown in the inset in Fig. 2.14(a). A cycle of pulsation in wave velocity, V, occurs over a length that is the same as the spacing between two reactive layers, L. An averaged propagation speed can be measured over a long distance (about 40 sources). The average wave speeds V_{avg}, normalized by V_{CJ}, resulting from the one-dimensional simulations are plotted as functions of Γ and L (as solid and open blue circles) in Fig. 2.15(a) and (b), respectively. As Γ decreases from 1 to 0.01 or L increases from 1 to 200, V_{avg} increases from V_{CJ} and asymptotically approaches a plateau value that is approximately 9-10% greater than V_{CJ}.

2.2.3.2 Two-dimensional reactive layers

The sample results plotted in Fig. 2.13(a) and (b) are the two-dimensional contours of the pressure (left column) and reaction progress variable (right column) at early ((a) $t = 30.2$) and later (b) $t = 140.5$) times for a simulation of discrete reactive layers with $\Gamma = 0.04$ and $L = 10$. The leading wave front propagates rightward in this figure. The red, vertical lines in the contours of Z are the highly concentrated, reactive layers. At early times, as shown in Fig. 2.13(a), the resulting wave structure remains transversely planar (uniform in the y-direction). Forward- and backward-running blast waves associated with high pressure (yellow-red) regions can be clearly identified in Fig. 2.13(a). At later times, as shown in Fig. 2.13(b), significant instabilities have developed, resulting in a no longer planar but highly irregular wave structure. The history of V/V_{CJ} as a function of leading shock position x_{s} is plotted in Fig. 2.14(b). At each time step, the leading shock position is found along the middle line in y-direction of the two-dimensional domain (at $y = 25$) using the same technique described in Sec. 2.2.3.1.

As shown in Inset I of Fig. 2.14(b), V varies in a regularly periodic fashion over a length scale of L. After the wave propagates over more than 700 sources, the variations in V become irregular and exhibit much larger amplitudes. As shown in Inset II, the spacing between two consecutive peaks in V is no longer a constant distance L. Note that, before the onset of instabilities, the propagation dynamics resulting from this two-dimensional case with reactive layers are identical to those of the one-dimensional case with the same parameter values (shown in Fig. 2.14(a)). The average propagation velocities reported in this paper were measured over a sufficiently long distance (more than 40 sources) after the instabilities had fully developed. The V_{avg} values resulting from the two-dimensional simulations with reactive layers are plotted as functions of Γ and L (as solid and open green diamonds) in Fig. 2.15(a) and (b), respectively. As Γ decreases or L increases, V_{avg}

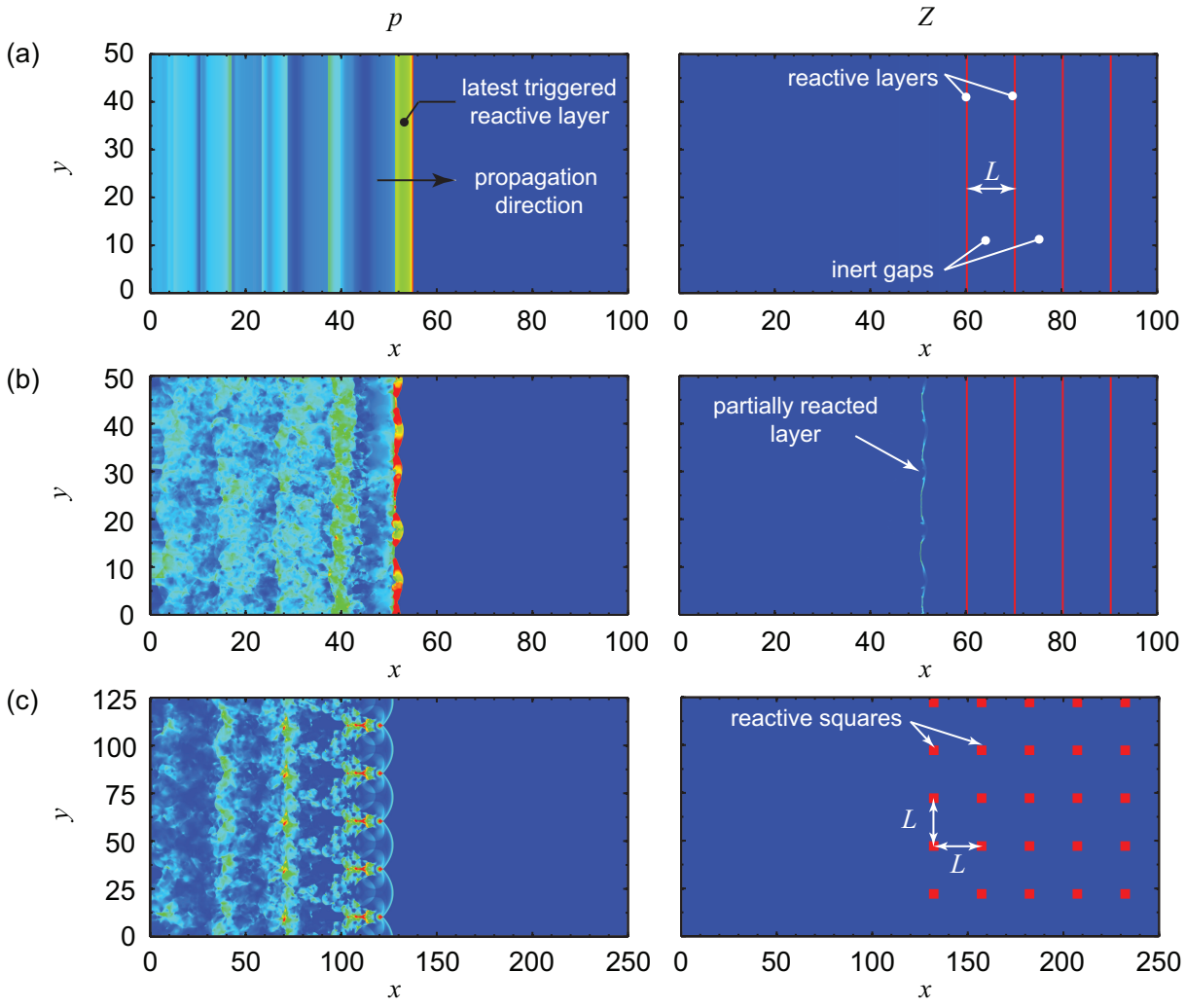

Figure 2.13: Sample two-dimensional contours of the pressure (left column) and reaction progress variable (right column) for the case with reactive layers at (a) early ($t = 30.2$) and (b) later ($t = 140.5$) times with $\Gamma = 0.04$ and $L = 10$, and (c) for the case with reactive squares, $\Gamma = 0.04$, and $L = 25$.

increases from V_{CJ} to super-CJ values. In Fig. 2.15(b), as L increases from 5 to 200, V_{avg} asymptotically approaches a plateau value that is nearly 10% greater than V_{CJ}, which is approximately the same as that resulting from the one-dimensional cases. The V_{avg} of the two-dimensional simulations are less than those of the corresponding values of the one-dimensional simulations for the same value of Γ and L.

2.2.3.3 Two-dimensional reactive squares

The sample results plotted in Fig. 2.13(c) are the two-dimensional contours of the pressure (left figure) and reaction progress variable (right figure) at early and later times for a simulation of discrete reactive squares with $\Gamma = 0.04$ and $L = 25$. The leading wave front propagates rightward in this figure. The red squares in the contour of Z are the highly concentrated sources of energy. As shown in the contour of pressure in Fig. 2.13(c), the transversely regular, wavy leading wave front, which consists of blast waves generated by the energy release of regularly spaced square sources, can be identified. Downstream (to the left) from the leading shock, the wave structure becomes increasingly irregular. In the plot of V/V_{CJ} as a function of leading shock position (Fig. 2.13(c)), a regularly periodic variation in V over a length of L, as shown in the inset of Fig. 2.14(c), persists throughout the simulation containing 120 vertical arrays of square sources. The leading shock position is again defined as that along the middle line in y-direction of the two-dimensional domain (at $y = 62.5$). The values of V_{avg} resulting from the two-dimensional simulations with reactive squares are plotted as functions of Γ and L (as solid and open red squares) in Fig. 2.15(a) and (b), respectively. As Γ decreases or L increases, V_{avg} increases from V_{CJ} to super-CJ values. In Fig. 2.15(b), at $L = 50$, V_{avg} reaches the same plateau value (i.e., nearly 10% greater than V_{CJ}) as that resulting from both the one- and two-dimensional cases with reactive layers. The V_{avg} of the two-dimensional, reactive square cases is fairly close to that of the two-dimensional, reactive layer cases, but lower

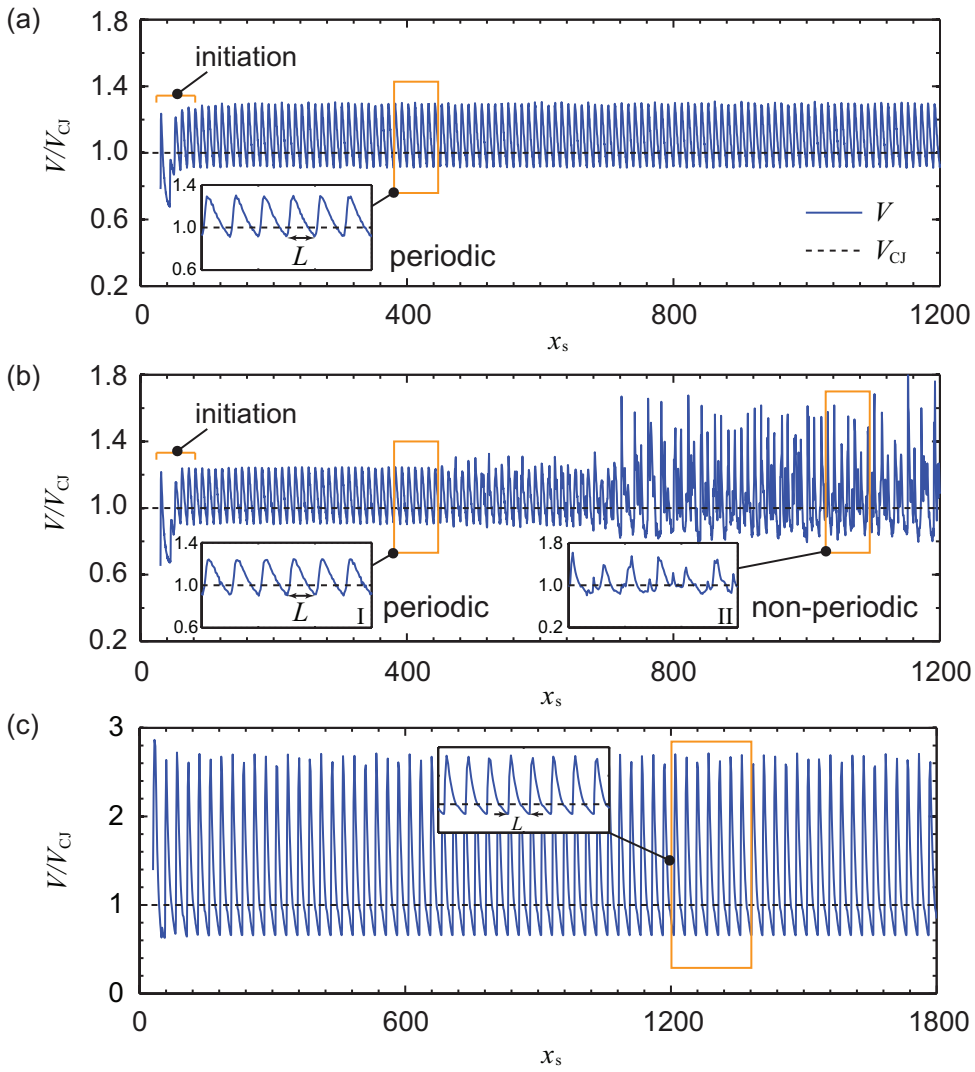

Figure 2.14: The history of instantaneous wave propagation velocity normalized by CJ velocity (V/V_{CJ}) as a function of the leading shock position for the cases with (a) one- and (b) two-dimensional reactive layers ($\Gamma = 0.04$ and $L = 10$), and (c) reactive squares ($\Gamma = 0.04$ and $L = 25$).

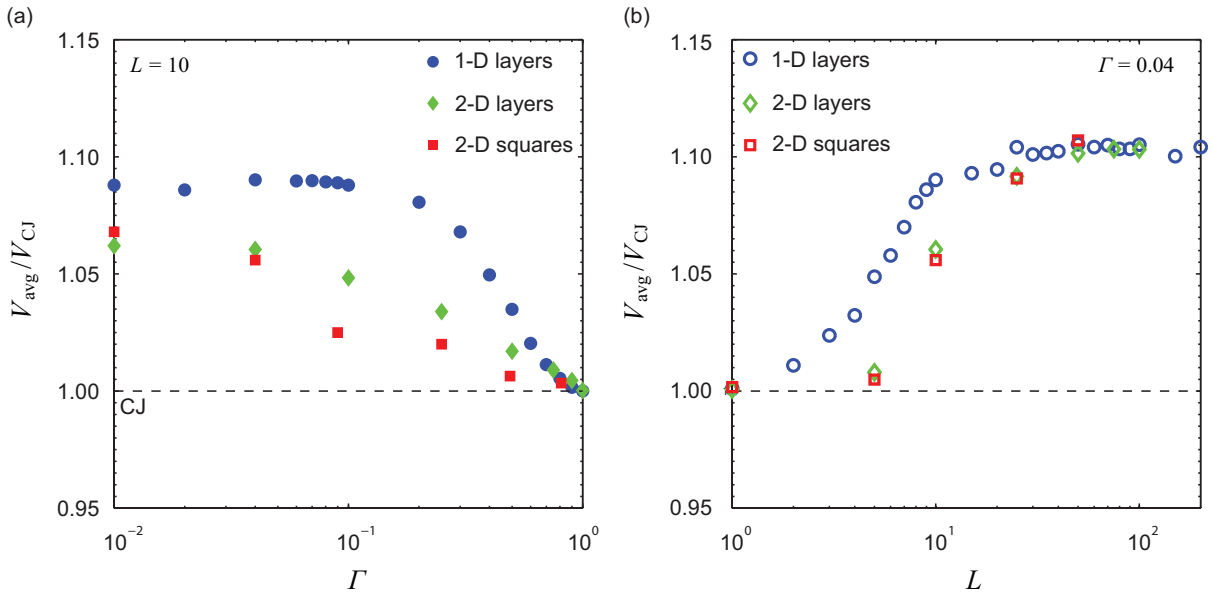

Figure 2.15: For cases with one-dimensional reactive layers (blue circles), two-dimensional reactive layers (green diamonds), and two-dimensional reactive squares (red squares), average wave propagation velocity normalized by CJ velocity as (a) a function of Γ with $L = 10$ and (solid symbols) (b) a function of L with $\Gamma = 0.04$ (open symbols).

than that of the one-dimensional cases for the same values of Γ and L.

2.2.4 Analysis

As shown in Sec. 2.2.3, a full spectrum of average wave propagation speeds that are significantly greater than V_{CJ} is obtained in both one- and two-dimensional systems with discretized energy sources governed by finite-rate, state-dependent Arrhenius kinetics. In order to understand the physical mechanism underlying these super-CJ waves, the simulation results are analyzed in two steps. First, the results of select cases are analyzed via a density-weighted (Favre), spatio-temporal averaging method. Using this analysis, which was introduced to the field of detonation by Lee and Radulescu [9], Radulescu *et al.* [4], and Sow *et al.* [44]. The super-CJ propagation, resulting from a system with highly concentrated sources that instantaneously deposit energy after a fixed delay time

is interpreted in Sec. 2.1 as weak detonations owing to the non-equilibrium condition at the average sonic surface. The motivation of performing this analysis in the present study is to verify that this mechanism of weak detonation is also responsible for the super-CJ propagation with more realistic reaction kinetics and a higher dimension. Second, with the assistance of an x-t diagram constructed from the numerical flow field, a physical parameter, τ_c, which compares the reaction time of a source t_r and shock transit time from one source to the next t_s, i.e., $\tau_c = t_r/t_s$, can be determined. This parameter is used to explain the continuous transition of the propagation speed from V_{CJ} to the plateau super-CJ value.

2.2.4.1 Averaged steady, one-dimensional wave structure

One- and two-dimensional systems with discrete reactive layers are analyzed using a Favre-averaging approach. The two representative cases selected for further analysis are with $\Gamma = 0.04$ and $L = 10$. The resulting average wave speed V_{avg} in both these one- and two-dimensional cases is approximately 10% greater than the CJ speed. Since the simulations are performed in a lab-fixed reference frame, the data are first transformed into a wave-attached reference frame moving at a constant value of V_{avg}. For the one-dimensional case, temporal averaging is performed to the transient wave structure as the leading shock propagates over 20 sources. For the two-dimensional case, the resulting flow field at each time step is first spatially averaged over the transverse (y-) direction. The temporal averaging is then performed to the time history of the spatially averaged one-dimensional wave profiles. The two-dimensional results are averaged over the time span required for the leading shock to propagate over 20 sources. The detailed derivation of the Favre-averaged equations can be found in the Appendix.

In Fig. 2.16(a), the averaged pressure $\bar{p}$ for the one-dimensional case is plotted with

respect to the wave-attached coordinates x', where $x' = x - V_{\text{avg}}t$. The sonic point marked as the black circle on the profile of $\bar{p}$ is where the slope of the averaged $u + c$ characteristics equals 0, i.e., $u^* + c^* = 0$. The average pressure at this averaged sonic point, $\bar{p}_{\text{sonic}} = 25.1$, is significantly greater than the pressure of the equilibrium CJ state, as indicated by the horizontal dashed line, $p_{\text{CJ}} = 21.5$. This deviation of $\bar{p}_{\text{sonic}}$ from p_{CJ} suggests that equilibrium is not reached as the flow passes through the effective sonic surface. In order to further verify this finding, the thermicity due to the mechanical fluctuation in momentum ϕ_{M} (blue dash-dot curve), the thermicity due to the thermal fluctuation in total energy ϕ_{T} (green dash curve), and the exothermicity associated with chemical reaction ϕ_{R} (red dotted curve) are evaluated and plotted near the average sonic point in Fig. 2.16(b). Thermicity is defined as the terms in the momentum equation that result in a change in the average flow velocity or, equivalently, a change in average pressure of the flow in the reaction zone of a detonation. As shown in this inset, ϕ_{M}, ϕ_{T}, and ϕ_{R} are still finite, the total thermicity, i.e., $\phi = \phi_{\text{M}} + \phi_{\text{T}} + \phi_{\text{R}}$ (thick black line), reaches zero in the vicinity of the sonic point. These significant fluctuations in momentum and total energy render a non-equilibrium state of the flow upon reaching the effective sonic surface. The derivation of ϕ_{M}, ϕ_{T}, and ϕ_{R}, and the master equation (Eq. D.3) that relates the acceleration/deceleration of the averaged flow with the total thermicity and sonic condition are shown in the Appendix.

A similar profile of $\bar{p}$ is obtained for the two-dimensional case as shown in Fig. 2.16(c). The jump in pressure associated to the averaged leading shock front is however less sharp (smeared out) than that for the one-dimensional case. As indicated by the black circle in the inset, $\bar{p}_{\text{sonic}} = 21.8$ is close to but still greater than p_{CJ} (dashed line). As shown in Fig. 2.16(d), while the exothermic reaction rate still remains significantly positive, and ϕ_{M} and ϕ_{T} persist with significantly large amplitudes, the total thermicity ϕ vanishes in the immediate vicinity of the average sonic point. Thus, in the two-dimensional case, the

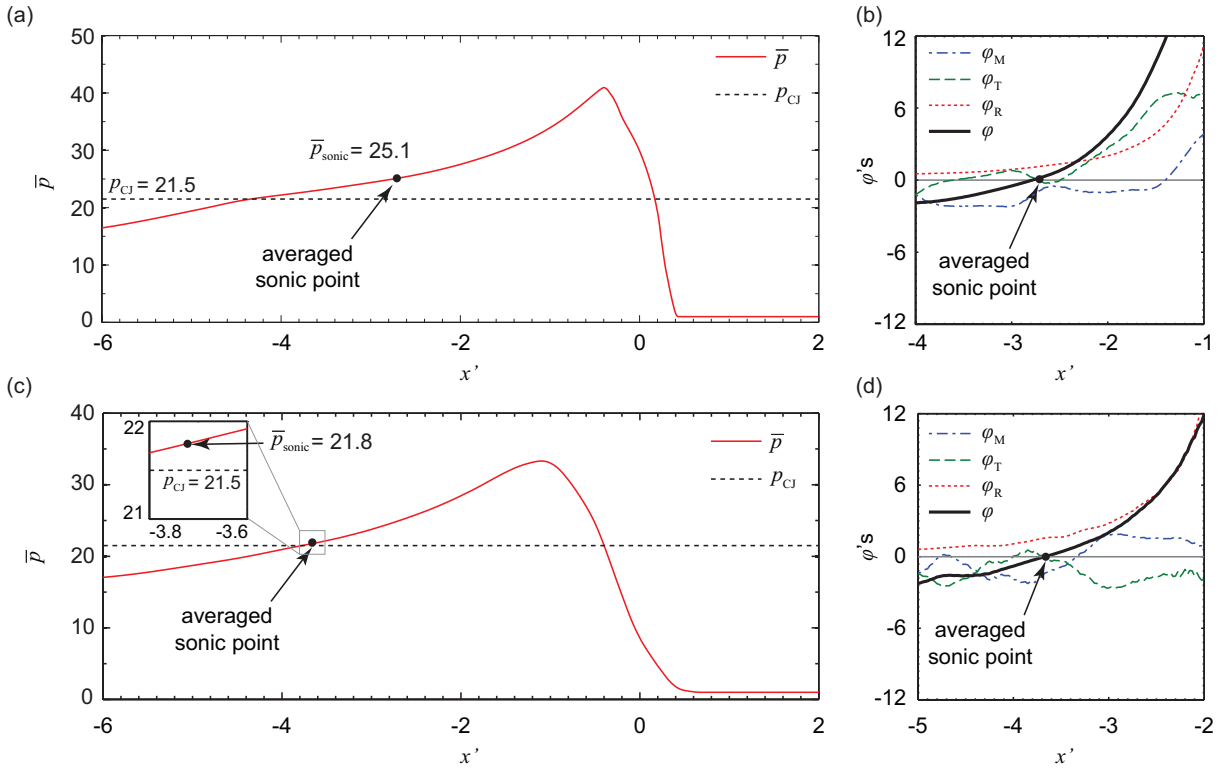

Figure 2.16: The spatial profiles of (a) averaged pressure plotted in wave-attached reference frame and (b) the terms of thermicity in the master equation (Eqs. D.3 and D.4) plotted in the vicinity of the averaged sonic point for the case with one-dimensional reactive layers, $\Gamma = 0.04$, and $L = 10$. The spatial profiles of (c) averaged pressure plotted in wave-attached reference frame and (d) the terms of thermicity in the master equation plotted in the vicinity of the averaged sonic point for the case with two-dimensional reactive layers, $\Gamma = 0.04$, and $L = 10$.

non-equilibrium state associated with significant mechanical and thermal fluctuations is identified at the location where the averaged flow encounters the effective sonic surface.

2.2.4.2 Evaluation of τ_c

As shown in Sec. 2.2.3 (Fig. 2.15), a continuous transition of the propagation speed from V_{CJ} to the plateau super-CJ value is found as Γ decreases from 1 to 0 or L increases. An analogous spectrum of propagation regimes is identified in flame propagation in reactive media with spatially discrete or point-like sources. [27, 28, 29, 30, 31, 32, 77, 78] A physical parameter, τ_c, which is the ratio between the heat release time of each source and the characteristic time of heat diffusion between neighboring sources, is used to characterize the corresponding flame propagation regime. Similarly, in this system of discrete source detonations, single-step Arrhenius kinetics with a finite reaction rate permit us to measure the time over which a discrete source (layer or square) releases its chemical energy, t_r. Knowing the trajectory of the leading shock wave, the time required for the wave front to travel from one discrete source to the next, t_s, can also be measured. Thus, the ratio between t_r and t_s, i.e., $\tau_c = t_r/t_s$, can be evaluated. As the physical significance of τ_c related to the wave propagation regimes in discretized reactive media is discussed in Sec. 2.2.5, this subsection is only focused on presenting an approach to post-processing the simulation data in order to evaluate τ_c.

The time evolution of the reaction progress variable Z can be plotted in an x'-t diagram where x' is the spatial coordinate in a wave-attached reference frame. This x'-t diagram of Z can be directly constructed from the simulation results for the one-dimensional cases. For the two-dimensional simulations, the flow field of Z at each time step first needs to be spatially averaged along the y-axis to obtain a one-dimensional profile. Then, the x'-t diagram can be constructed based on these averaged profiles of Z from the two-

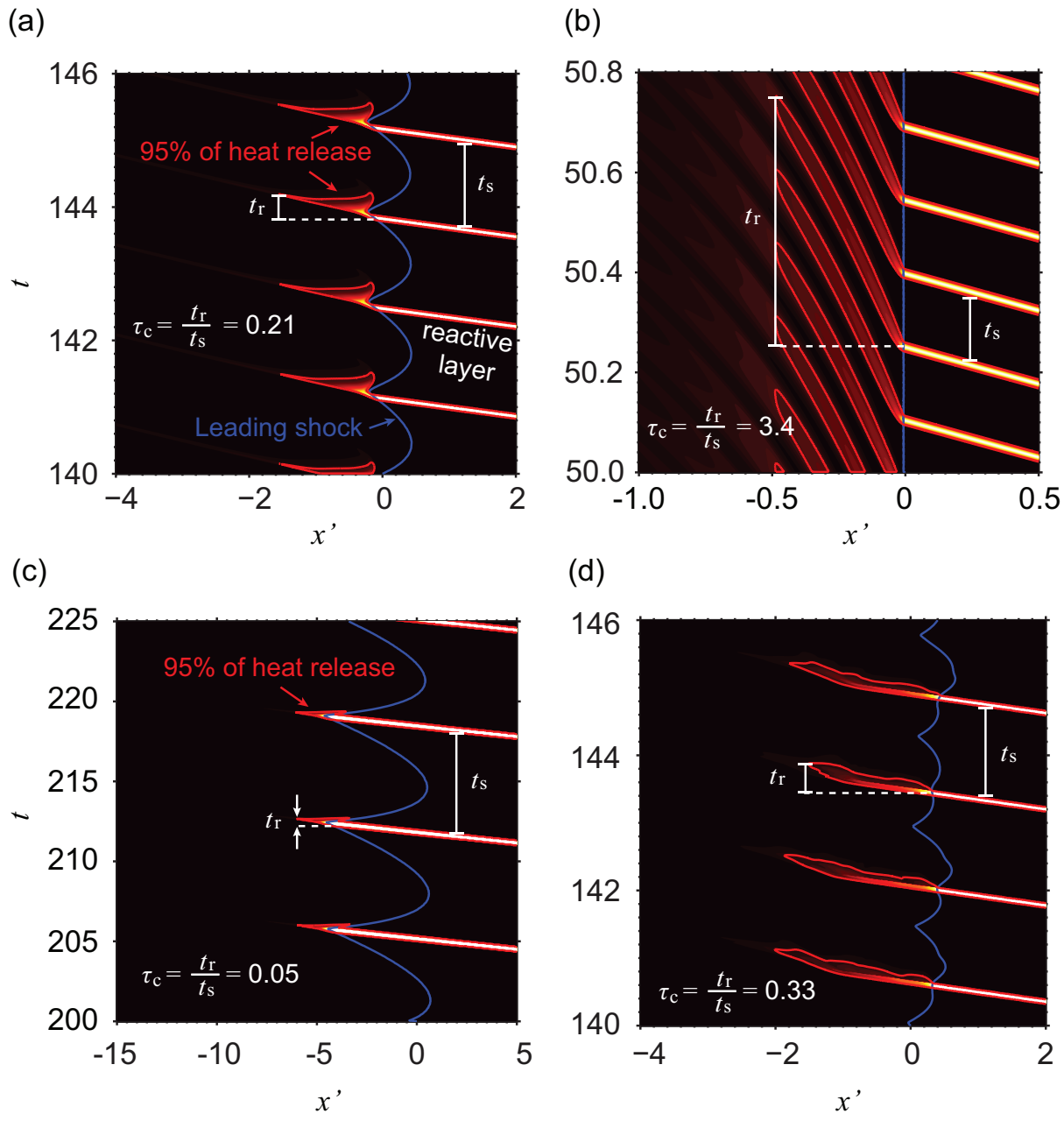

Figure 2.17: Contours of reactive progress variable Z plotted in x'-t diagrams for the cases with one-dimensional reactive layers with (a) $L = 10$, (b) $L = 1$, (c) $L = 50$, (d) two-dimensional reactive layers with $L = 10$, and $\Gamma = 0.04$.

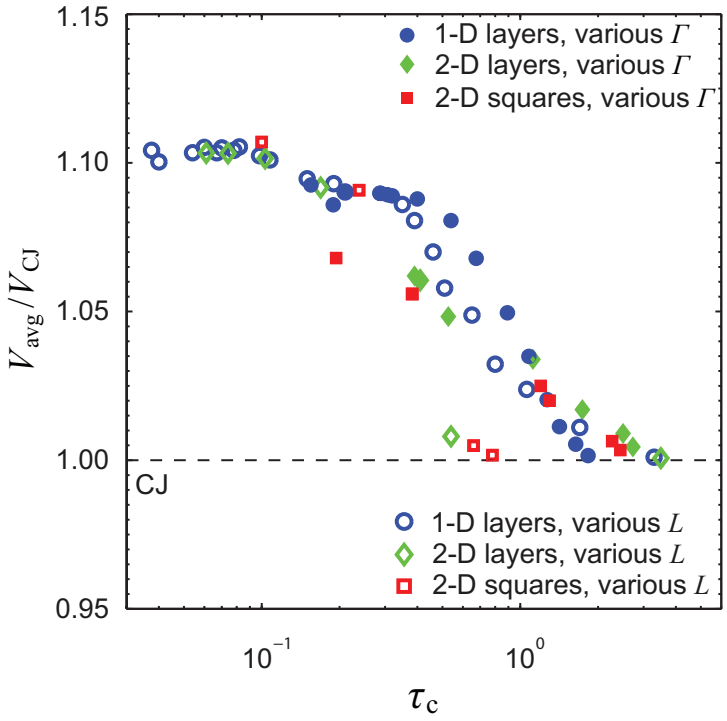

Figure 2.18: For cases with one-dimensional reactive layers (blue circles), two-dimensional reactive layers (green diamonds), and two-dimensional reactive squares (red squares), average wave propagation velocity normalized by CJ velocity as a function of τ_c. The open symbols are for the cases with $\Gamma = 0.04$ and various L; the solid symbols are for the cases with $L = 10$ and various Γ.

dimensional simulation results. The x'-t diagrams of Z for cases with various model parameters are shown in Fig. 2.17.

Figure 2.17(a), the case with one-dimensional reactive layers ($\Gamma = 0.04$ and $L = 10$), is taken in this subsection as an example to explain how τ_c is determined. The color contour of Z is scaled from bright to dark as $Z = 1$ to 0. Thus, the bright stripes on the right of this figure are the loci of unreacted discrete layers moving (leftwards) towards the leading shock whose trajectory is plotted as the blue curve. The shock transit time between discrete sources t_s can be obtained by measuring the vertical spacing between two bright stripes. The dark zones separating the discrete layers are the inert regions.

The areas of gradual color change emanating from where the leading shock encounters the reactive layers indicate the energy release. The areas of energy release are bounded by a thin red outline, which is the iso-contour of $Z = 0.05$, indicating that 95% of the chemical energy initially stored in each source is released within the bounded zone. The reaction time t_r of each discrete source can be measured as the vertical spacing between the locus of shock-source intersection and the upper bound (in time) of the 95% heat release zone. Although this technique of determining t_r is somewhat arbitrary, it should be sufficient to characterize the wave propagation regimes as long as this measurement is consistently performed in this study. The results of average propagation velocity normalized by the CJ value for the scenarios of one-dimensional reactive layers (blue circles), two-dimensional reactive layers (green diamonds), and two-dimensional reactive squares (red squares) with various Γ (solid symbols) and L (open symbols) can thus be plotted as a function of τ_c as shown in Fig. 2.18.

2.2.5 Discussion

The results presented in this paper show that, in an adiabatic system of discretized energy sources governed by single-step Arrhenius kinetics, waves can propagate, in a self-sustained manner, at a speed that is significantly greater than the CJ value of a homogeneous system with the same amount of overall heat release and without the support of a piston. Based on the analysis presented in Sec. 2.2.4.1 for selected one- and two-dimensional cases, this nearly 10% super-CJ wave propagation can be interpreted as a weak detonation where the flow remains in a non-equilibrium state upon reaching the effective sonic surface. Note that, of all detonation solutions satisfying the conservation laws, the CJ solution with a complete equilibrium state at the sonic surface corresponds to the slowest possible wave speed. By evaluating the terms which comprise the total

thermicity in the master equation (Eq. D.3) based on the Favre-averaged properties, the non-equilibrium condition at the sonic point is attributed to the intense fluctuations in momentum and total energy of the flow. The generalized-CJ condition, i.e., a vanishing thermicity ($\phi = 0$) at the average sonic point ($u^* + c^* = 0$), is satisfied owing to the balance between the exothermic chemical reaction and the mechanical and thermal fluctuations. The finding of this study incorporating a more realistic, state-dependent reaction model complements the study of Sec. 2.1, verifying that the classic CJ criterion assuming a homogeneous medium based on averaged properties is not always applicable to predict the wave propagation speed in a spatially inhomogeneous system, and further suggesting that the resulting super-CJ propagation is independent of the particular energy deposition mechanism.

In Sec. 2.1, where an instantaneous, state- and shock strength-independent mechanism of energy deposition was considered, the spatial coordinate can be normalized by the regular spacing between two consecutive sources. In other words, source spacing L does not affect the wave propagation behavior. In that study, the ratio of specific heat capacity γ and the spatial discreteness parameter Γ are the only two factors determining the deviation of average wave speed away from the CJ solution. In the current study, however, as a finite-rate, state-dependent reaction rate is incorporated, an additional length scale, i.e., the reaction zone length of a detonation in the homogenized system, comes into play. This physical length scale is a function of E_a, Q, and γ, but independent of source spacing. The source spacing relative to the intrinsic reaction zone length therefore affects the resulting wave propagation behavior.

The effect of L on the average wave speed can be identified in Fig. 2.15(b). For a fixed spatial discreteness $\Gamma = 0.04$, V_avg increases from V_CJ to a plateau value that is

10% greater than V_{CJ} as L increases from 1 (i.e., source spacing equals half-reaction-zone length) to 200. As Γ decreases from 1 to the limit of $\Gamma \to 0$, a similar trend of V_{avg} increasing from the CJ speed to the same plateau value is shown in Fig. 2.15(a). These two asymptotic limits of Γ can be understood as follows: When $\Gamma = 1$, the source size equals the source spacing; the system is thus continuous, resulting in a CJ propagation speed. As $\Gamma \to 0$, the discrete sources tend to be spatial δ-functions and release energy nearly instantaneously. In this limit, each source generates forward- and backward-running blast waves. The forward running blast triggers the next source, so the wave propagates via a mechanism of sequentially initiated blast waves by the point sources, which can be qualitatively captured by the heuristic model based on the construction of point-source blast solutions in the Appendix B. Since the variation of V_{avg} as a function of L is between the same asymptotic limits as those of Γ, the underlying mechanisms at these limits must have an equivalent effect on the wave propagation. When L is small, i.e., on the order of the intrinsic half-reaction-zone length, these spatial inhomogeneities are too fine so that the reactive medium is effectively homogenized. In the other limit, where L is hundreds of times larger than the half-reaction-zone length, the time of a discrete source being processed by the leading shock and releasing energy is much shorter than the time required for the leading shock to travel from a source to the next. Hence, given the large time scale of wave propagation, the energy of one source is released effectively instantaneously, and the overall picture of this wave propagation reverts to the case of sequentially triggered point blasts. Note that, since neither losses nor a chemical kinetic cutoff are considered in this system, further increasing L will not qualitatively alter the resulting wave dynamics or lead to quenching.

The continuous spectrum of the wave solutions from the effectively homogeneous CJ propagation to a sequence of point-source blasts can be rationalized with the assistance

of τ_c evaluated via the method presented in Sec. 2.2.4.2. In other words, the effect of L and Γ on the wave propagation speed can be reconciled by considering the τ_c parameter. The x'-t diagram of Z-contour shown in Fig. 2.17(b) is for the case of one-dimensional reactive layers with $\Gamma = 0.04$ and $L = 1$, where the reaction time t_r of a source is much longer than the shock transit time t_s, i.e., τ_c is significantly greater than unity. This case corresponds to the scenario wherein the very small scale discrete sources are effectively homogenized, and results in a CJ wave speed. Keeping Γ fixed at 0.04 and increasing L to 10 (for the one-dimensional case), as shown in Fig. 2.17(a), t_r is still finite but smaller than t_s. In this case, where $\tau_c = 0.21$, V_{avg} reaches an intermediate value that is approximately 8.5% greater than V_{CJ}, but still less than the 10% super-CJ plateau value. For the one-dimensional case with $\Gamma = 0.04$ and L increased to 50, as shown in Fig. 2.17(c), t_r is significantly smaller than t_s, i.e., $\tau_c = 0.05$. The wave propagation in this case is thus via the mechanism of sequentially triggered point-source blasts, and a plateau super-CJ speed is observed.

As shown in Fig. 2.15, the resulting V_{avg} values in the one- and two-dimensional cases with reactive layers coincide at the CJ and plateau super-CJ limits, but differ over the transitional range of Γ and L. Over this range, the V_{avg} values of the two-dimensional cases are smaller than that of the one-dimensional cases. This difference is due to the fact that, while the detonation in the one-dimensional homogeneous system is stable for the selected parameters ($Q = 50$, $\gamma = 1.2$, and $E_a = 20$) [72], it is intrinsically unstable in a homogeneous two-dimensional system. [73] In addition, the stability analysis which indicates that this system should be stable in one-dimension only applies to homogeneous media. As the source energy is concentrated into reactive layers or squares, the local heat release increases by a factor of $1/\Gamma$, likely promoting the development of instability. For the cases with large Γ and small L, which are not severely inhomogeneous, the intrinsic

detonation instabilities are likely developed in a two-dimensional system. As shown in the two-dimensional sample result in Fig. 2.13(b), after the instabilities have fully developed, the leading shock front becomes transversely wavy, and thus processes different parts of the discrete reactive layer at different times and with different strength. The spatially smeared shock front in the $\bar{p}$ profile for the two-dimensional case shown in Fig. 2.16(c) is a result of these developed instabilities. Hence, the heat release of a discrete layer is also temporally and spatially smeared out, having a homogenizing effect on the energy deposition. This effect can be verified in the x'-t diagram of Z-contour for the two-dimensional case with $\Gamma = 0.04$ and $L = 10$ based on the spatially averaged one-dimensional wave profiles (Fig. 2.17(d)). The τ_{c} for this case is determined as 0.33, which is greater than that for the one-dimensional case with the same Γ and L, i.e., $\tau_{\mathrm{c}} = 0.21$, as shown in Fig. 2.17(a) and (d). Correspondingly, the V_{avg} resulting from the above-mentioned two-dimensional case is 6.1% greater than V_{CJ} while that for the one-dimensional case is 8.5% greater than V_{CJ}. Therefore, as an alternative to Γ and L, τ_{c} can be used as a general parameter that quantifies the effect of energy discretization on the wave propagation speed. As demonstrated in Fig. 2.18, the results V_{avg} for both one- and two-dimensional cases with various Γ and L follow qualitatively the same trend when plotted as a function of τ_{c}.

In this study, the super-CJ wave propagation is identified in the cases with a two-dimensional arrangement of reactive squares. The super-CJ plateau value and the dependence of the deviation from the CJ propagation on the spatial discreteness Γ and spacing between reactive squares L is qualitatively the same as that for the cases with reactive layers. This result suggests that the super-CJ wave propagation and its underlying mechanism due to the spatial inhomogeneities are unlikely an artifact only arising from a one-dimensional system or a system with a one-dimensional, laminar-like arrangement

of discrete sources (i.e., reactive layers), but a rather fundamental consequence of multi-dimensionally distributed inhomogeneities on the propagation of reaction waves.

Although this study considers simplified scenarios of spatial inhomogeneities, it may capture some details of a detonation propagating in the combustion chamber of a rotating detonation engine with discretely located fuel/oxidizer injection. The scenario with reactive layers resembles the RDE design where detonable gases are axially injected into the annular combustion chamber such as those studied in Refs. [79, 80, 81]; the RDEs with impinging injection of non-premixed fuel and oxidizer [82, 83] can be conceptualized as the scenario with discrete reactive squares. The key finding of this current work may explain the 5% super-CJ detonation velocity recently reported by Fujii *et al.* [80] for the numerical simulations of a detonation wave propagating in a RDE combustion chamber with relatively widely spaced, premixed gas injection.

Drawing inspiration from Vasil'ev and Nikolaev's heuristic model [26], which utilized interacting point-source blast waves to mimic detonation cell structure, the two-dimensional arrangement of highly concentrated, reactive squares considered in this study can be used to investigate the wave dynamics of cellular detonations in future efforts. By selecting a source spacing L that is similar to typical detonation cell sizes, the wave structure induced by imposing spatial inhomogeneities can be hypothesized to have a similar effect on the overall propagation behavior and critical limits as those resulting from the intrinsic cellular structure. Spatially regular and random distributions of inhomogeneities can potentially be used to induce wave structures similar to that in weakly and strongly unstable mixtures, respectively.

Further development of this detonation system with spatial inhomogeneities will also

be carried out by incorporating a multi-step, chain-branching reaction scheme that provides a kinetic quenching mechanism [84, 85], i.e., a critical temperature below which the exothermic reaction rate is decreased significantly (or quenches). With such a system, it would be possible to examine critical detonation phenomena, for example, a propagation limit in source spacing L beyond which the blast wave generated by a discrete source decays to a shock that is too weak to trigger the exothermic reaction of the subsequent sources.

2.2.6 Conclusions

The effect of spatial inhomogeneity in the reaction progress variable upon detonation propagation, while maintaining the overall energy release of the medium as constant, has been studied via numerical simulations in one-dimensional systems and in two-dimensional systems of reactive layers and squares governed by activated, Arrhenius kinetics. The average wave speeds are observed to agree with the predictions of the classical Chapman-Jouguet criterion provided that the time scale of the energy release is greater than the time required for the leading shock to propagate between sources. This regime is observed if the medium is nearly homogeneous (i.e., with the gaps of inert media being smaller than the reactive areas) or when the spacing between the reactive layers is small in comparison to the half reaction zone length of a detonation in the equivalent homogeneous media. In sufficiently inhomogeneous media, wherein the spacing between reactive regions is greater than the inherent reaction zone length, average wave propagation speeds significantly greater than the CJ velocity of the equivalent homogenous medium are observed (up to 10%). Based on spatial and temporal averaging of the numerical results, the super-CJ waves can be interpreted as weak detonations wherein the generalized CJ condition applies at a state of non-equilibrium existing at an effective sonic point inside the wave

structure, rather than at an equilibrium point located at the end of the reaction zone in the classical CJ detonation criterion. The non-equilibrium condition in the flow is attributed to persistent fluctuations in momentum and total energy resulting from the intense shock waves generated by the concentrated pockets of energy release.

Chapter 3

Effect of spatial inhomogeneities on propagation limit of detonations with compressible confinement

The propagation of gaseous detonations in a charge with an inert, compressible confinement, as illustrated in Fig. 3.1, has been an intriguing problem for researchers over the past 60 years. This problem, considered as an analog to detonations propagating in condensed-phase explosives with yielding confinement, was first studied in the 1960s in order to examine the influence of the confining material on the propagation dynamics. [86, 87, 88] In the pioneering studies of this problem, the propagating detonation wave was theoretically depicted as a planar leading shock followed by laterally expanding flow, in spite of the curve front revealed by schlieren images. [86, 87, 88] The discover of cellular structure of gaseous detonations made around the same time [8] also complicated the understanding of the structure of the flow field for this problem. Over the following two decades, deeper and more quantitative insights into the cellular wave structure of gaseous detonation was gained. In the 1980s, creating cylindrical gas columns of det-

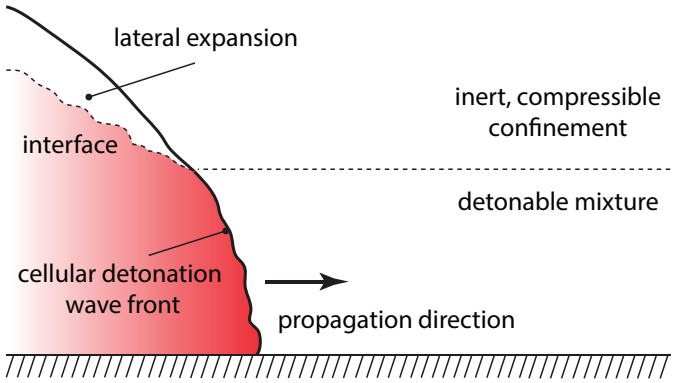

Figure 3.1: Conceptual illustration of a cellular detonation wave propagating in a mixture of detonable gases confined by an inert gas layer.

onable mixtures bounded by inert gases via various experimental techniques, researchers revisited this problem with their focus upon linking the critical charge diameter (d^*) for a self-sustained propagation to other dynamic parameters of gaseous detonations, such as detonation cell size (λ) and critical diameter for a transition to unconfined detonation (d_c). [89, 90, 91, 92]

As an upsurge in developing rotating detonation engines (RDEs) arose since the turn of the new century, the attention of researchers has again been drawn to the dynamic behavior of cellular detonations interacting with an inert gas confinement. A detonation wave spinning in the annular combustion chamber of an RDE experiences lateral expansion in the axial direction of the engine; hence, determining the critical height (h^*) of the combustible mixture injected into the chamber for a detonation wave to continuously propagate is crucial for the RDE design. [93, 94] To this end, recent studies on detonations with an inert gas confinement have been focused on rectangular geometries, wherein detonable gases are initially separated from [95, 96, 97, 98, 99, 100, 101, 102] or dynamically injected [80, 103] into an inert medium, simulating the combustion scenarios arising from RDEs.

Due to the difficulty in experimentally preparing the reactive and inert gas mixtures under consistent initial conditions, experimental values of d^* or h^* have not been extensively reported in the literature. In Vasil'ev and Zak's experiments, a detonation wave propagates in a cylindrical jet of reactive gases surrounded by inert gases without a physical separation at the reactant-inert interface. [91] These authors determined a critical diameter $d^* \approx$ 40-60λ for various detonable mixtures. For experimental set-up with a physical separation between the reactive and inert gases, significantly smaller values of d^*/λ or h^*/λ have been reported in the literature. Murray and Lee determined a critical diameter $d^* \approx$ 7.5-15.2λ for a detonation wave to self-sustainably propagate in cylindrical plastic bags filled of explosive gases. [89, 90] In Rudy *et al.*'s work, a critical thickness $h^* \approx$ 3-5λ was found for semi-confined (confined by a rigid wall on one side and a layer of inert gases with a thin-film separation on the other side) hydrogen/air and hydrogen/methane/air mixtures. [96, 97] This nearly one-order-of-magnitude discrepancy can be explained as that the presence of a film significantly increases the confinement strength comparing to merely a layer of inert gas, thus, suppresses the expansion flow to a certain extent, allowing a detonation wave to propagate into smaller charges. Based on these limited experimental data, however, whether or how the critical charge size varies with the nature of the reactive mixture (e.g., activation energy, mixture stability, etc.) and the inert confinement (e.g., acoustic impedance) still remains unclear.

Two recent studies put the complex dynamics of this problem under closer scrutiny via computational simulations. [99, 100] Houim and Fievisohn's work is focused on illustrating the mechanism through which the wave interaction at the reactant-inert interface influences the overall propagation behavior. [99] They found that, at a height of the reactant layer about $h \approx$ 4-5λ, the detonation wave propagates if the acoustic impedance

of the confining layer is greater than that of the reactant, and the detonation fails if the impedance nearly matches at the interface. Since the activation energy $E_a = 39.19$ was fixed in their work, the dependence of h^*/λ on E_a or cell regularity was not examined in this study. In Reynaud *et al.*'s work, various activation energies, characterized as ranging from regular to mildly irregular mixtures, are considered. [100] They showed that the resulting h^* increases from 1 to 20 times the cell size in the ideal case as E_a increases from 10 to 38.23. This trend is seemingly opposite to the dependence of the critical diameter for a transition to unconfined detonation normalized by detonation cell size, i.e., d_c/λ, on the activation energy, or cell regularity, of the mixture. There is perhaps a large uncertainty in these simulation results due to the challenge in numerically resolving the naturally developed, spatially inhomogeneous wave structure and energy release in the reaction zone (as discussed in Ch. 1).

A more important aspect of this problem is that examining how a cellular detonation responds to lateral losses allows one to better understand the mechanism of propagation. Without losses, the detonation velocity is always the ideal CJ velocity (or excess above V_{CJ} in highly discrete cases). With the yielding confinement, however, the propagation velocity exhibits a deficit. Examining how this deficit from V_{CJ} increases as the reactive layer thickness approaches a critical value h^* is a measure of the effective activation energy governing the dynamic behavior of detonation waves. It is hence of importance to investigate cellular detonation waves interacting with compressible confinement in order to probe the effective activation energy of the actual transient, multidimensional structure of detonation waves.

The aim of this current study is to further elucidate the mechanism of the spatially inhomogeneous nature of gaseous detonations responding to the losses resulting from the

lateral expansion in the reaction zone. In this chapter, the approach of imposing spatial inhomogeneities is extended to a two-dimensional system of a detonable gaseous mixture confined by an inert gas layer. This approach was recently explored in Li *et al.*'s work where the inhomogeneities were introduced as a sinusoidal variation in the initial density and temperature of the reactive medium. [35] In this study, the inhomogeneities are introduced as a spatially random distribution of discrete reactive sources where the reactants are highly concentrated, similar to those used in previous chapters. Simulations based on the two-dimensional, reactive Euler equations are performed for both homogeneous and randomly inhomogeneous cases. The influence of activation energy and the characteristic of the imposed sources on the near-limit propagation is investigated.

This chapter is organized as follows. In Sec. 3.1, the problem for simulation is stated. Section 3.2 describes the numerical methodology used to solve the governing equations. The simulation results of wave structures, the history of instantaneous propagation speed, the averaged propagation speed as a function of the reciprocal of the reactive layer thickness $1/h$, and the critical thickness for self-sustained propagation h^* as a function of spatial discreteness Γ are presented in Sec. 3.3. In Sec. 3.4, a theoretical model based on the ZND-type wave structure is described. The findings based upon the simulation results are discussed in Sec. 3.5 and summarized in the Conclusions (Sec. 3.6).

3.1 Problem statement

The reactive system consists of an inviscid, calorically perfect gas (i.e., with a constant ratio of specific heat γ). The gasdynamics of this system is described by the two-dimensional reactive Euler equations in a lab-fixed reference frame with flow and state

variables non-dimensionalized with respect to the pre-shock, initial state (same as the governing equations Eqs. 2.20 and 2.21 formulated in Sec. 2.2). For a homogeneous reactive system, the specific total energy is defined as $e = p/(\gamma-1)\rho + (u^2+v^2)/2 + ZQ$, where Z is the reaction progress variable, which varies between 1 (unreacted) and 0 (fully reacted), and Q is the dimensionless energy released by the complete chemical reaction. Applying the CJ criterion, the velocity (V_{CJ}) of a detonation wave propagating in a homogenous reactive system with the energy release Q can be calculated via Eq. 2.1. In order to represent a typical gaseous detonable mixture, $Q = 50$ and $\gamma = 1.2$ are chosen for all the simulations in this chapter. The reaction rate $\Omega = \partial Z/\partial t$ is governed by single-step Arrhenius chemical kinetics as Eq. 2.22. Three different values for the dimensionless activation energy, i.e., $E_{\mathrm{a}} = 10$, 20, and 30, are considered, and the value of preexponential factor k in the reaction rate is accordingly selected so that the half-reaction-zone length $l_{1/2}$ in the ideal ZND solution for the homogeneous case is unity.

The initial configuration of the simulation system is illustrated in Fig. 3.2(a). The red region on the bottom is the reactive gas layer with a thickness h; the blue region on the top is the inert gas layer with a thickness h_{I}, where Z equals 0 initially. The critical thickness of the reactive layer below which a detonation wave fails to propagate is denoted as h^* in this chapter. A high-pressure region near the left end of the simulation domain, as shown in Fig. 3.2(a), is used to initiate a rightward-propagating detonation wave. For the cases with a low activation energy, i.e., $E_{\mathrm{a}} = 10$ and 20, the pressure and density in the initiation zone was set equal twice the corresponding CJ state properties, i.e., $p = 2p_{\mathrm{CJ}}$ and $\rho = 2\rho_{\mathrm{CJ}}$; for the cases with a relatively high activation energy, i.e., $E_{\mathrm{a}} = 30$, the pressure and density in the initiation were set to $p = 5p_{\mathrm{CJ}}$ and $\rho = 2\rho_{\mathrm{CJ}}$. The rest of the simulation domain was initialized with uniform, density, and particle velocity as $p = 1$, $\rho = 1$, $u = 0$, and $v = 0$.

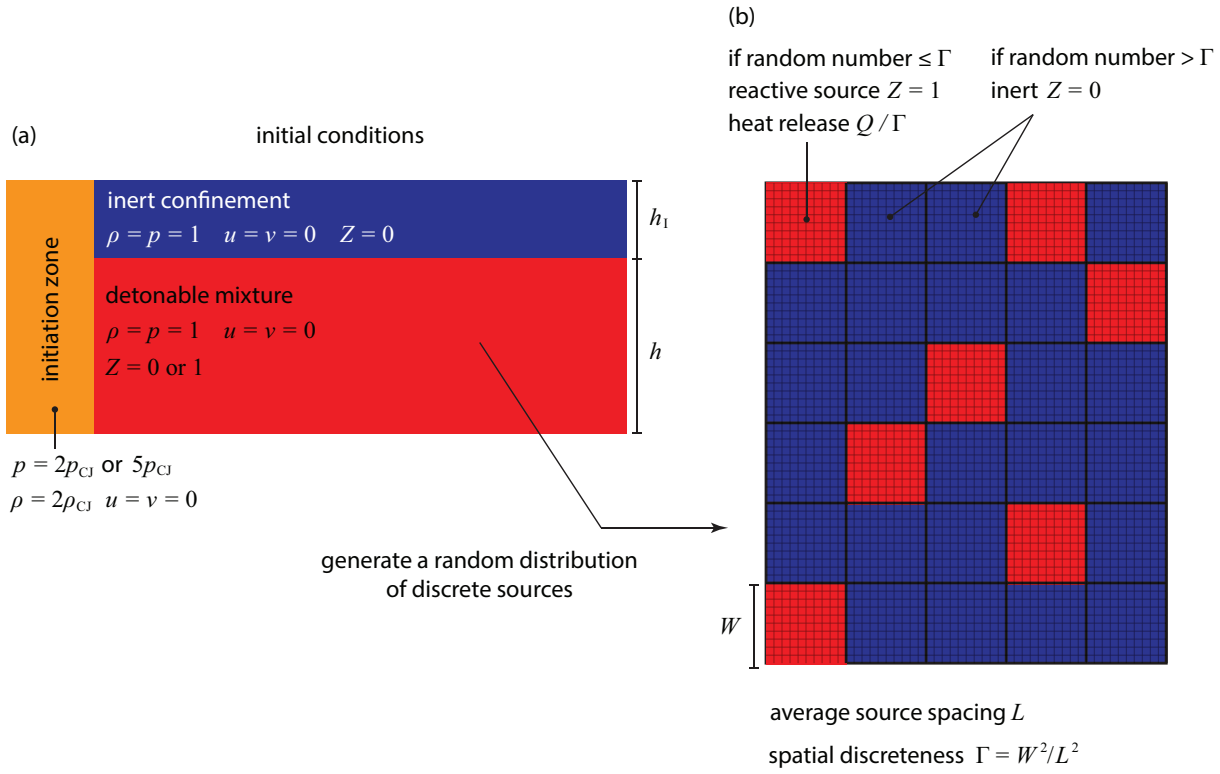

Figure 3.2: Schematic illustration of (a) the initial conditions for the simulation system and (b) the method used to initialize a spatially random distribution of discrete sources.

The spatial inhomogeneities are introduced to the simulation system as spatially discrete reactive squares, similar to those described in Sec. 2.2.1 (Fig. 2.11(b)). The reaction progress variable Z is initialized as 1 in these reactive sources and 0 in the inert regions separating them. Different from a regularly spaced array of sources introduced in Sec. 2.2, square sources of the same size are randomly distributed in the reactive layer. With a prescribed average spacing between neighboring sources L, the spatial discreteness parameter Γ can be defined as the ratio between the size of a source and the inert area surrounding it, i.e., $\Gamma = W^2/L^2$. In the limit of $\Gamma \to 1$, the reactive layer becomes homogeneous where the initial distribution of Z is uniform; in the limit of $\Gamma \to 0$, a discrete source approaches a δ-function in space, namely, a point source of energy. In order to maintain the average

specific energy release Q the same as that in the homogeneous cases, the actual energy release associated with each discrete source must be increased according to the prescribed spatial discreteness Γ. For the cases with spatial inhomogeneities, the specific total energy is formulated as $e = p/(\gamma - 1)\rho + (u^2 + v^2)/2 + ZQ/\Gamma$. The method used to randomize the positions of the discrete sources while maintaining a prescribed value of the overall discreteness Γ is described in the next section.

3.2 Numerical methodology

The simulation code used to solve the two-dimensional reactive Euler equations is based upon a uniform Cartesian grid. The MUSCL-Hancock scheme with the van Leer nonsmooth slope limiter and a Harten-Lax-van Leer-contact (HLLC) approximate solver for the Riemann problem was used. This code is implemented in Nvidia's CUDA programming language. The simulations were performed on a Nvidia Tesla K40M GPU computing processor. The Strang splitting method was adopted to treat separately the hydrodynamic process and the reactive process. This numerical scheme is thus of second-order accuracy in space and time.

In each case where a detonation wave successfully propagated, the length (in x-direction) of the entire simulation domain was approximately 3000 times the half-reaction-zone length $l_{1/2}$ for an ideal, homogeneous case. The technique of an advancing computational window, which were developed in several recent studies for simulating detonation waves propagating over a long distance [104, 35, 3, 100], was used in this study in order to reduce the computational cost. Instead of the entire domain, the simulations were only performed in a window that enclosed the leading wave complex. Once the leading shock front nearly reached the end of the computational window (i.e., $20l_{1/2}$ away from the right

boundary), the left and right boundaries of the window were advanced by half of the window size. A window size of $600l_{1/2}$ was used for all the simulations in this study and was verified to be sufficiently large to capture the reaction zone dynamics that contribute to the propagating wave front. On the top, left, and right boundaries of this computational window, a transmissive boundary condition is applied; on the bottom boundary, a reflecting boundary is applied to model a rigid confining wall. For all simulations reported in this chapter, a minimum thickness of the inert layer $h_{\mathrm{I}} = 50l_{1/2}$ was used to eliminate the influence of the top boundary on the propagation dynamics.

As the average source spacing L and the overall spatial discreteness Γ were prescribed, the width of each square source W was calculated as $W = \sqrt{\Gamma L^2}$. In order to initialize the simulation domain with a spatially random distribution of discrete sources, the reactive layer was first divided into squares of a size W^2 as marked by the thick black lines in Fig. 3.2(b). Note that a source-sized square is much larger than the size of the computational cells shown as thin gray lines. A random number N_{r} between 0 and 1 was assigned to each source-sized square using a uniform random number generator. As shown in Fig. 3.2(b), if a N_{r} is less than or equal to the spatial discreteness Γ, a reactive source is placed at this square, and all the computational cells within this square are initialized with $Z = 1$; otherwise, the square contains only inert material with $Z = 0$. A numerical resolution of 10 computational cells per half-reaction-zone length of the ideal homogeneous case, i.e., $l_{1/2}/\Delta x = 10$, was for most of the simulations reported in this Chapter. For selected cases, simulations were performed at different resolutions, i.e., $l_{1/2}/\Delta x = 5$, 20, and 30, for convergence tests. For the cases with very small discrete sources, e.g., $W = 1$ corresponding to $L = 10$ and $\Gamma = 0.01$, the minimum resolution ensures a sufficient number of computational cells within a square source (100 cells in the source with 10 cells along each side of the square).

3.3 Results

For all the simulations performed in this chapter, the average specific energy release $Q = 50$ and the ratio of specific heats $\gamma = 1.2$ are fixed. Three different values of activation energy, i.e., $E_a = 10$, 20, and 30, are considered. The value of the preexponential factor k is selected to be $k = 3.64$, 16.45, and 80.24 for $E_a = 10$, 20, and 30, respectively, so that the half-reaction-zone length $l_{1/2}$ in the ideal ZND solution for the homogeneous case equals to unity. Thus, all the length quantities reported in this section are in the unit of the corresponding $l_{1/2}$. The average source spacing L and the spatial discreteness Γ can be independently varied to quantitatively control the nature of the imposed spatial inhomogeneities. For each set of simulations with fixed E_a, L, and Γ, the only variable parameter is the thickness of the detonable layer h. Some selected results showing the wave structure for both homogeneous and inhomogeneous cases with various governing parameters are presented in Sec. 3.3.1. Sample plots of the propagation velocity histories resulting from different cases, which allows one to identify whether a detonation wave successfully propagates or not, are shown in Sec. 3.3.2. The measured average propagation velocity V_{avg} for all the cases considered in this study plotted as functions of the reciprocal of the detonable layer thickness, i.e., $1/h$, and the determined critical thickness h^* below which a detonation wave extinguishes are summarized in Sec. 3.3.3.

3.3.1 Wave structure

For $E_a = 20$, selected snapshots of the wave structures resulting from a homogeneous case and inhomogeneous cases with moderately discretized ($L = 10$, $\Gamma = 0.25$) and highly discretized ($L = 10$, $\Gamma = 0.01$) sources are shown in Fig. 3.3(a), (b), and (c), respectively. The top half of each subfigure is the contour plot of reaction progress variable Z; the

bottom half is the contour plot of pressure. The red area in the plot of Z is the reactive regions, or discrete sources in the inhomogeneous cases (Fig. 3.3(b) and (c)). The white dash lines indicate the interface between the reactive medium and the inert confinement. At the selected reactive layer thickness $h = 100$, a detonation wave can propagate in all three cases.

In the homogeneous case (Fig. 3.3(a)), transverse waves interacting with a globally curved leading shock front can be observed. A thin blue-green streak attached to the confinement interface can be seen on the Z-plot in Fig. 3.3(a), indicating that flow behind the leading shock laterally expand and some partially reacted gas moves away from the detonation complex. For the case with moderately discrete sources ($L = 10$, $\Gamma = 0.25$), as shown in Fig. 3.3(b), the resulting reaction-zone wave structure appears to be spatially more inhomogeneous than that from an initially homogeneous medium, featuring spatially localized high-pressure pockets near the leading shock front. A global curvature of the leading shock front can still be identified. While maintaining the average source spacing $L = 10$ the same, decreasing Γ to 0.01 makes the chemical energy possessed by the medium highly concentrated into the small ($W = 1$) discrete sources as shown in Fig. 3.3(c). The resulting localized high-pressure pockets behind the leading shock are separated by rather large low-pressure regions. Although the shock front propagating in the reactive layer can be distinguished from the oblique shock compressing the inert confinement, it does not seem to exhibit a globally curved shape.

Sample wave structures shown in Fig. 3.4 are for the case of lower activation energy $E_\mathrm{a} = 10$. With a homogeneous reactive medium, as shown in Fig. 3.4(a), the resulting wave front exhibits a nearly smooth curvature without any noticeable transverse waves. Discretizing the reactive medium into square sources with $\Gamma = 0.25$ and an average source

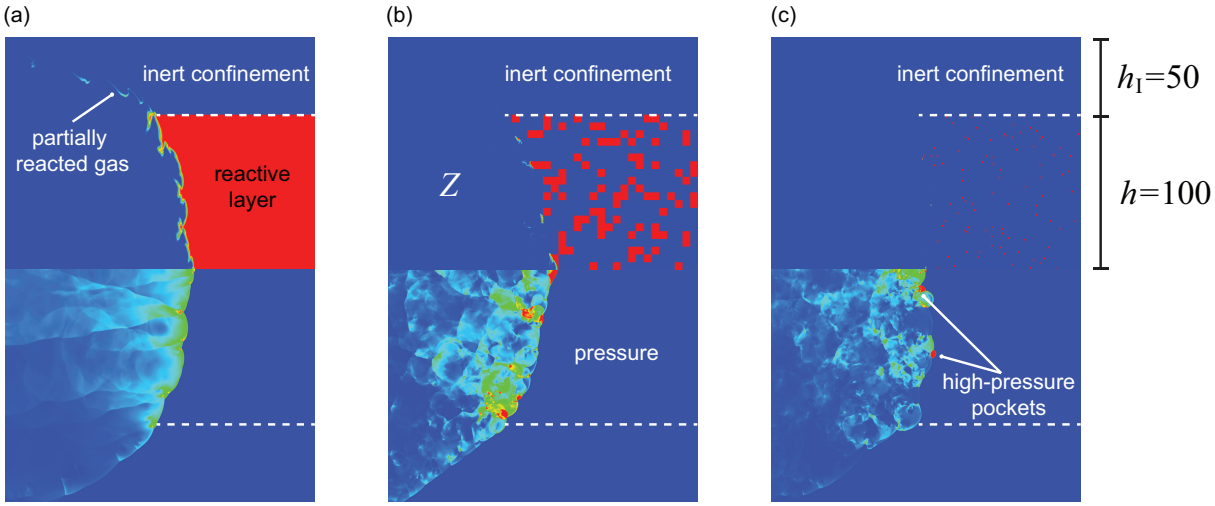

Figure 3.3: Wave structures (contour plots of reaction progress variable on top and pressure on bottom) for the cases with $E_a = 20$, $h = 100$, and (a) a spatially homogeneous reactive medium, (b) an inhomogeneous medium with moderately discrete sources ($L = 10$, $\Gamma = 0.25$), and (c) an inhomogeneous medium with highly discrete sources ($L = 10$, $\Gamma = 0.01$).

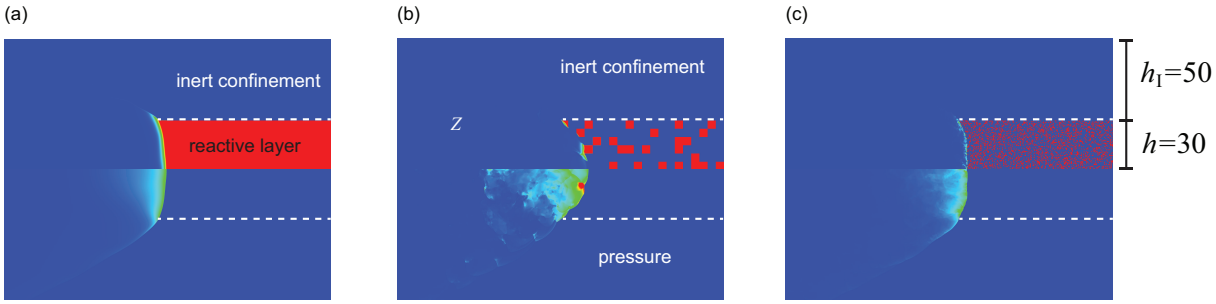

Figure 3.4: Wave structures (contour plots of reaction progress variable on top and pressure on bottom) for the cases with $E_a = 10$, $h = 30$, and (a) a spatially homogeneous reactive medium, (b) an inhomogeneous medium with discrete sources of $L = 10$, $\Gamma = 0.25$ and (c) $L = 1$, $\Gamma = 0.25$.

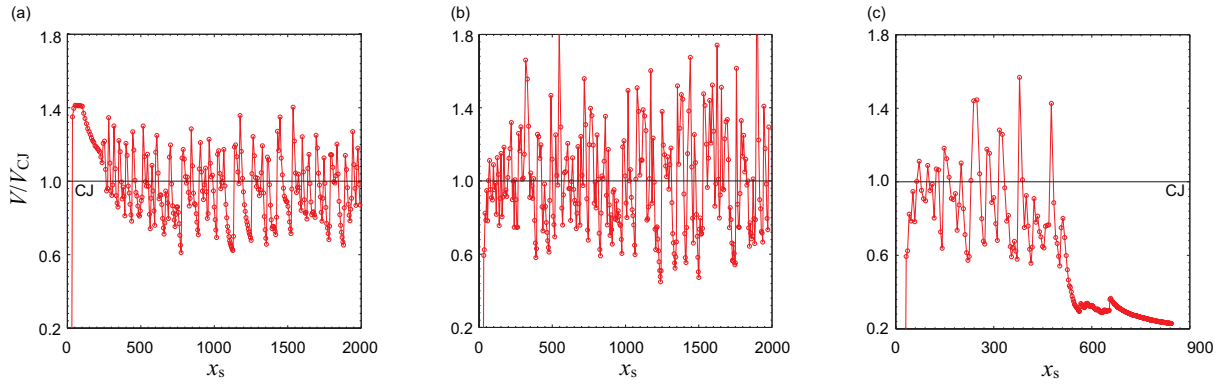

Figure 3.5: The history of instantaneous propagation velocity V normalized by the Chapman-Jouguet (CJ) velocity V_{CJ} as a function of the leading shock position x_s for $E_a = 20$: (a) a homogeneous case with $h = 80$; inhomogeneous cases ($L = 10$ and $\Gamma = 0.25$) with (b) $h = 80$ and (c) $h = 40$.

spacing $L = 10$, significantly larger than the intrinsic reaction-zone length for an ideal, homogeneous case, the wave structure becomes irregular as shown in Fig. 3.4(b). A localized high-pressure region can be observed near the leading shock front. While fixing the spatial discreteness $\Gamma = 0.25$ and reducing the average source spacing to $L = 1$, i.e., equals to the $l_{1/2}$ for the ideal ZND solution, a lightly rough wave front with an identifiable global curvature is recovered as shown in Fig. 3.4(c).

3.3.2 Velocity history

For each simulation run, the trajectory of the leading shock front $x_s(t)$ along the rigid wall (the bottom boundary of the simulation domain) can be recorded by finding the location where pressure increases to $p = 1.01$ from its initial value $p = 1$ every unity time step. The instantaneous propagation velocity V can then be calculated by numerically differentiating $x_s(t)$ over time. For some selected cases with $E_a = 20$, sample results of the instantaneous propagation velocity histories normalized by V_{CJ} as a function of the leading shock position are plotted in Fig. 3.5.

As shown in Fig. 3.5(a) and (b), for both homogeneous and inhomogeneous ($L = 10$ and $\Gamma = 0.25$) cases, respectively, with a reactive layer thickness $h = 80$, the detonation wave can self-sustainably propagate. The fluctuation in V for the homogeneous case shown in Fig. 3.5(a) has an average amplitude of approximately 80% of V_{CJ} (from 0.6 to $1.4V_{\mathrm{CJ}}$). For the inhomogeneous cases with $h = 80$ (Fig. 3.5(b)), V fluctuates over a much larger range from 0.5 to $1.8V_{\mathrm{CJ}}$. The inhomogeneous case shown in Fig. 3.5(c) has a much thinner reactive layer of $h = 40$. The resulting velocity history exhibits some fluctuations around V_{CJ} after the initiation process, and decreases to a very low value (below $0.2V_{\mathrm{CJ}}$). A velocity history as shown in Fig. 3.5(c) indicates that a detonation wave cannot successfully propagate at this reactive layer thickness, i.e., $h < h^*$, for the given set of parameters.

3.3.3 Average propagation velocity

For a case of simulation where the resulting detonation wave successfully propagates, although the instantaneous propagation velocity exhibits fluctuations due to the presence of inhomogeneities in energy release, a quasi-steady propagation velocity can be measured in an average sense over time or propagation distance. The total distance over which a detonation wave propagates in such a simulation run is approximately 3000. The average propagation velocity V_{avg} is measured over the second half of the propagation distance, i.e., from $x_{\mathrm{s}} \approx 1500$ to 3000, in order to avoid the influence of the initiation process on the measurement. The measured V_{avg} normalized by the CJ velocity are plotted as a function of the reciprocal of the reactive layer thickness $1/h$ for all the cases with $E_{\mathrm{a}} = 10$, 20, and = 30 in Fig. 3.6(a), (b), and (c), respectively. Two average velocities over smaller distances, i.e., $x_{\mathrm{s}} \approx 1500$ to 2250 and $x_{\mathrm{s}} \approx 2250$ to 3000, are also measured to provide information regarding the uncertainty in the measurement of V_{avg} and plotted as error

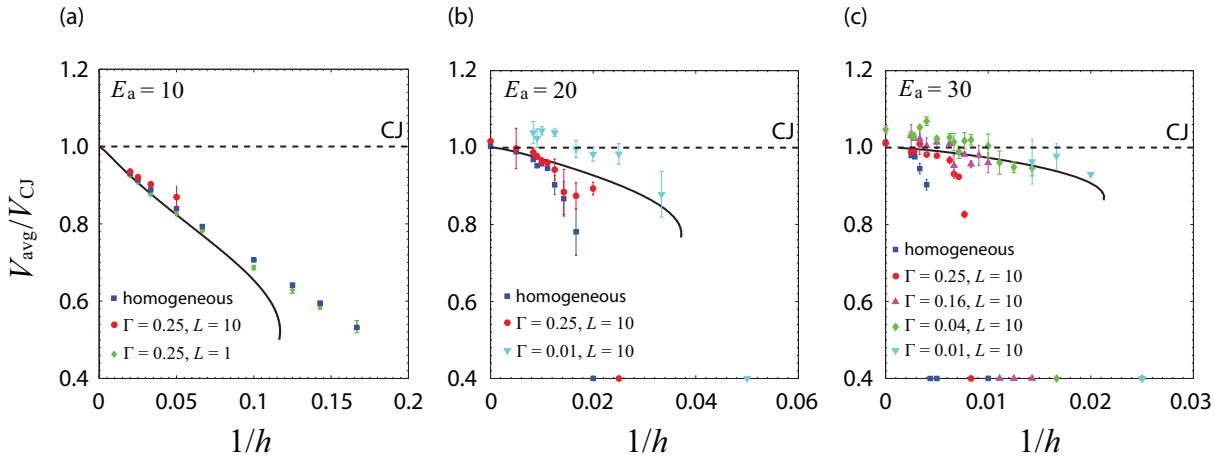

Figure 3.6: Average propagation velocity V_{avg} normalized by the CJ velocity as a function of the reciprocal of the reactive layer thickness $1/h$ for the cases with (a) $E_{\text{a}} = 10$, (b) $E_{\text{a}} = 20$, and (c) $E_{\text{a}} = 30$. The black curve on each plot is the theoretical prediction using the Wood and Kirkwood model with a curvature-based geometric construction of the wave front.

bars to the data points in Fig. 3.6.

The results plotted in Fig. 3.6(a) are for the cases with a very low activation energy $E_{\text{a}} = 10$. As the reactive layer thickness decreases (i.e., $1/h$ increases), the average velocity resulting from homogeneous and inhomogeneous cases decreases. The V_{avg} for the inhomogeneous cases with an average source spacing $L = 10$ (red circles) are slightly higher than those resulting from the homogeneous cases (blue squares). For the inhomogeneous cases with an average source spacing $L = 1$ (cyan diamonds), the resulting V_{avg} are very close to those for the homogeneous cases. For all three of these cases, the resulting V_{avg} decreases with h in a seemingly linear fashion; no case resulting in a quenched detonation is captured given this low activation energy $E_{\text{a}} = 10$.

In Fig. 3.6(b) and (c), the results of $V_{\text{avg}}/V_{\text{CJ}}$ plotted as a function of $1/h$ are for the cases with relatively higher activation energies, i.e., $E_{\text{a}} = 20$ and $E_{\text{a}} = 30$. For an

infinitely large reactive medium, i.e., an adiabatic detonation system without losses, the V_{avg} resulting from the homogeneous cases with both $E_{\text{a}} = 20$ and 30 is very close to V_{CJ} (with less than 1% difference). As the half thickness decreases, the velocity deficit from the CJ value becomes greater and greater until the propagation limit is encountered between $h = 60$ and $h = 50$ for $E_{\text{a}} = 20$ and between $h = 250$ and $h = 240$ for $E_{\text{a}} = 30$. For the cases with $E_{\text{a}} = 20$ and moderately discretized sources ($\Gamma = 0.25$, red circles in Fig. 3.6(b)), the resulting V_{avg} is not significantly different from that of the homogeneous cases at larges reactive layer thicknesses (small $1/h$); near the critical thickness marking the propagation limit, the V_{avg} for the $\Gamma = 0.25$ inhomogeneous cases are significantly greater than that for the homogeneous cases. For the case with $h = 50$, the resulting detonation wave can propagate in the inhomogeneous case but fails in the homogeneous case. For the cases with $E_{\text{a}} = 20$ and extremely discretized reactive sources ($\Gamma = 0.01$, cyan downward-pointing triangles in Fig. 3.6(b)), the resulting V_{avg} is significantly greater than the CJ velocity for the ideal, homogeneous system with the same amount of overall heat release; the propagation limit is encountered at a much smaller critical thickness between $h = 20$ and $h = 30$.

For the cases with $E_{\text{a}} = 30$ as shown in Fig. 3.6(c), the homogeneous cases (blue squares) result in a larger velocity deficit from V_{CJ} and reaches the propagation limit at a larger h comparing to those with a inhomogeneous medium. Making the reactive source sufficiently discrete (i.e., $\Gamma \leq 0.16$), the resulting V_{avg} are significantly greater than V_{CJ} at relatively large reactive layer thickness. As Γ decreases from 0.25 (red circles) to $\Gamma = 0.01$ (cyan downward-pointing triangles), a detonation wave can self-sustainably propagate into thinner and thinner reactive layers.

3.3.4 Critical thickness

With activation energies $E_a = 20$ and 30, the failure of detonation propagation is captured in the cases with both a homogeneous reactive layer and a random distribution of discrete sources as shown in Fig. 3.6(b) and (c). The critical thickness of the reactive layer h^* below which a detonation fails to propagate can thus be determined for these cases and summarized in Fig. 3.7. For each data point plotted on this figure, the upper error bar indicates the smallest thickness at which the simulation results in a self-sustained propagation, h^*_{go}; the lower error indicates the largest thickness at which a failure of propagation is identified, $h^*_{\text{no-go}}$. The critical thickness h^* is determined as the average value between h^*_{go} and $h^*_{\text{no-go}}$, i.e., $h^* = (h^*_{\text{go}} + h^*_{\text{no-go}})/2$. Note that there is no simulation performed exactly at the critical thickness h^*.

The simulation results of h^* at a numerical resolution of 10 computational cells per the half-reaction-zone length ($l_{1/2}/\Delta x = 10$) are plotted as a function of Γ, the spatial discreteness of the imposed inhomogeneous sources, with a fixed average source spacing $L = 10$ in Fig. 3.7(a). On the right end of this plot, $\Gamma = 1$ associates with the cases of a homogeneous reactive layer. The results with $E_a = 20$, plotted as circles, show that the critical thickness decreases from $h^* = 57.5 \pm 2.5$ to 25 ± 5 as the reactive medium is varied from spatially homogeneous to highly discretized, i.e., from $\Gamma = 1$ to $\Gamma = 0.01$. For the cases with $E_a = 30$, the resulting h^* (blue squares in Fig. 3.7) decreases from 247.5 ± 2.5 to 45 ± 5 as Γ decreases $\Gamma = 1$ to $\Gamma = 0.01$, exhibiting a steeper slope of change with the spatial discreteness of the reactive medium than that associated with the $E_a = 20$ results.

In Fig. 3.7(b), the simulation results of critical thickness h^* at different numerical resolutions are plotted as a function of activation energy E_a for the homogeneous $\Gamma = 1$

cases (marked as squares) and the most highly discretized cases with $\Gamma = 0.01$ and $L = 10$ (marked as circles). For the cases with $E_a = 20$, simulations have been performed at 4 different resolutions: $l_{1/2}/\Delta x = 5$ (green symbols), 10 (black symbols), 20 (blue symbols), and 30 (red symbols). For the cases with $E_a = 30$, simulations have been performed at 3 different resolutions: $l_{1/2}/\Delta x = 5$, 10, and 20. Note that, since the spatial discreteness for square reactive sources is defined as $\Gamma = W^2/L^2$, for the most highly discretized case with $\Gamma = 0.01$ and $L = 10$, there are 25, 100, 400, and 900 computational cells resolving each discrete source at numerical resolutions of $l_{1/2}/\Delta x = 5$, 10, 20, and 30, respectively.

For $E_a = 20$, homogeneous case shown in Fig. 3.7(b), as the numerical resolution was increases from $l_{1/2}/\Delta x = 10$ to 20, the result of h^* increases by approximately 9%; as the numerical resolution was increases from $l_{1/2}/\Delta x = 20$ to 30, there is no change greater than $\pm 4\%$ in the result of h^*. For the highly discretized case with $E_a = 20$, $\Gamma = 0.01$, and $L = 10$, there is no change greater than the prescribed average source spacing L in the result of h^* was the resolution as increased from $l_{1/2}/\Delta x = 5$ to 30. For $E_a = 30$, homogeneous case shown in Fig. 3.7(b), as the numerical resolution was increases from $l_{1/2}/\Delta x = 5$ to 10, the result of h^* increases by approximately 26%; as the numerical resolution was increases from $l_{1/2}/\Delta x = 10$ to 20, the change in the result of h^* is less than $\pm 1\%$. For the highly discretized case with $E_a = 30$, $\Gamma = 0.01$, and $L = 10$, there is no change greater than the prescribed average source spacing L in the result of h^* as the resolution was increased from $l_{1/2}/\Delta x = 5$ to 20.

Via performing convergence tests for the selected cases shown in Fig. 3.7(b), a numerical resolution of $l_{1/2}/\Delta x = 10$ has been demonstrated to be fairly sufficient to determine the critical reactive layer thickness for a self-sustainable propagation. For the highly discretized cases, since simulations have been performed at thicknesses being integer times

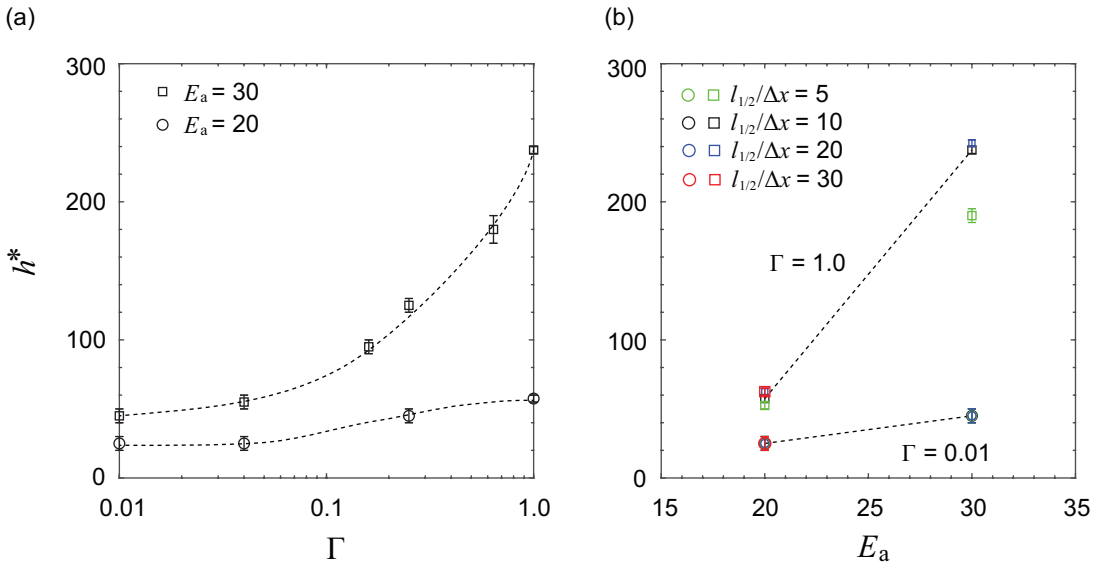

Figure 3.7: Critical thickness of the reactive layer h^* as (a) a function of spatial discreteness Γ and (b) a function of activation energy E_a with $L = 10$. Results of h^* at different numerical resolutions are plotted on (b).

of the source spacing, e.g., $h = 20$, 30, 40, and so on for $L = 10$, these cases result in h^* with an error range of $\pm L/2$. Although this error range is relatively great comparing to the determined h^* for the highly discretized cases ($\Gamma = 0.01$ and $L = 10$), simulations performed at different resolutions result in a consistent range of h within which the propagation limit is encountered, i.e., between $h = 20$ and 30 for $E_a = 20$, and between $h = 40$ and 50 for $E_a = 30$. Thus, further increasing the numerical resolution will very unlikely alter the qualitative dependence of h^* on the spatial discreteness Γ and activation energy E_a for $E_a = 20$ and $E_a = 30$ as reported in this Section. Additional details of how the convergence test has been performed for the cases shown in Fig. 3.7(b) are provided in Appendix E.

3.4 Theoretical model

The prediction of the V_{avg} *vs.* h relation using a theoretical model is plotted as the black curves in Fig. 3.6. This model is based on the assumption of a smoothly curved leading shock front followed by a steady, laminar-like reaction zone structure. First, using Wood and Kirkwood's quasi-one-dimensional model along the central streamline (equivalent to that along the rigid wall confinement in the problem considered in this study), the relation between the normal detonation velocity and the wave front curvature (D_{n}-κ relation), can be solved. [20] The smoothly curved leading wave front can then be geometrically constructed knowing the D_{n}-κ relation using the method first developed by Eyring *et al.* [5] This theoretical model, combining Wood and Kirkwood's solution and Eyring *et al.*'s geometric construction (see more details in Appendices C and D, respectively), was used by Li *et al.* [3, 35] to predict the V_{avg} *vs.* h relation.

For the cases with a low activation energy $E_{\text{a}} = 10$ shown in Fig. 3.6(a), the theoretical prediction is very close to the simulations results for both homogeneous and inhomogeneous cases at large thicknesses; a propagation limit, marked by the turning point of the V_{avg} *vs.* $1/h$ curve, is predicted by this model, but it is not captured by the numerical simulations. For higher activation energies $E_{\text{a}} = 20$ and 30 shown in Fig. 3.6(b) and (c), respectively, the model predicts significantly smaller velocity deficits and critical reactive layer thickness than the simulations results for the homogeneous and moderately inhomogeneous ($\Gamma = 0.25$) cases. The simulation results of V_{avg} for the near-limit cases with highly discretized inhomogeneities ($\Gamma = 0.01$) appear to be fairly close to the turning point of the theoretical prediction curves in Fig. 3.6(b) and (c).

3.5 Discussions

The simulation results reported in this chapter show that, for a sufficiently high activation energy, i.e., $E_a \geq 20$, the presence of spatially discrete reactive sources assist a detonation wave to propagate beyond the limit encountered in a homogeneous reactive medium. For the cases with a relatively high $E_a = 30$, as varying the spatial inhomogeneity of the initial distribution of reactant from a homogeneous medium to highly discretized reactive sources, the critical thickness of the reactive layer for a self-sustained propagation is reduced by nearly an order of magnitude (shown in Fig. 3.7). This sensitizing effect of spatial inhomogeneities on the near-limit propagation of detonation waves was first found by Li *et al.* [35] In their work, a pressure-dependent reaction model, which results in a smooth, laminar-like wave structure in the homogeneous case, was incorporated. The finding of this current study thus complements Li *et al.*'s work [35] by showing this enhancing effect in an unstable denotative system governed by Arrhenius kinetics. Given that the inhomogeneities were implemented as spatially discrete regions with highly concentrated reactant in this study, a significantly more pronounced effect of inhomogeneities on the propagation limit was found in the limit of extremely discretized sources of energy or point-like sources ($\Gamma \to 0$). The resulting dynamics in this limit could not be easily captured using a system previously explored by Li *et al.*, wherein inhomogeneities were implemented as variations in the initial density and temperature distribution.

A homogeneous mixture of reactive gases with $E_a = 20 \sim 30$ results in a detonation wave exhibiting regular or slightly irregular cell patterns. In such a cellular detonation complex, the transversely propagating shock waves are rather weak so that the triple-point interaction along the leading shock front cannot trigger localized explosions as strong as

those in a highly irregular mixture (with larger activation energies, e.g., $E_a > 40$). The reactive gas shocked by the weak parts of the leading wave front undergoes relatively slow combustion processes. Resulting from the lateral expansion, the strength of the leading shock decreases significantly in the transverse direction from the rigid wall towards the inert confinement. A more substantial amount of slowly reacting gas can thus be found near the expanding confinement interface downstream from the leading shock as indicated in Fig. 3.3(a). The energy release from these slowly reacting pockets of gas are not sufficient to restrengthen the leading shock wave propagating in a sub-critical case. Hence, a near-limit, cellular detonation wave under compressible confinement suffers not only losses in momentum of the expanding product in the x-direction, but also an insufficient support from the slow energy release of the weakly shocked reactant. This mechanism underlying the failure of a cellular detonation wave is likely verified by comparing the simulation results and model prediction of V_{avg} and h^* with a homogeneous reactive medium. For the cases with $E_a = 20$ and 30 (shown in Fig. 3.6(b) and (c)), the simulation results of h^* are significantly larger than those predicted by the theoretical model assuming a smoothly curved shock front wherein only losses in momentum are considered. For the cases with $E_a = 10$, the wave front resulting from the simulations is nearly smooth (Fig. 3.3(a)), and thus, the results of V_{avg} agree fairly well with the theoretical prediction as shown in Fig. 3.6(a).

For the homogeneous cases, the simulation results of h^* normalized by the half-reaction-zone length $l_{1/2}$ of the corresponding ideal ZND solution increases by nearly an order of magnitude as activation energy increases from 20 to 30, which are qualitatively consistent with the results reported by Reynaud *et al.* [100] This trend can be explained considering the above-described failure mechanism for regular or slightly irregular cellular detonations. As a large amount of reactive gas is processed by the leading shock

at a strength that is considerably lower than the corresponding CJ Mach number, the exothermic reaction is initiated at a relatively low temperature (much lower than the von Neumann (vN) temperature associated with $M_{\rm CJ}$). Given the exponential temperature-dependence of an activated reaction rate (for instance, single-step Arrhenius kinetics), at a very low post-shock temperature, the reaction rate is lower for a higher activation energy. Thus, the effective reaction zone length for these weakly shocked pockets (denoted as $l_{\rm eff}$ for convenience) increases with an increasing activation energy. The $l_{1/2}$ of the ZND solution is based on the assumption of a reaction process triggered by a leading shock of $M_{\rm CJ}$, i.e., initiated at a much higher temperature associated with the vN state. With an increasing $E_{\rm a}$, $l_{1/2}$ should thus decrease. Therefore, if the ratio $h^*/l_{\rm eff}$ remains a constant characteristic value for detonable mixtures with a similar detonation cell regularity, $h^*/l_{1/2}$ must increase as $E_{\rm a}$ increases.

By spatially discretizing the reactive medium (decreasing Γ while keeping L fixed), the chemical energy of the medium is concentrated into smaller and smaller reactive sources. In such cases, the amount of weakly shocked reactant that undergoes a slow heat release process is reduced and completely eliminated in the limit of $\Gamma \to 0$; the energy release is thus dominated by the localized explosions or high pressure pockets as these highly concentrated sources are triggered by the shock front. Therefore, this sensitizing effect of spatially discrete sources seems to be more pronounced with an increasing $E_{\rm a}$ in the range featuring a regular or slightly irregular, homogeneous mixture. For the cases with nearly point-like sources ($\Gamma = 0.01$), as shown in Fig. 3.7, the values of h^* resulting from the simulations with $E_{\rm a} = 20$ and 30 seem to converge to a rather narrow range of $h^* = 25$-45 for a fixed average source spacing $L = 10$. These results suggest that, in the limit of extremely discretized sources, h^* is more likely governed by the average number of localized explosions that can be triggered transversely across the reactive layer, in other

words, the ratio between h^* and the average source spacing L might be an approximately constant value, which is independent of E_a.

3.6 Conclusions

The effect of a spatially random distribution of inhomogeneities in the initial reactant concentration upon the propagation limit of gaseous detonation with compressible confinement has been studied via numerical simulations. Detonation systems with a homogeneous reactive medium are also simulated, and the results are compared with those from the simulations with an inhomogeneous medium in order to illustrate the effect of spatial inhomogeneities. A critical thickness of the reactive layer below which a detonation wave cannot propagate in a self-sustained manner has been determined for both homogeneous and inhomogeneous cases with $E_a = 20$ and 30, which represent a homogeneous detonable mixture featuring regular or slightly irregular cell patterns. The simulation results suggest that the imposed spatially discrete sources have a sensitizing effect on the near-limit propagation of detonation waves, i.e., concentrating the energy sources assists the detonation wave to propagate significantly beyond the limit that is encountered in the homogeneous system with the same amount of overall energy release. The mechanism underlying this sensitizing effect is related to the difference in the nature of the energy release processes between a homogeneous reactive medium and a random distribution of highly discretized reactive sources.

Chapter 4

Concluding remarks

This present body of work has been aimed to further elucidate the propagation mechanism of detonation waves of a spatially inhomogeneous nature via numerical simulations. Instead of directly resolving the naturally developed inhomogeneities within a detonation wave complex which takes a tremendous amount of computational effort, the approach of imposing discretely located reactive sources to the medium has been explored in this current work. In Ch. 2, discrete sources were introduced to adiabatic detonation systems with a hierarchy of complexities in order to investigate the effect of spatial inhomogeneities on the propagation velocity. The simulation results reveal that, with a sufficiently inhomogeneous reactive medium, a detonation wave propagates at a velocity that is significantly greater than the CJ velocity for the same amount of overall energy release. This super-CJ wave propagation can be understood as a weak detonation due to the non-equilibrium state at the effective sonic surface. In Ch. 3, a random distribution of spatially discrete sources was implemented into a two-dimensional detonation system confined by an inert, compressible layer of gas. The simulation results show that, for a sufficiently high activation energy, the spatial inhomogeneities assist a detonation wave to propagate beyond the limit that is encountered in a homogeneous reactive medium with the equivalent amount

of energy release. The underlying sensitization mechanism is due to the energy release dominated by the localized explosions as the highly discretized sources are triggered.

Appendix A

Derivation of the Favre-averaged equations, the master equation, and the thermicity terms

The complete derivation of the Favre-averaged (i.e., density-weighted, spatio-temporally averaged) equations, the master equation, and the thermicity terms (ϕ, ϕ_{M}, ϕ_{T}, and ϕ_{R}) are presented in this Appendix. The averaging is performed in a reference frame moving at the averaged wave propagation velocity V_{avg}. In this moving reference frame, the spatial coordinate and the x-component of particle velocity are transformed as $x' = x - V_{\mathrm{avg}}t$ and $u' = u - V_{\mathrm{avg}}$, respectively. For convenience, u denotes the x-component of particle velocity with respect to the moving frame in this Appendix.

A simple spatio-temporal averaging (or only temporal for one-dimensional cases), i.e., Reynolds averaging procedure, is then applied to density and pressure as follows

$$\bar{\rho}\left(x'\right) = \frac{1}{t_2 - t_1}\int_{t_1}^{t_2}\frac{1}{y_2 - y_1}\int_{y_1}^{y_2}\rho\left(x', t\right)\mathrm{d}y\mathrm{d}t \quad \text{and} \quad \rho = \bar{\rho} + \rho^{\circ} \tag{A.1}$$

$$\bar{p}\left(x'\right)=\frac{1}{t_2-t_1}\int_{t_1}^{t_2}\frac{1}{y_2-y_1}\int_{y_1}^{y_2}p\left(x',t\right)\mathrm{d}y\mathrm{d}t \quad \text{and} \quad p=\bar{p}+p^{\circ} \tag{A.2}$$

where t_1 and t_2 indicate the starting and ending time of the period, and y_1 and y_2 indicate the lower and upper boundaries of the computational domain in the y-direction, over which ρ and p are averaged. The bar "–" and superscript "$\circ$" indicate spatio-temporally averaged variables and their corresponding fluctuating quantities. Favre averaging (i.e., density-weighted averaging) is applied to the particle velocity and reaction progress variable as follows,

$$u^{*}=\frac{\overline{\rho u}}{\bar{\rho}} \text{ and } u=u^{*}+u'' \tag{A.3}$$

$$Z^{*}=\frac{\overline{\rho Z}}{\bar{\rho}} \text{ and } Z=Z^{*}+Z'' \tag{A.4}$$

where superscripts "$*$" and "$''$" indicate Favre-averaged variables and their corresponding fluctuating quantities, respectively. The average structure of the wave is therefore governed by the one-dimensional, stationary Favre-averaged Euler equations as follows,

$$\frac{\partial}{\partial x'}\left(\bar{\rho}u^{*}\right)=0 \tag{A.5}$$

$$\frac{\partial}{\partial x'}\left(\bar{\rho}u^{*2}+\bar{p}+\overline{\rho u''^{2}}\right)=0 \tag{A.6}$$

$$\frac{\partial}{\partial x'}\left(\bar{\rho}e^{*}u^{*}+\bar{\rho}\left(e''u''\right)^{*}+\overline{pu}\right)=0 \tag{A.7}$$

where the averaged specific total energy e^{*} can be expressed as follows,

$$e^{*}=\frac{\bar{p}}{\bar{\rho}(\gamma-1)}+\frac{u^{*2}}{2}+\frac{Z^{*}Q}{\Gamma} \tag{A.8}$$

Knowing the upstream boundary condition, i.e., the initial state of the region ahead of

the leading shock, Eqs. A.5-C.1 can be integrated to obtain the following equations,

$$\bar{\rho}u^* = V_{\text{avg}} \tag{A.9}$$

$$\frac{V_{\text{avg}}^2}{\bar{\rho}} + \bar{p} + f = V_{\text{avg}}^2 + 1 \tag{A.10}$$

$$\frac{\gamma\bar{p}}{(\gamma-1)\bar{\rho}} + \frac{u^{*2}}{2} + \frac{Z^*Q}{\Gamma} + \frac{g}{V_{\text{avg}}} = \frac{\gamma}{\gamma-1} + Q + \frac{{V_{\text{avg}}}^2}{2} \tag{A.11}$$

where $f = \overline{\rho u''^2}$ and $g = \overline{\rho e'' u''} + \overline{p^\circ u''}$ are the intensities of mechanical and thermal fluctuations, respectively. With the averaged quantities V_{avg}, $\bar{p}$, $\bar{\rho}$, u^*, and Z^* calculated, f and g can be then evaluated using Eqs. C.4 and D.1. The average sound speed, which is assumed to be independent of the intensity of fluctuation, can be calculated as

$$c^* = \sqrt{\frac{\gamma\bar{p}}{\bar{\rho}}} \tag{A.12}$$

The effective sonic point in the one-dimensional averaged wave structure is located at the position at where $u^* + c^* = 0$. Considering Eqs. A.5 and A.6 and taking the expression for e^* (Eq. C.2) into Eq. C.1, after some algebraic manipulation, one obtains the so-called master equation as follows,

$$\frac{\mathrm{d}u^*}{\mathrm{d}x'} = \frac{\gamma u^* \frac{\mathrm{d}f}{\mathrm{d}x'} - (\gamma-1)\frac{\mathrm{d}g}{\mathrm{d}x'} - \frac{(\gamma-1)QV_{\text{avg}}}{\Gamma}\frac{\mathrm{d}Z^*}{\mathrm{d}x'}}{\bar{\rho}\left(c^{*2} - u^{*2}\right)} = \frac{\phi}{\bar{\rho}\left(c^{*2} - u^{*2}\right)} \tag{A.13}$$

where

$$\begin{aligned}
\phi_{\mathrm{M}} &= \gamma u^* \frac{\mathrm{d}f}{\mathrm{d}x'} \\
\phi_{\mathrm{T}} &= -(\gamma - 1)\frac{\mathrm{d}g}{\mathrm{d}x'} \\
\phi_{\mathrm{R}} &= -\frac{(\gamma - 1)QV_{\mathrm{avg}}}{\Gamma}\frac{\mathrm{d}Z^*}{\mathrm{d}x'} \\
\phi &= \phi_{\mathrm{M}} + \phi_{\mathrm{T}} + \phi_{\mathrm{R}}
\end{aligned} \tag{A.14}$$

The master equation describes how the particle velocity of a fluid element traversing through a one-dimensional, steady Favre-averaged wave structure is influenced by the thermicity (ϕ) due to mechanical fluctuations (ϕ_{M}), thermal fluctuations (ϕ_{M}), and chemical reaction progress (ϕ_{R}). Upon the flow passing through the averaged sonic point where the denominator of the master equation (Eq. D.3) equals zero, i.e., $c^{*2} - u^{*2} = 0$, the thermicity ϕ must vanish, i.e., $\phi = 0$. Otherwise, a singularity would be encountered at the averaged sonic point. Thus, the condition $\phi = 0$ at the sonic surface that permits a singularity-free wave structure is known as the *generalized CJ condition*.

Appendix B

Heuristic model for the discrete source detonation problem

The collection of a large number of interacting blast waves and other unsteady flow features that comprise the dynamics of the discrete source detonation problem are unlikely to be amenable to an analytic solution. In the limit of point-like energy sources (discreteness $\Gamma \to 0$) and the delay time going to zero ($\tau \to 0$), however, the problem becomes simpler. In this case, as shown in figure B.1(a), the blast wave from a new source originates on the shock front of the prior blast, initially with no other flow interactions involved. This problem, and the subsequent propagation of the blast, are considered in this Appendix in an attempt to construct an analytic solution to this problem. It should be emphasized that this is a constructed solution, in which previously known solutions are patched together in an *ad hoc*, or heuristic, manner, rather than a solution to the discrete detonation problem derived rigorously from the governing conservation laws.

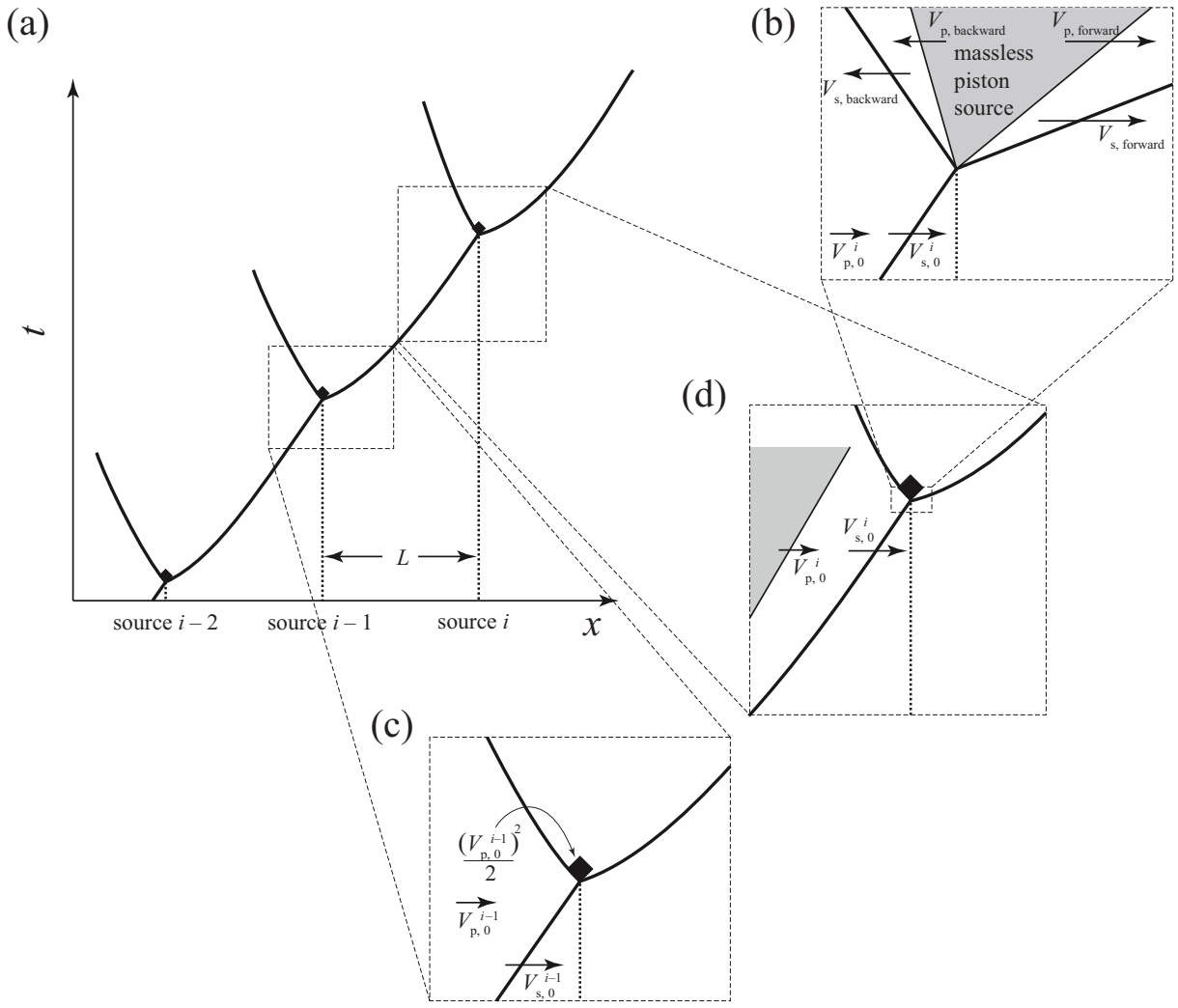

Figure B.1: Schematic illustration of the one-dimensional, discrete-source detonation propagation problem, as an x-t (space-time) diagram (a). In (b), the mechanism of source energy deposition is assumed to occur via the impulsive motion of two outward-facing, massless pistons. The approximation of the carried-over influence from the previous sources onto the $(i-1)^{\text{th}}$ source is shown in (c). In (d), the carried-over particle velocity imposed on the i^{th} source, $V^i_{\text{p},0}$, is approximated as the piston velocity required to sustain the instantaneous shock velocity, $V^i_{\text{s},0}$.

B.1 Taylor-Sedov solution for point-source blast

An approximate, analytical solution to this problem for the case where the delay time and discreteness are both taken to the limit of zero begins with the similarity solution for the planar version of the well-known point-blast problem of Taylor and Sedov [105]. For a planar blast wave, the Taylor-Sedov solution that governs the motion of the shock front is given by the following non-dimensionalized equation,

$$V_{\text{inst}} = \frac{\mathrm{d}x_{\text{s}}}{\mathrm{d}t} = \sqrt{\frac{0.5Q}{\mathrm{B}x_{\text{s}}}} \tag{B.1}$$

where V_{inst} is the instantaneous velocity of the leading shock front, x_{s} is the position of the leading shock front, and B is a dimensionless energy parameter depending on the specific heat capacity ratio γ. Considering that the point source releases its energy in an initially uniform and quiescent medium, the source energy Q is equally partitioned into forward and backward propagating blast waves. The factor of 0.5 in (B.1) thus indicates that only half of the source energy contributes to the forward propagating blast wave.

B.2 Energy partition of blast waves

Except for the first source, each subsequent source releases its energy at the shock front originating from the previous source; thus, the blast energy is not equally partitioned into forward and backward propagating blast waves. In order to estimate this partitioning, the following model of blast energy deposition is proposed. As illustrated in figure B.1(b), the mechanism of source energy deposition is hypothesized to be two massless pistons, one that pushes outward into the undisturbed gas ahead of the blast and the other that pushes into the gas behind the blast from the prior source. An approximation

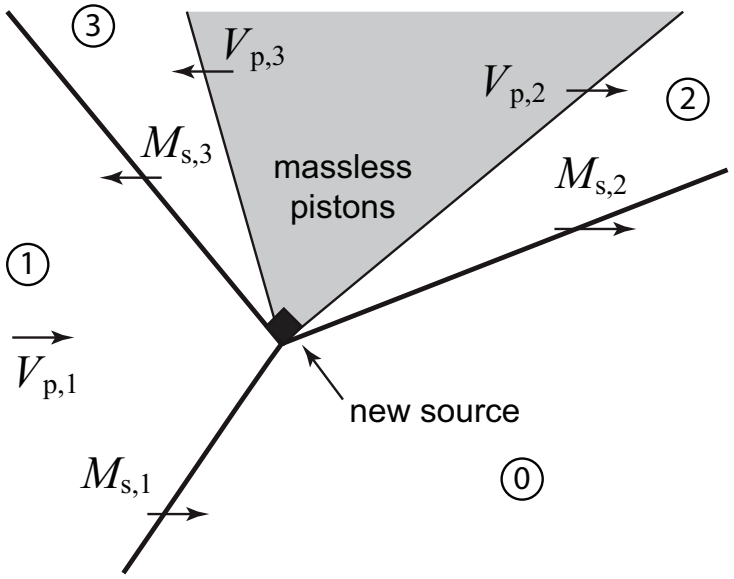

Figure B.2: Schematic layout of the gasdynamic analysis for the energy deposition process of a new source modeled as two massless pistons impulsively pushing forward and backward.

of blast energy partitioning can be made based on a simple analysis of the gasdynamics shortly after a new source depositing its energy, as detailed in the following paragraph.

In order to demonstrate this simple analysis, figure B.1(b) is redrawn as figure B.2 with different regions labeled as follows: Region (0) is the undisturbed region ahead of the leading shock front; Region (1) is the gas behind the blast wave from the previous source; Region (2) is the gas behind the forward-propagating shock wave generated by the new source; Region (3) is the gas behind backward-propagating shock generated by the new source. The Mach numbers associated with the incident blast from the previous source, the forward-propagating shock from the new source, and the backward-propagating shock from the new source are denoted as $M_{s,1}$, $M_{s,2}$, and $M_{s,3}$, respectively. The particle velocity in Region (1) is $V_{p,1}$; the particle velocity in Region (2) or piston velocity pushing the forward-propagating shock is $V_{p,2}$; the particle velocity in Region (3) or piston velocity

pushing the backward-propagating shock is $V_{\mathrm{p},3}$.

The particle (or piston) velocity V_{p} required to maintain a strong shock wave of a Mach number M_{s} can be calculated as

$$V_{\mathrm{p}} = \frac{2}{\gamma+1} M_{\mathrm{s}} c \tag{B.2}$$

where c is the sound speed in the gas ahead of the shock wave. Via this relation, the blast Mach numbers can be expressed in terms of the particle velocities and sound speed in different regions as follows,

$$M_{\mathrm{s},1} = \frac{\gamma+1}{2}\frac{V_{\mathrm{p},1}}{c_0}, \quad M_{\mathrm{s},2} = \frac{\gamma+1}{2}\frac{V_{\mathrm{p},2}}{c_0}, \quad M_{\mathrm{s},3} = \frac{\gamma+1}{2}\frac{(V_{\mathrm{p},1}+V_{\mathrm{p},3})}{c_1} \tag{B.3}$$

Applying the Rankin-Hugoniot relations for strong shocks, the pressure ratio across each shock wave can be expressed as a function of the corresponding shock Mach number as follows,

$$\frac{p_1}{p_0} = \frac{2\gamma}{\gamma+1}(M_{\mathrm{s},1})^2, \quad \frac{p_2}{p_0} = \frac{2\gamma}{\gamma+1}(M_{\mathrm{s},2})^2, \quad \frac{p_3}{p_1} = \frac{2\gamma}{\gamma+1}(M_{\mathrm{s},3})^2 \tag{B.4}$$

and the ratio between sound speeds c_0 and c_1 can be expressed as

$$\frac{c_1}{c_0} = \sqrt{\frac{2\gamma(\gamma-1)}{(\gamma+1)^2}} M_{\mathrm{s},1} \tag{B.5}$$

Taking the expression for the shock Mach numbers (B.3) into (B.4) and (B.5) and considering $p_0 = 1$, after some algebraic manipulation, the pressure in Regions (2) and (3) can be expressed in terms of the particle velocities as follows,

$$p_2 = \frac{\gamma(\gamma+1)}{2}\left(\frac{V_{\mathrm{p},2}}{c_0}\right)^2 \quad p_3 = \frac{\gamma(\gamma+1)^2}{2(\gamma-1)}\left(\frac{V_{\mathrm{p},1}+V_{\mathrm{p},3}}{c_0}\right)^2 \tag{B.6}$$

Applying the condition that the pressure on both piston faces must be equal (since, being massless, they cannot exert any net force on the flow), i.e., $p_2 = p_3$, the following equation can be derived by equating the expressions for p_2 and p_3 (B.6):

$$V_{\mathrm{p},2} = \sqrt{\frac{\gamma+1}{\gamma-1}}\,(V_{\mathrm{p},1} + V_{\mathrm{p},3}) \tag{B.7}$$

Assuming that the particle motion behind the backward-propagating blast is much stronger than the particle motion behind the incident blast from the previous source, i.e., $V_{\mathrm{p},3} \gg V_{\mathrm{p},1}$, thus, $V_{\mathrm{p},1} + V_{\mathrm{p},3} \approx V_{\mathrm{p},3}$, and a relation between the two piston velocities $V_{\mathrm{p},2}$ and $V_{\mathrm{p},3}$ can be obtained,

$$\frac{V_{\mathrm{p},2}}{V_{\mathrm{p},3}} = \sqrt{\frac{\gamma+1}{\gamma-1}} \tag{B.8}$$

The source energy partitioned into forward- and backward-propagating blast waves can be estimated as the work done by the pistons pushing forward and backward, respectively. A factor η can be defined as the ratio of the energy partitioned into the forward-propagating blast over the total amount of source energy,

$$\eta = \frac{Q_{\mathrm{forward}}}{Q} = \frac{Q_{\mathrm{forward}}}{Q_{\mathrm{forward}} + Q_{\mathrm{backward}}} = \frac{V_{\mathrm{p},2} p_2 A \Delta t}{V_{\mathrm{p},2} p_2 A \Delta t + V_{\mathrm{p},3} p_3 A \Delta t} \tag{B.9}$$

Since the area A on which the pistons push and the time duration Δt are the same, and the pressures on the piston faces are equal ($p_2 = p_3$), taking the relation (B.8) between $V_{\mathrm{p},2}$ and $V_{\mathrm{p},3}$ into (B.9), the blast energy partition factor η can be obtained as a function of γ only,

$$\frac{Q_{\mathrm{forward}}}{Q} = \eta = \frac{1}{\sqrt{\frac{\gamma-1}{\gamma+1}} + 1} \tag{B.10}$$

Since only ηQ contributes to the forward propagating blast, the equation describing the

motion of the leading shock front needs to be modified,

$$V_{\text{inst}} = \frac{\mathrm{d}x_{\text{s}}}{\mathrm{d}t} = \sqrt{\frac{\eta Q}{\mathrm{B}x_{\text{s}}}} \tag{B.11}$$

Interestingly, (B.10) is the same partition of blast energy found by Sakurai [106] in examining planar blast waves generated by energy release at a stationary density interface (as opposed to energy release at a moving shock front in the current problem).

B.3 Carry-over of influence from one source to the next

Following the release of source energy, the subsequent blast wave motion is additionally influenced by the particle velocity that was imposed by the blast wave from the previous sources. Considering the energy partitioned into the forward propagating blast and the particle motion imposed by the previous source, the motion of the blast wave propagation from one source to the next (from the i^{th} to the $(i+1)^{\text{th}}$ source) is given by,

$$V_{\text{inst}} = \frac{\mathrm{d}x_{\text{s}}^{i}}{\mathrm{d}t} = \sqrt{\frac{\eta Q}{\mathrm{B}x_{\text{s}}^{i}}} + V_{\text{p}}^{i}\left(x_{\text{s}}^{i}\right) \tag{B.12}$$

where x_{s}^{i} is the leading shock position relative to the location of the i^{th} source, and $V_{\text{p}}^{i}\left(x_{\text{s}}^{i}\right)$ is the particle velocity carried over from the previous source. This relation (B.12) assumes that the blast wave from a source is additionally advected by the particle motion imposed by the prior source. Since the spacing between two consecutive sources is of unit length, x_{s}^{i} increases from 0 to 1 as the blast wave propagates from the i^{th} to the $(i+1)^{\text{th}}$ source, and it is related to the absolute position of the leading shock x_{s} relative to the location of the first source ($x = 0$) via $x_{\text{s}} = (i-1) + x_{\text{s}}^{i}$. Note that, for algebraic convenience, only

the leading shock position relative to the i^{th} source, x_{s}^i, is used to formulate the governing equations of the heuristic model in this Appendix. A series of *ad hoc* approximations are made to incorporate V_{p}^i into (B.12), as detailed in the following paragraphs.

The carried-over particle velocity at the location of a newly triggered (the i^{th}) source, i.e., $V_{\text{p}}^i(x_{\text{s}}^i = 0)$ or $V_{\text{p,0}}^i$, can be approximated as follows. The blast wave, which imposes $V_{\text{p,0}}^i$ onto the i^{th} source, is a result of the energy release of not only the $(i-1)^{\text{th}}$ source, but also all the previous sources (from the first one) with diminishing effect. As shown in figure B.1(c), this influence from the previous sources is approximated as the kinetic energy possessed by the particle motion imposed on the $(i-1)^{\text{th}}$ source, i.e., $\left(V_{\text{p,0}}^{i-1}\right)^2/2$, added to the forward-partitioned source energy ηQ to propel the blast propagating towards the i^{th} source. With this carried-over amount of energy from the previous sources, the velocity, at which the blast reaches the i^{th} source, can be obtained from the Taylor-Sedov solution,

$$V_{\text{s,0}}^i = \sqrt{\frac{\eta Q}{B} + \frac{\left(V_{\text{p,0}}^{i-1}\right)^2}{2}} \tag{B.13}$$

The particle velocity imposed on the i^{th} source, $V_{\text{p,0}}^i$, as shown in figure B.1(d), can be then approximated as the piston velocity required to sustain the blast front moving at its approximated instantaneous velocity $V_{\text{s,0}}^i$,

$$V_{\text{p,0}}^i = \frac{2}{\gamma+1} V_{\text{s,0}}^i = \frac{2}{\gamma+1}\sqrt{\frac{\eta Q}{B} + \frac{\left(V_{\text{p,0}}^{i-1}\right)^2}{2}} \tag{B.14}$$

As the carried-over particle velocity is zero when the first source releases energy, V_{p}^1, the subsequent values of $V_{\text{p,0}}^i$ can be calculated recursively. As the blast wave propagates to the next source, the influence of the previous source on the particle motion should diminish. In order to consider this effect, V_{p}^i is modeled to be inversely proportional to

x_{s}^{i},

$$V_{\mathrm{p}}^{i}\left(x_{\mathrm{s}}^{i}\right)=\frac{1}{x_{\mathrm{s}}^{i}+1}V_{\mathrm{p},0}^{i} \tag{B.15}$$

Note that the factor $1/\left(x_{\mathrm{s}}^{i}+1\right)$ is an *ad hoc* approximation made to consider the diminishing effect of the imposed particle motion, but not rigorously derived from the solution for the blast wave profile. When the leading shock front just reaches the i^{th} source ($x_{\mathrm{s}}^{i}=0$), (B.15) gives $V_{\mathrm{p}}^{i}\left(x_{\mathrm{s}}^{i}=0\right)=V_{\mathrm{p},0}^{i}$; when the leading shock reaches the next source ($x_{\mathrm{s}}^{i}=1$), (B.15) gives $V_{\mathrm{p}}^{i}\left(x_{\mathrm{s}}^{i}=1\right)=0.5V_{\mathrm{p},0}^{i}$.

Taking the *ad hoc* approximations of V_{p}^{i} (B.13)-(B.15) into (B.12), the equation describing the leading shock propagation from one source to the next is formulated as follows,

$$V_{\mathrm{inst}}=\frac{\mathrm{d}x_{\mathrm{s}}^{i}}{\mathrm{d}t}=\sqrt{\frac{\eta Q}{\mathrm{B}x_{\mathrm{s}}^{i}}}+\frac{1}{\left(x_{\mathrm{s}}^{i}+1\right)}\underbrace{\frac{1}{(\gamma+1)}\sqrt{\frac{\eta Q}{B}+\frac{\left(V_{\mathrm{p},0}^{i-1}\right)^{2}}{2}}}_{V_{\mathrm{p},0}^{i}} \tag{B.16}$$

By solving (B.16) source by source, the model predictions for the instantaneous velocity of the shock front V_{inst} as a function of shock front position x_{s} and the source-to-source average velocity $V_{\mathrm{avg,source}}$ can be obtained.

B.4 Summary of procedure

A summary of the procedure to calculate the model prediction of V_{inst} as a function of x_{s} and the average velocity of the leading shock propagating from the i^{th} to the $(i+1)^{\mathrm{th}}$ source $V_{\mathrm{avg,source}}^{i}$ is provided as follows:

- For the first source ($i=1$), since it deposits its energy into an initially uniform and quiescent medium without any carried-over influence, $V_{\mathrm{p}}^{1}=0$ and $\eta=0.5$. Having $V_{\mathrm{p}}^{1}=0$ in (B.12), the governing equation for V_{inst} reverts to the Taylor-Sedov point-

blast solution as (B.1).

- For the second source, V_{inst} can be obtained by evaluating the right-hand side of (B.16) where $V_{\text{p},0}^{i-1}$ for $i = 2$ is $V_{\text{p},0}^{1}$. Since there is no carried-over particle motion for the first source, $V_{\text{p},0}^{1} = 0$. The blast energy partition factor η can be calculated via (B.10). Thus, every element on the right-hand side of (B.16) is known, and V_{inst} for the second source can be calculated.

- For the third source ($i = 3$), V_{inst} can again be obtained by evaluating the right-hand side of (B.16). This time $V_{\text{p},0}^{i-1}$ that appears in (B.16) is $V_{\text{p},0}^{2}$, which has already been solved when evaluating the second term on the right-hand side of (B.16) for the second source or equivalently calculated via (B.14).

- For each subsequent source, since the input from the previous source $V_{\text{p},0}^{i-1}$ has already been solved, the instantaneous velocity of the shock front V_{inst} can be calculated via evaluating the right-hand side of (B.16).

- Knowing that the spacing between two sources is 1, the average velocity of the leading shock propagating from the i^{th} to the $(i+1)^{\text{th}}$ source, $V_{\text{avg,source}}^{i}$, can be expressed as follows,

$$1/V_{\text{avg,source}}^{i} = \int_{0}^{1} \frac{\mathrm{d}x_{\text{s}}^{i}}{V_{\text{inst}}\left(x_{\text{s}}^{i}\right)} \tag{B.17}$$

  With the model prediction of $V_{\text{inst}}\left(x_{\text{s}}^{i}\right)$ obtained from the previous steps, the right-hand side of (B.17) can be numerically integrated to compute $V_{\text{avg,source}}^{i}$.

B.5 Model results

The predictions of this model for the instantaneous velocity of the shock front are shown in figure 2.5(a). Note that, since the Taylor-Sedov similarity solution for a point

blast (in planar geometry) is used, the shock velocity at each source is initially infinite. The velocity decays as the blast propagates forward, then jumps up again as a new source is triggered. The minimum velocity before each new source is triggered monotonically increases as more sources are encountered, in qualitative agreement with the computational simulations. In figure 2.5(b), the average velocity (from one source to the next) is plotted as a dashed line, and again exhibits good qualitative agreement with simulations in the limit as discreteness $\Gamma \to 0$, although it tends to over-predict the final value of the plateau velocity. This model can be used to examine the effect of γ, which enters the model significantly via the partitioning of blast energy released at the shock front (B.10), as shown in figure 2.6(b). Again, the model captures the qualitative trend of an increasing deviation away from the CJ solution as γ approaches unity, although the predicted deviation is more than twice that observed in the simulations.

Appendix C

Normal Detonation Velocity and Shock Front Curvature (D_{N}-κ) Relation

As Wood and Kirkwood[20] originally proposed, the D_{N}-κ relation can be obtained by solving the two-dimensional steady reactive Euler equation along the central axial streamline of the reaction zone. Given conditions of symmetry along this streamline, the transverse or radial flow velocity v is zero. Hence, the continuity equation along this streamline can be written as,

$$\frac{\partial \rho u}{\partial x} + \alpha \rho \frac{\partial v}{\partial y} = 0 \tag{C.1}$$

where y denotes the transverse and radial coordinate, and α has the value of 1 and 2 for the two-dimensional slab and axisymmetric geometries, respectively.

By performing a simple geometrical analysis along the leading shock front, a relation between the derivative of radial flow immediately behind the shock and the curvature of

the shock front at the central axis can be obtained as,

$$\frac{\partial v}{\partial y} = \frac{D - u_{\mathrm{vN}}}{R} \tag{C.2}$$

where u_{vN} is the axial velocity at the von Neumann point, and R is the local radius of curvature at the central axis. Considering that the length of the effective reaction zone is much smaller than the radius of curvature of the shock front, $\frac{\partial v}{\partial y}$ can be assumed to only vary with local axial velocity while R is taken as constant,

$$\frac{\partial v}{\partial y} = \frac{D - u(x)}{R} \tag{C.3}$$

The shock radius of curvature R can be linked to the shock front curvature κ through the following relation,

$$\kappa = \frac{\alpha}{R} \tag{C.4}$$

By numerically solving the two-dimensional steady reactive Euler equations coupled with the relation between the shock front curvature and the derivative of radial flow velocity along the central axial streamline, a unique value of κ can be determined for a given detonation velocity. Thus, detonation velocity can be obtained as a function of shock front curvature. This relation relates the normal component of detonation velocity D_{N} to the local shock front curvature away from the central axis. Note that the α appearing in Eq. (C.4) will cancel out with that in the equations of mass and momentum conservation, so the solutions of the governing equations for the D_{N}-κ relation for two-dimensional slab and axisymmetric geometries will be the same.

Appendix D

Geometric Construction of Detonation Wave Front

The approach of geometrically constructing the detonation wave front utilizing the D_{N}-κ relation (see Appendix C) was originally developed by Eyring et al. [5] to obtain a relation for the detonation velocity as a function of charge thickness or radius. In this model, any small portion of the wave front of the detonation propagating in a finite sized charge can be approximated by an infinitesimal segment of a steady spherical or cylindrical wave. [5] The radius of this wave can be obtained from the D_{N}-κ relation providing the detonation velocity component normal to the local wave front, D_{N}. As illustrated in Figure D.1 (a), starting from the central axis, a series of arc segments, which have their sweep angles of a small incremental angle ϕ and radii determined through the obtained D_{N}-κ relation, are piecewise drawn and connected to define the shape of the detonation wave front. From this simple geometrical analysis, the following relation can be obtained to calculate the half-thickness or the radius of the charge,

$$\frac{t}{2} \text{ or } r = R_n \sin n\phi + \sum_{i=1}^{n-1} (R_i - R_{i+1}) \sin i\phi \tag{D.1}$$

where n denotes the total number of incremental angle ϕ's required to reach the boundary of the charge. To find n, the shock polar matching condition needs to be applied at the explosive and confinement boundary. As the shock front angle to the incoming flow is obtained at the confinement boundary, n can be calculated via the following relation,

$$n\phi = 90^\circ - \sigma_\mathrm{B} \tag{D.2}$$

Provided σ_B, the shock front angle at the confinement boundary, and D_N-κ relation (see Appendix C) are known, the approach of constructing the detonation wave front can be then applied to solve for the steady detonation velocity as a function of charge thickness or radius.

In the limit where the incremental angles are taken as infinitesimally small, the Eyring construction can be cast in the form of a differential equation that relates the mathematical formulation of local curvature in terms of local wave front position, $x_\mathrm{s}(y)$, and its first and second-order derivatives with respect to y, to the local curvature determined by the calculated D_N-κ relation. As illustrated in Fig. D.1 (b), the local D_N can be related to the local slope of the wave front profile, $\frac{\mathrm{d}x_\mathrm{s}}{\mathrm{d}y}$, as follows,

$$D_\mathrm{N} = \frac{D}{\sqrt{1 + \left(\frac{\mathrm{d}x_\mathrm{s}}{\mathrm{d}y}\right)^2}} \tag{D.3}$$

Thus, the governing differential equation can be formulated as,

$$\frac{\frac{\mathrm{d}^2 x_\mathrm{s}}{\mathrm{d}y^2}}{\left[1 + \left(\frac{\mathrm{d}x_\mathrm{s}}{\mathrm{d}y}\right)^2\right]^{\frac{3}{2}}} = \kappa\left(D_\mathrm{N}\right) = \kappa\left(\frac{D}{\sqrt{1 + \left(\frac{\mathrm{d}x_\mathrm{s}}{\mathrm{d}y}\right)^2}}\right) \tag{D.4}$$

This equation can be numerically integrated starting from the centerline boundary condition ($\frac{\mathrm{d}x_\mathrm{s}}{\mathrm{d}y} = 0$) and integrating toward the edge of the charge in order to compute the critical diameter for a given detonation velocity. This equation is seen to be identical to that obtained via Detonation Shock Dynamics when the front evolution equation is relaxed to a steady state solution. This integration procedure is continued outward, with the shock angle continuously decreasing, until the shock angle matches the value determined by shock polar analysis, σ_B, as shown in Fig D.1 (b). In the problem studied in Ch. 3, the acoustic impedance in the inert gas confinement is the same as that in the initial reactive layer. The σ_B for such a case is thus assumed to associated with a sonic flow condition behind the leading shock.

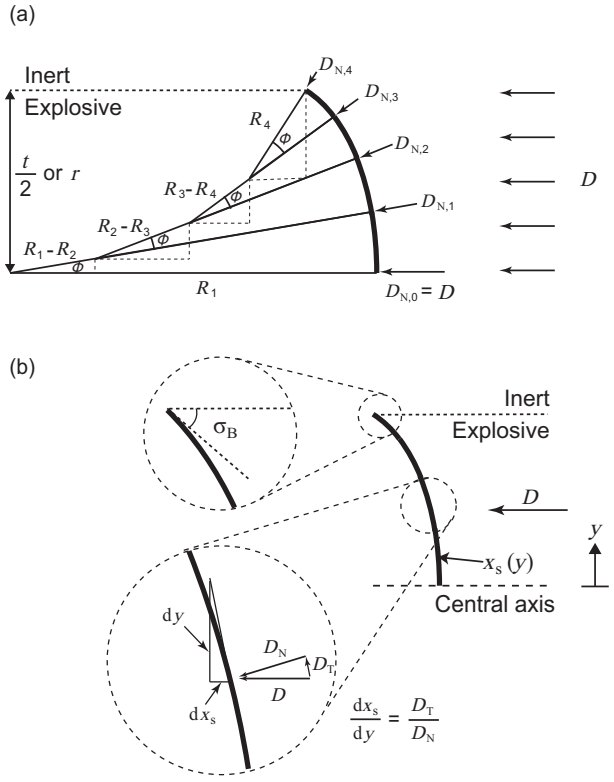

Figure D.1: Illustations of (a) the geometric construction of detonation wave front after Eyring *et al.* [5], (b) geometric relation between local D_N and the slope of the shock wave front profile, and the shock angle at the confinement boundary.

Appendix E

Numerical convergence study for critical reactive layer thickness

For both of the moderately high activation energies considered in Ch. 3, i.e., $E_a = 20$ and $E_a = 30$, numerical convergence tests have been performed for the homogeneous cases ($\Gamma = 1$) and the most highly discretized cases ($\Gamma = 0.01$ and $L = 10$). The convergence study for the resulting critical reactive layer thickness h^* from these cases is shown as the "go" *vs.* "no-go" charts plotted in Figs. E.1 and E.2.

In Figs. E.1 and E.2, each symbol represents a case of one or several simulations with a reactive layer thickness h at a numerical resolution in terms of the number of computational cells per the ideal half-reaction-zone length $l_{1/2}/\Delta x$. In these figures, a circle $\circ$ indicates a "go", i.e., a case resulting in a self-sustainable propagation; a cross $\times$ indicates a "no-go", i.e., a case of propagation failure. The dashed line indicates the boundary between "go" and "no-go" results that defines the critical thickness h^* as a function of numerical resolution. Considering the stochastic nature of the distribution of reactive sources in a highly inhomogeneous medium, for the near-limit cases, five simulations have

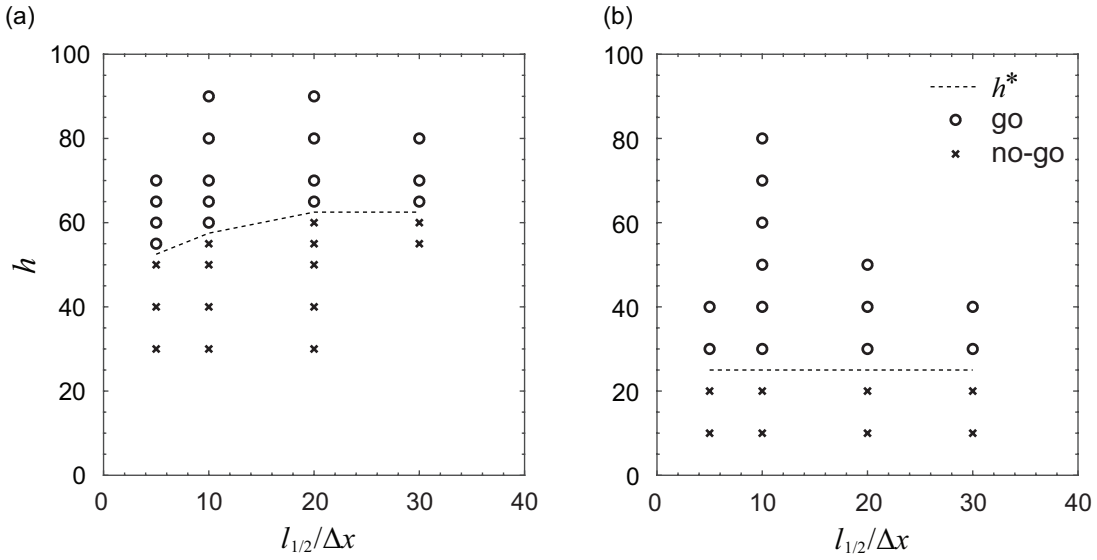

Figure E.1: Numerical convergence study for the result of critical reactive layer thickness h^* with $E_a = 20$ for (a) homogeneous cases and (b) inhomogeneous cases with $\Gamma = 0.01$ and $L = 10$.

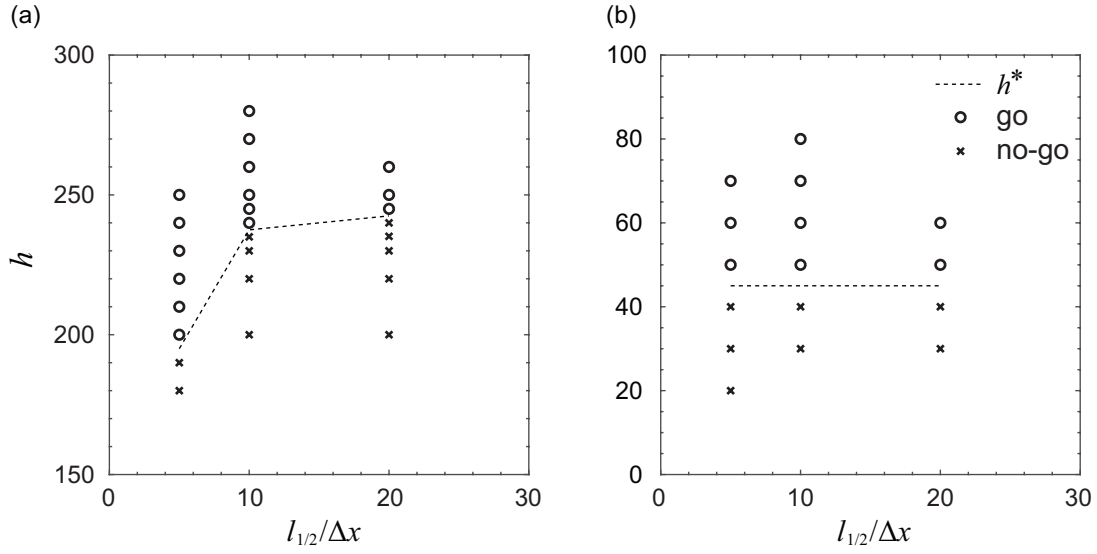

Figure E.2: Numerical convergence study for the result of critical reactive layer thickness h^* with $E_a = 30$ for (a) homogeneous cases and (b) inhomogeneous cases with $\Gamma = 0.01$ and $L = 10$.

been performed for the same value of h. Only if all of these five simulations result in a successful wave propagation over a distance that is more than approximately 150 times the average source spacing L, the case with the corresponding h is considered as a "go".

For the homogeneous cases with both $E_a = 20$ and $E_a = 30$ as shown in Figs. E.1(a) and E.2(a), respectively, simulations at a relatively coarse resolution result in a smaller critical thickness. This reduction in h^* could be attributed to the fact that the effect of numerical diffusion becomes more significant when the inviscid Euler equations are solved at coarser resolutions. In a cellular detonation structure that arises from a homogeneous reactive medium, there is a large amount of reactant that is shocked by the weak parts of the leading shock and undergoes a very slow burning process. The efficiency of this slow reaction process can be significantly enhanced by numerical diffusion. Simulations at coarse resolution likely result in an artificially (numerically) enhanced energy release rate and, thus, enables a detonation wave to propagate in a thinner reactive layer.

For the highly discretized cases shown in Figs. E.1(b) and E.2(b), simulations have been performed at thicknesses being integer times of the source spacing, e.g., $h = 20$, 30, 40, and so on for $L = 10$. Thus, these cases result in h^* with an error range of $\pm L/2$. Although this error range is relatively great comparing to the determined h^* for the highly discretized cases ($\Gamma = 0.01$ and $L = 10$), simulations performed at different resolutions result in a consistent range of h within which the propagation limit is encountered, i.e., between $h = 20$ and 30 for $E_a = 20$, and between $h = 40$ and 50 for $E_a = 30$.

Bibliography

[1] X. Mi, E.V. Timofeev, and A.J. Higgins. Effect of spatial discretization of energy on detonation wave propagation. *Journal of Fluid Mechanics*, 817:306–338, 2017.

[2] X.C. Mi, A.J. Higgins, H.D. Ng, C.B. Kiyanda, and N. Nikiforakis. Propagation of gaseous detonation waves in a spatially inhomogeneous reactive medium. *Physical Review Fluids*, 2(5):053201, 2017.

[3] J. Li, X. Mi, and A. J. Higgins. Geometric scaling for a detonation wave governed by a pressure-dependent reaction rate and yielding confinement. *Physics of Fluids*, 27(2), 2015.

[4] M.I. Radulescu, G.J. Sharpe, C.K. Law, and J.H.S. Lee. The hydrodynamic structure of unstable cellular detonations. *Journal of Fluid Mechanics*, 580:31–81, 2007.

[5] H. Eyring, R.E. Powell, G.H. Duffy, and R.B. Parlin. The stability of detonation. *Chemical Reviews*, 45(1):69–181, 1949.

[6] W. Fickett and W.C. Davis. *Detonation: Theory and Experiment*. Dover Publications, 2000.

[7] J.H.S. Lee. *The Detonation Phenomenon*. Cambridge University Press, 2008.

[8] Yu.N. Denisov and Ya.K. Troshin. On the mechanism of detonative combustion. *Eighth Symposium (International) on Combustion*, 8(1):600 – 610, 1961.

[9] J.H.S. Lee and M.I. Radulescu. On the hydrodynamic thickness of cellular detonations. *Combustion, Explosion, and Shock Waves*, 41(6):745–765, 2005.

[10] C.B. Kiyanda and A.J. Higgins. Photographic investigation into the mechanism of combustion in irregular detonation waves. *Shock Waves*, 23(2):115–130, 2013.

[11] P. Howe, R. Frey, and G. Melani. Observations concerning transverse waves in solid explosives. *Combustion Science and Technology*, 14(1-3):63–74, 1976.

[12] P.A. Urtiew, A.S. Kusubov, and R.E. Duff. Cellular structure of detonation in nitromethane. *Combustion and Flame*, 14:117–122, 1970.

[13] AJ Higgins. Discrete effects in energetic materials. In *Journal of Physics: Conference Series*, volume 500, page 052016, 2014.

[14] R. Knepper, R.R. Wixom, M.P. Marquez, and A.S. Tappan. Near-failure detonation behavior of vapor-deposited hexanitrostilbene (HNS) films. In *AIP Conference Proceedings*, volume 1793, page 030014, 2017.

[15] D.L. Chapman. On the rate of explosion in gases. *Philosophical Magazine*, 47(284):90–104, 1899.

[16] É. Jouguet. Sur la propagation des réactions chimiques dans les gaz. *Journal des Mathématiques Pures et Appliquées, série*, 1:347–425, 1905.

[17] Y.B. Zeldovich. On the theory of the propagation of detonation in gaseous systems. 1950.

[18] J. von Neumann. Theory of detonation waves. Technical report OSRD-549. Technical Report OSRD-549, National Defense Research Committee, 1942.

[19] W. Döring. Über den detonationsvorgang in gasen. *Annalen der Physik*, 435(6-7):421–436, 1943.

[20] W.W. Wood and J.G. Kirkwood. Diameter effect in condensed explosives. The relation between velocity and radius of curvature of the detonation wave. *The Journal of Chemical Physics*, 22(11):1920–1924, 1954.

[21] G.B. Whitham. *Linear and Nonlinear Waves*. John Wiley & Sons, 1974.

[22] J.B. Bdzil and D.S. Stewart. Modeling twodimensional detonations with detonation shock dynamics. *Physics of Fluids A: Fluid Dynamics (1989-1993)*, 1(7):1261–1267, 1989.

[23] D.S. Stewart and J.B. Bdzil. Examples of detonation shock dynamics for detonation wave spread applications. In 9^{th} *Symposium (International) on Detonation*, volume 152, pages 773–783. Office of Naval Research, Arlington, 1989.

[24] T.D. Aslam, J.B. Bdzil, and D.S. Stewart. Level set methods applied to modeling detonation shock dynamics. *Journal of Computational Physics*, 126(2):390–409, 1996.

[25] K. Mazaheri, Y. Mahmoudi, and M.I. Radulescu. Diffusion and hydrodynamic instabilities in gaseous detonations. *Combustion and Flame*, 159(6):2138 – 2154, 2012.

[26] A.A. Vasil'ev and Yu. Nikolaev. Closed theoretical model of a detonation cell. *Acta Astronautica*, 5(11-12):983–996, 1978.

[27] S. Goroshin, J.H.S. Lee, and Yu. Shoshin. Effect of the discrete nature of heat sources on flame propagation in particulate suspensions. *Proceedings of the Combustion Institute*, 27(1):743–749, 1998.

[28] J.M. Beck and V.A. Volpert. Nonlinear dynamics in a simple model of solid flame microstructure. *Physica D: Nonlinear Phenomena*, 182(12):86–102, 2003.

[29] F.D. Tang, A.J. Higgins, and S. Goroshin. Effect of discreteness on heterogeneous flames: propagation limits in regular and random particle arrays. *Combustion Theory and Modelling*, 13(2):319–341, 2009.

[30] S. Goroshin, F.D. Tang, and A.J. Higgins. Reaction-diffusion fronts in media with spatially discrete sources. *Physical Review E*, 84(2):027301, 2011.

[31] F.D. Tang, A.J. Higgins, and S. Goroshin. Propagation limits and velocity of reaction-diffusion fronts in a system of discrete random sources. *Physical Review E*, 85:036311, Mar 2012.

[32] X. Mi, A.J. Higgins, S. Goroshin, and J.M. Bergthorson. The influence of spatial discreteness on the thermo-diffusive instability of flame propagation with infinite lewis number. *Proceedings of the Combustion Institute*, 36(2):2359–2366, 2017.

[33] D.S. Stewart and B.W. Asay. Discrete modeling of beds of propellant exposed to strong stimulus. In P. C. Fife, A. Liñán, and F.A. Williams, editors, *Dynamical Issues in Combustion Theory*, volume 35 of *The IMA Volumes in Mathematics and its Applications*, pages 241–257. Springer New York, 1991.

[34] E.O. Morano and J.E. Shepherd. Effect of reaction rate periodicity on detonation propagation. *AIP Conference Proceedings*, 620(1):446–449, 2002.

[35] J. Li, X. Mi, and A.J. Higgins. Effect of spatial heterogeneity on near-limit propagation of a pressure-dependent detonation. *Proceedings of the Combustion Institute*, 35(2):2025–2032, 2015.

[36] A.K. Oppenheim. Development and structure of plane detonation waves. In *Fourth AGARD Combustion and Propulsion Colloquium*, pages 186–258, 1961.

[37] H.L. Brode. Numerical solutions of spherical blast waves. *Journal of Applied Physics*, 26(6):766–775, 1955.

[38] E. F. Toro. *Riemann Solvers and Numerical Methods for Fluid Dynamics*. Springer, third edition, 2009.

[39] T. Saito, P. Voinovich, E. Timofeev, and K. Takayama. Development and application of high-resolution adaptive numerical techniques in shock wave research center. In E.F. Toro, editor, *Godunov Methods*, pages 763–784. Springer US, 2001.

[40] J.B. McVey and T.Y. Toong. Mechanism of instabilities of exothermic hypersonic blunt-body flows. *Combustion Science and Technology*, 3(2):63–76, 1971.

[41] A.R. Kasimov and D.S. Stewart. On the dynamics of self-sustained one-dimensional detonations: A numerical study in the shock-attached frame. *Physics of Fluids*, 16(10):3566–3578, 2004.

[42] C. Leung, M.I. Radulescu, and G.J. Sharpe. Characteristics analysis of the one-dimensional pulsating dynamics of chain-branching detonations. *Physics of Fluids (1994-present)*, 22(12):126101, 2010.

[43] D.R. White. Turbulent structure of gaseous detonation. *The Physics of Fluids*, 4(4):465–480, 1961.

[44] A. Sow, A. Chinnayya, and A. Hadjadj. Mean structure of one-dimensional unstable detonations with friction. *Journal of Fluid Mechanics*, 743:503–533, 3 2014.

[45] A.J. Higgins. Steady one-dimensional detonations. In F. Zhang, editor, *Shock Waves Science and Technology Library*, volume 6, pages 33–105. Springer Berlin Heidelberg, 2012.

[46] J.B. Anderson and L.N. Long. Direct monte carlo simulation of chemical reaction systems: Prediction of ultrafast detonations. *The Journal of Chemical Physics*, 118(7):3102–3110, 2003.

[47] C.B. Kiyanda and A.J. Higgins. Photographic investigation into the mechanism of combustion in irregular detonation waves. *Shock Waves*, 23(2):115–130, 2013.

[48] J.J. Lee, G. Dupr, R. Knystautas, and J.H. Lee. Doppler interferometry study of unstable detonations. *Shock Waves*, 5(3):175–181, 1995.

[49] Y. Gao, H.D. Ng, and J.H. Lee. Experimental characterization of galloping detonations in unstable mixtures. *Combustion and Flame*, 162(6):2405 – 2413, 2015.

[50] S.I. Jackson, B.J. Lee, and J.E. Shepherd. Detonation mode and frequency variation under high loss conditions. In *25th International Colloquium on the Dynamics of Explosions and Reactive Systems*, 2015.

[51] M.I. Radulescu and J.E. Shepherd. Dynamics of galloping detonations: inert hydrodynamics with pulsed energy release. *Bulletin of the American Physical Society*, 60, 2015.

[52] W.C. Davis. The detonation of explosives. *Scientific American*, 256:106–112, 1987.

[53] X. Mi and A.J. Higgins. Influence of discrete sources on detonation propagation in a Burgers equation analog system. *Physical Review E*, 91:053014, May 2015.

[54] W. Fickett and W.C. Davis. *Detonation: Theory and Experiment*. Dover Publications, 1979.

[55] A. Majda. A qualitative model for dynamic combustion. *SIAM Journal on Applied Mathematics*, 41(1):70–93, 1981.

[56] M.I. Radulescu and J. Tang. Nonlinear dynamics of self-sustained supersonic reaction waves: Ficketts detonation analogue. *Physical Review Letters*, 107(16):164503, 2011.

[57] A.R. Kasimov, L.M. Faria, and R.R. Rosales. Model for shock wave chaos. *Physical Review Letters*, 110(10):104104, 2013.

[58] J. Tang and M.I. Radulescu. Dynamics of shock induced ignition in Fickett's model: Influence of χ. *Proceedings of the Combustion Institute*, 34(2):2035–2041, 2013.

[59] L.M. Faria and A.R. Kasimov. Qualitative modeling of the dynamics of detonations with losses. *Proceedings of the Combustion Institute*, 35(2):2015–2023, 2015.

[60] J. C. Gois, J. Campos, and R. Mendes. Extinction and initiation of detonation of NM-PMMA-GMB mixtures. *AIP Conference Proceedings*, 370(1):827–830, 1996.

[61] O.E. Petel, D. Mack, A.J. Higgins, R. Turcotte, and S.K. Chan. Comparison of the detonation failure mechanism in homogeneous and heterogeneous explosives. In *13th Symposium (International) on Detonation*, pages 2–11. Office of Naval Research, Arlington, 2006.

[62] O.E. Petel, D. Mack, A.J. Higgins, R. Turcotte, and S.K. Chan. Minimum propagation diameter and thickness of high explosives. *Journal of Loss Prevention in the Process Industries*, 20(4–6):578 – 583, 2007.

[63] A.J. Higgins. Measurement of detonation velocity for a nonideal heterogeneous explosive in axisymmetric and two-dimensional geometries. *AIP Conference Proceedings*, 1195(1):193–196, 2009.

[64] A.J. Higgins. Discrete effects in energetic materials. *Journal of Physics: Conference Series*, 500(5):052016, 2014.

[65] J. Buckmaster and J. Neves. One-dimensional detonation stability: The spectrum for infinite activation energy. *Physics of Fluids*, 31(12):3571–3576, 1988.

[66] M. Short. Multidimensional linear stability of a detonation wave at high activation energy. *SIAM Journal on Applied Mathematics*, 57(2):307–326, 1997.

[67] J.J. Erpenbeck. Stability of idealized one-reaction detonations: Zero activation energy. *Physics of Fluids*, 8(6):1192–1193, 1965.

[68] P. Clavin and L. He. Stability and nonlinear dynamics of one-dimensional overdriven detonations in gases. *Journal of Fluid Mechanics*, 306:353–378, 1 1996.

[69] P. Clavin, L. He, and F.A. Williams. Multidimensional stability analysis of overdriven gaseous detonations. *Physics of Fluids*, 9(12):3764–3785, 1997.

[70] M. Short and D.S. Stewart. The multi-dimensional stability of weak-heat-release detonations. *Journal of Fluid Mechanics*, 382:109–135, 3 1999.

[71] M. Short. An asymptotic derivation of the linear stability of the square-wave detonation using the newtonian limit. *Proceedings of the Royal Society of London A: Mathematical, Physical and Engineering Sciences*, 452(1953):2203–2224, 1996.

[72] H.I. Lee and D.S. Stewart. Calculation of linear detonation instability: one-dimensional instability of plane detonation. *Journal of Fluid Mechanics*, 216:103–132, 1990.

[73] M. Short and D.S. Stewart. Cellular detonation stability: A normal mode linear analysis. *Journal of Fluid Mechanics*, 368:229–262, 1998.

[74] G. Strang. On the construction and comparison of difference schemes. *SIAM Journal on Numerical Analysis*, 5(3):506–517, 1968.

[75] G.H. Morgan. The euler equations with a single-step arrhenius reaction. Technical report, University of Cambridge, 2013.

[76] C.B. Kiyanda, G.H. Morgan, N. Nikiforakis, and H.D. Ng. High resolution gpu-based flow simulation of the gaseous methane-oxygen detonation structure. *Journal of Visualization*, 18(2):273–276, 2015.

[77] A. Wright, A.J. Higgins, and S. Goroshin. The discrete regime of flame propagation in metal particulate clouds. *Combustion Science and Technology*, 188(11-12):2178–2199, 2016.

[78] F. Lam, X.C. Mi, and A.J. Higgins. Front roughening of flames in discrete media. *Physical Review E*, 96:013107, 2017.

[79] M. Hishida, T. Fujiwara, and P. Wolanski. Fundamentals of rotating detonations. *Shock Waves*, 19(1):1–10, 2009.

[80] J. Fujii, Y. Kumazawa, A. Matsuo, S. Nakagami, K. Matsuoka, and J. Kasahara. Numerical investigation on detonation velocity in rotating detonation engine chamber. *Proceedings of the Combustion Institute*, 36(2):2665–2672, 2017.

[81] S. Yao, X. Han, Y. Liu, and J. Wang. Numerical study of rotating detonation engine with an array of injection holes. *Shock Waves*, 27(3):467–476, 2017.

[82] J. Kindracki, P. Wolański, and Z. Gut. Experimental research on the rotating detonation in gaseous fuels–oxygen mixtures. *Shock Waves*, 21(2):75–84, 2011.

[83] B.A. Rankin, C.A. Fugger, D.R. Richardson, K.Y. Cho, J.L. Hoke, A.W. Caswell, J.R. Gord, and F.R. Schauer. Evaluation of mixing processes in a non-premixed rotating detonation engine using acetone plif imaging. In *54th AIAA Aerospace Sciences Meeting*, number 2016-1198, 2016.

[84] M. Short and J.J. Quirk. On the nonlinear stability and detonability limit of a detonation wave for a model three-step chain-branching reaction. *Journal of Fluid Mechanics*, 339:89–119, 1997.

[85] H.D. Ng and John H.S. Lee. Direct initiation of detonation with a multi-step reaction scheme. *Journal of Fluid Mechanics*, 476:179–211, 2003.

[86] W.P. Sommers and R.B. Morrison. Simulation of condensedexplosive detonation phenomena with gases. *Phys. Fluids*, 5(3):241–248, 1962.

[87] E.K. Dabora, J.A. Nicholls, and R.B. Morrison. The influence of a compressible boundary on the propagation of gaseous detonations. *Symposium (International) on Combustion*, 10(1):817 – 830, 1965. Tenth Symposium (International) on Combustion.

[88] E.K. Dabora, J.A. Nicholls, and M. Sichel. The interaction process between gaseous detonation waves and inert gaseous boundaries: final report. Technical Report 05170-3-F, The University of Michigan, Aircraft Propulsion Laboratory, 1965.

[89] S.B. Murray and J.H.S. Lee. The influence of yielding confinement on large-scale ethylene-air detonations. *Prog. Astronaut. Aeronaut*, 94:80–103, 1984.

[90] S.B. Murray and J.H.S. Lee. The influence of physical boundaries on gaseous detonation waves. *Prog. Astronaut. Aeronaut*, 106:329–355, 1986.

[91] A.A. Vasil'ev and D.V. Zak. Detonation of gas jets. *Comb. Expl. Shock*, 22:463–468, 1986.

[92] A.A. Borisov, S.V. Khomic, and V.N. Mikhalkin. Detonation of unconfined and semiconfined charges of gaseous mixtures. *Prog. Astronaut. Aeronaut*, 133:118–132, 1991.

[93] F.A. Bykovskii, S.A. Zhdan, and E.F. Vedernikov. Continuous spin detonations. *Journal of Propulsion and Power*, 22(6):1204, 2006.

[94] F.K. Lu and E.M. Braun. Rotating detonation wave propulsion: experimental challenges, modeling, and engine concepts. *Journal of Propulsion and Power*, 30(5):1125–1142, 2014.

[95] W. Rudy, M. Kuznetsov, R. Porowski, A. Teodorczyk, J. Grune, and K. Sempert. Critical conditions of hydrogen-air detonation in partially confined geometry. *Proceedings of the Combustion Institute*, 34(2):1965–1972, 2013.

[96] W. Rudy, M. Zbikowski, and A. Teodorczyk. Detonations in hydrogen-methane-air mixtures in semi confined flat channels. *Energy*, 116:1479–1483, 2016.

[97] W. Rudy, K. Dziubanii, M. Zbikowski, and A. Teodorczyk. Experimental determination of critical conditions for hydrogen-air detonation propagation in partially confined geometry. *International Journal of Hydrogen Energy*, 42(11):7366–7373, 2017.

[98] J. Grune, K. Sempert, A. Friedrich, M. Kuznetsov, and T. Jordan. Detonation wave propagation in semi-confined layers of hydrogen–air and hydrogen–oxygen mixtures. *International Journal of Hydrogen Energy*, 42(11):7589–7599, 2017.

[99] R.W. Houim and R.T. Fievisohn. The influence of acoustic impedance on gaseous layered detonations bounded by an inert gas. *Combustion and Flame*, 179:185–198, 2017.

[100] M. Reynaud, F. Virot, and A. Chinnayya. A computational study of the interaction of gaseous detonations with a compressible layer. *Physics of Fluids*, 29(5):056101, 2017.

[101] K.Y. Cho, J.R. Codoni, B.A. Rankin, J. Hoke, and F. Schauer. Effects of lateral relief of detonation in a thin channel. In *55th AIAA Aerospace Sciences Meeting*, page 0373, 2017.

[102] A.V. Gaathaug, K. Vaagsaether, and D. Bjerketvedt. Detonation failure in stratified layers–the influence of detonation regularity. In *26th International Colloquium on the Dynamics of Explosions and Reactive Systems*, 2017.

[103] J.R. Burr and K. Yu. Detonation wave propagation in cross-flow of discretely spaced reactant jets. In *53rd AIAA/SAE/ASEE Joint Propulsion Conference*, page 4908, 2017.

[104] J. Li, X. Mi, and A.J. Higgins. Propagation Distance Required to Reach Steady-State Detonation Velocity in Finite-Sized Charges. In 15th *Symposium (International) on Detonation*, pages 777–786. Office of Naval Research, Arlington, 2014.

[105] D.L. Jones. Strong blast waves in spherical, cylindrical, and plane shocks. *Physics of Fluids*, 4(9):1183–1184, 1961.

[106] A. Sakurai. Blast wave from a plane source at an interface. *Journal of the Physical Society of Japan*, 36(2):610–610, 1974.